Quantitative Magnetic Resonance Measurements of Porous Media:

Radio Frequency Field Mapping and Selective Pulse Design

by

Sarah Vashaee

Bachelor of Science, Sharif University of Technology, 2008

A Dissertation Submitted in Partial Fulfillment
of the Requirements for the Degree of

Doctor of Philosophy

in the Graduate Academic Unit of Physics

Supervisors:	Bruce J. Balcom, Ph.D., Physics Ben Newling, Ph.D., Physics
Examining Board:	Dennis W. Tokaryk, Ph.D., Physics Larry Calhoun, Ph.D., Chemistry Zong-Chao Yan, Ph.D., Physics
External Examiner:	Simon J. Doran, Ph.D. CRUK Cancer Imaging Centre, Institute of Cancer Research Surrey, UK

This dissertation is accepted by the
Dean of Graduate Studies

THE UNIVERSITY OF NEW BRUNSWICK

April 2015

ABSTRACT

Magnetic resonance imaging (MRI) is a powerful tool for the non-destructive measurement of fluid content and fluid behavior in porous media. The essential factor in quantitative MRI of such systems is a reliable measure of fluid quantity in the pore space. Quantitative imaging is impaired in many cases by non-uniform B_1 fields in the sample space.

In this thesis a novel method is described for mapping B_1 inhomogeneities based on measurement of the B_1 field employing centric-scan pure phase encode MRI measurements. The resultant B_1 map is employed to correct B_1 related non-uniformities in MR profiles, which leads to quantitative density profiling. The new B_1 mapping technique is also employed to investigate B_1 induced MRI artifacts by analyzing image distortions surrounding two geometrically identical metallic strips of aluminum and lead.

Quantitative density profiles may be acquired in porous media with a spatially selective adiabatic inversion pulse, which is immune to B_1 field non-uniformities. The pulse is applied in the presence of a slice selective magnetic field gradient to restrict the field of view to a region of interest in which the B_1 field is fairly uniform. This is advantageous in axial profiling of petroleum reservoir core samples and core plugs in which the sample of interest may be much longer than the natural field of view defined by the RF probe and region of constant magnetic field gradient. The adiabatic slice selection lends itself to a spatially selective T_2 distribution measurement when a CPMG pulse sequence follows the slice selection. This method is an alternative to MRI-based techniques for T_2 mapping in porous media when T_2 is required to be measured at only a few positions along the sample, and a resolution of 5 mm is acceptable.

The above T_2 distribution mapping method is compared with spin-echo SPI (SE-SPI) and DANTE-Z CPMG methods in terms of spatial resolution, minimum observable T_2 and sensitivity.

Finally, multi-slice T_2 measurement employing the longitudinal Hadamard encoding technique and adiabatic inversion pulses is discussed. The method has an inherent sensitivity advantage over corresponding slice-by-slice local T_2 measurements.

DEDICATION

To my parents

ACKNOWLEDGEMENTS

First, I would like to thank my supervisor Prof. Balcom and my co-supervisor Prof. Newling for providing me with the opportunity to complete my PhD thesis at the UNB MRI Centre. Their support and guidance made my thesis work possible. They have been actively interested in my work and have always been available to advise me. I am very grateful for their patience, motivation, enthusiasm, and immense knowledge in MRI.

I want to thank present and past members of the UNB MRI Centre, in particular Rodney MacGregor, Dr. Bryce MacMillan, Dr. Florin Marica, Dr. Fred Goora, Dr. Oleg Petrov, and Dr. Igor Mastikhin for giving me an introduction into the MRI lab and sharing their broad knowledge. I also thank Jennie McPhail, who has been very helpful throughout my time at UNB.

For this dissertation I would like to thank my reading committee members for their time, interest, and helpful comments.

I gratefully acknowledge the funding sources that made my Ph.D. work possible: NSERC of Canada, Canada Chairs Program, the Atlantic Innovation Foundation, Saudi Aramco, Conoco Phillips and Green Imaging Technologies.

Lastly, I would like to thank my family for all their love and encouragement. A special thanks to Matthew Ouellette and his family for supporting and encouraging me essentially every single day of my graduate studies.

Table of Contents

List of Tables

List of Figures

List of Symbols, Nomenclature or Abbreviations

1D	One-dimensional
2D	Two-dimensional
3D	Three-dimensional
2τ	Echo time
A	Amperes
a.u.	Arbitrary units
B_0	Static magnetic flux density
B_1 or B_{rf}	Radiofrequency magnetic flux density
$B_{1,app}$	Applied B_1
$B_{1,ind}$	Induced B_1 field
$B_{1,max}$	Maximum B_1 strength
B_{1eff}	Effective B_1
$B_{1x,ind}$	Induced B_1 along *x* direction
B_{1xy}	Transverse component of the B_1 field
$B_{1y,ind}$	Induced B_1 along *y* direction
$B_{1y.app}$	Applied B_1 along *y* direction
bw	Bandwidth
bw_{eff}	Effective bandwidth
bw^{sim}	Simulated bandwidth
bw_{eff}^{sim}	Simulated effective bandwidth
cm	Centimeter

CPMG	Carr-Purcell-Meiboom-Gill
DANTE	Delays Alternating with Nutation for Tailored Excitation
dhk	Double half *k*-space
$\vec{D}$	Electric displacement
EM	Electromagnetic
EMF or ζ	Electromotive Force or voltage
f	Frequency
FID	Free Induction Decay
FOV	Field of View
FW	Filter Width
G	Gauss or magnetic field gradient amplitude
$G_{max,x}$	Maximum magnetic field gradient strength along *x* direction
$G_{max,y}$	Maximum magnetic field gradient strength along *y* direction
$G_{max,z}$	Maximum magnetic field gradient strength along *z* direction
G_{slice} or G_{ss}	Slice selective magnetic field gradient
H_1	Magnetic field strength
$H_{1x,ind}$	Induced H_1 along *x* direction
$H_{1y,ind}$	Induced H_1 along *y* direction
$\mathbf{H}_n$	n^{th} order Hadamard matrix
HS	Hyperbolic Secant
H_{1x}	Magnetic field strength along x direction
H_{1y}	Magnetic field strength along y direction

$\vec{J}$	Current density
j	Imaginary number unit used to represent $\sqrt{-1}$
k	Propagation constant
$\vec{k}$	*k*-space vector
kHz	kilohertz
kW	kilowatt
L	Self-inductance
l_0	Inversion number
l_0^{sim}	Simulated inversion number
L_{metal}	Metal self-inductance
m	Meter
M	Mutual inductance
M_0	Equilibrium longitudinal magnetization
mm	Millimeter
MR	Magnetic Resonance
M_{rest} or M_z	Magnetization along $+z$
M_{xy}	Transverse magnetization
NMR	Nuclear Magnetic Resonance
Np	Neper
$\vec{n}$	Normal vector perpendicular to the surface
P	Supplied power
P_{90}	90˚ pulse duration

Q	Quality factor of the radiofrequency probe
R	Electrical resistance
RF	Radiofrequency
RF_{max}	Highest amplitude in the RF pulse envelope
R_{metal}	Metal electrical resistance
ROI	Region of Interest
S	Signal intensity, Siemens or surface
s	Second
SE-SPI	Spin Echo Single Point Imaging
SNR	Signal-to-Noise Ratio
SPI	Single Point Imaging
SPRITE	Single Point Ramped Imaging with T_1 Enhancement
SW	Sweep width
T	Tesla
t	Time
T_1	Spin-lattice relaxation time constant
$T_{1\rho}$	Spin-lattice relaxation in the rotating frame
T_2	Spin-spin relaxation time constant
T_2^*	Effective spin-spin relaxation time constant
T_{eff}	Effective pulse duration or effective pulse length
T_p	Slice selective pulse duration
t_p	Phase encoding time
t_{pulse}	Pulse duration or pulse length

TR	Repetition time
V	Voltage
Z_{metal}	Total impedance of the metal
α	Flip angle or attenuation constant
β	Phase constant or RF amplitude truncation constant
Δl	Deterioration of the inversion number
γ	Gyromagnetic ratio
δ	Skin depth
ΔB_0	Inhomogeneity of the static magnetic flux density
ε	Electrical permitivity
ε_o	Electrical permitivity of free space
κ	Proportionality constant
μ	Magnetic moment or magnetic permeability or degree of frequency modulation
μ_o	Magnetic permeability of free space
ρ_o	Grams per unit volume of ^1H material or proton density
σ	Electrical conductivity
σ_{metal}	Electrical conductivity of the metal
Φ	Magnetic flux
ω_0	Larmor frequency
ω_{rf}	RF pulse frequency

Chapter 1 – Introduction

1.1 Research motivation and objectives

Magnetic resonance (MR) is a spectroscopic technique, probing nuclei, that is sensitive to molecular scale structure and molecular dynamics. Since MR works at radio frequencies, whole sample measurements of all but the most conductive samples are possible and the method is not surface limited. These properties make MR an ideal probe for condensed matter. MR has been recognized for its potential in measuring the pore size distribution and fluid permeability of rock cores for well-logging and petrophysics research. Recent advances in quantitative magnetic resonance imaging (MRI) of reservoir rock core plugs have led to the development of new core analysis methods for capillary pressure and other petrophysical parameters [1-4].

The essential element in quantitative MRI of such systems is a reliable measure of fluid quantity in the pore space. Pure phase encoding MRI methods [4-6] have proven to be robust in their ability to generate quantitative images in porous media. However, we observed in this work that the images produced by the SPRITE method were very non-uniform for nominally uniform samples so the quantitative imaging was impaired. We showed the non-uniformities over the SPRITE images were due to non-uniform B_1 fields in the sample space, particularly when the sample of interest occupies a large fraction of the radiofrequency (RF) coil. The spatial variation of the B_1 field, both for excitation and reception, is one principal reason for non-uniform images of nominally uniform samples. The B_1 inhomogeneity problem may be solved by limiting the sample space in a larger RF probe [7] but this is not a very good use of the experimental sample space. We are

interested in developing new strategies, which improve quantitative MRI measurements without hardware modifications.

We developed a new B_1 mapping technique which is based on measurements of image intensities acquired with a series of low flip angle excitation pulses, employing centric scan Single Point Ramped Imaging with T_1 Enhancement (SPRITE) [5, 8]. A simple method is proposed for correcting B_1 inhomogeneity effects over the centric scan SPRITE images employing B_1 field maps.

As a pure phase encode method, the above B_1 mapping method works well even in the presence of conductive structures that support eddy currents. The new B_1 mapping technique was employed to isolate and determine B_1-induced eddy current effects near strips of metals in MR images. The strip geometry was chosen to mimic metal electrodes employed in electrochemistry studies. The results are particularly important for NMR and MRI of batteries and other electrochemical devices. Such analyses may become valuable in many applications involving battery systems [9-11].

In addition to employment of the above B_1 mapping technique to correct B_1 non-uniformities over centric scan SPRITE images, we introduced a second technique for quantitative profiling of petroleum reservoir core plugs. In axial profiling of petroleum reservoir core plugs, the samples of interest may be much longer than the natural field of view (FOV), defined by the RF probe and region of constant magnetic field gradient. Axial profiling of such samples results in distorted, non-quantitative profiles near the edge of the FOV due to B_1 field variation and nonlinear magnetic field variations. A new technique was developed to permit profiling of long extended samples. Spatially selective adiabatic inversion pulses [12], which are immune to B_1 non-uniformities, were

employed to restrict the interrogation to a region of interest that is a small section of the long core sample. The most important outcome of the method is a local T_2 distribution measurement. This method is conceptually similar to image selected *in vivo* spectroscopy (ISIS) techniques for spatial localization [13], but its application to porous media and to the determination of the T_2 relaxation time distribution is novel. Bulk CPMG was employed to measure T_2 at different positions with adiabatic slice selection. The ability of the adiabatic inversion CPMG method to measure almost the same range of T_2 as the bulk CPMG, makes the method very beneficial for quantitative analysis.

The adiabatic inversion CPMG method was compared with two other MR techniques developed at the UNB MRI Centre for the measurement of spatially resolved T_2 distributions, Spin-Echo Single Point Imaging (SE-SPI) [4] and DANTE-Z CPMG [14] These methods were, in turn, compared with a "gold standard" bulk CPMG method. The three methods, Spin-Echo Single Point Imaging (SE-SPI) [4], DANTE-Z CPMG [14] and adiabatic inversion CPMG were compared in terms of spatial resolution, minimum observable T_2, and sensitivity. The adiabatic inversion followed by a CPMG pulse train is the preferred way to measure local T_2 distributions with higher sensitivity, provided a regional measurement of coarse spatial resolution is sufficient.

It is very convenient in slice selective MR to improve the overall efficiency of data acquisition by employing multi-slice techniques. Considering the excellent ability of adiabatic inversion pulses to measure T_2 distributions, to conclude this thesis we employed multiband adiabatic inversion pulses to allow multi-slice T_2 measurements across a porous medium. However, the multi-slice selection leads to the superposition of information from different slices. To detangle the individual slice information, the

modified experiment must be performed several times with individual slice information labeled uniquely for each of the sub-experiments. We employed the Hadamard matrices [15, 16] to encode the signal from different slices of interest.

Multi-slice T_2 measurement employing the Hadamard encoding technique has an inherent sensitivity advantage over corresponding slice-by-slice local T_2 measurements. While Hadamard encoding is well established for local spectroscopy, this thesis is the first use of Hadamard encoding for local T_2 measurements.

1.2 Thesis outline

The thesis is organized as follows:

Chapter 1 provides an introduction as well as an outline of the thesis work.

Chapter 2 introduces the relevant MRI background.

Chapter 3 describes B_1 mapping with a pure phase encode approach and quantitative density profiling of rock core plugs. The chapter is largely based on a paper published in the *Journal of Magnetic Resonance* [17]. The author of the thesis performed the experiments and data analysis in this chapter and wrote the corresponding article of which she is first author. The paper formed the basis of a related patent [18].

Chapter 4 describes mapping B_1-induced eddy current effects near metallic structures in MR images. A comparison of simulation and experimental results was undertaken for this chapter. This chapter is largely based on an article published in the *Journal of Magnetic Resonance* [19]. A significantly greater level of detail and mathematical rigor is provided in this chapter, compared to the article. This chapter is an important application of the B_1 mapping method with a pure phase encode imaging

method. The author of the thesis performed the experiments and data analysis in this chapter and wrote the corresponding article of which she is first author. Dr. Fred Goora performed the simulations.

Chapter 5 presents region of interest selection of long core plug samples by MRI. A new technique has been employed to perform profiling and local T_2 measurement in porous media MRI. The chapter is largely based on a paper published in the journal *Measurement Science and Technology* [20]. The author of the thesis designed and performed all of the experiments and data analysis in this chapter and wrote the corresponding article of which she is first author.

Chapter 6 describes a comparison of three MR methods for spatially resolved T_2 distribution measurements in porous media and the relative benefits and disadvantages of each method. This chapter is largely based on an article, which has been published in the journal *Measurement Science and Technology* [21]. The author of the thesis performed the experiments and the simulations in this chapter, performed the data analysis and wrote the corresponding article of which she is first author.

Chapter 7 demonstrates local T_2 measurement employing longitudinal Hadamard encoding and adiabatic inversion pulses in porous media. The author of the thesis performed all of the experiments and data analysis in this chapter.

Chapter 8 provides the conclusion of this thesis and recommendations for future work.

This thesis is written in the form of a thesis with chapters as papers. The content has been structured such that successive topics build on each other and flow naturally between successive chapters.

1.3 References

[1] C.M. Muir, B.J. Balcom, Pure phase encode magnetic resonance imaging of fluids in porous media, Ann. Rep. NMR Spec. 77 (2012) 81-113.

[2] J. Mitchell, J. Staniland, R. Chassagne, K. Mogensen, S. Frank, E.J. Fordham, Mapping oil saturation distribution, in a limestone plug with low-field magnetic resonance, J. Petrol. Sci. Technol. 108 (2013) 14–21.

[3] J. Mitchell, T.C. Chandrasekera, D.J. Holland, L.F. Gladden, E.J. Fordham, Magnetic resonance imaging in laboratory petrophysical core analysis, Phys. Rep. 526 (2013) 165-225.

[4] O.V. Petrov, G. Ersland, B.J. Balcom, T_2 distribution mapping profiles with phase encode MRI, J. Magn. Reson. 209 (2011) 39–46.

[5] B.J. Balcom, R.P. MacGregor, S.D. Beyea, D.P. Green, R.L. Armstrong, T.W. Bremner. Single-point ramped imaging with T_1 enhancement. J. Magn. Reson. Series A 123 (1996) 131-134.

[6] L. Li, H. Han, B.J. Balcom. Spin echo SPI methods for quantitative analysis of fluids in porous media. Journal of Magnetic Resonance 198 (2009) 252-260.

[7] D.I. Hoult, The NMR receiver: A description and analysis of design, Prog. NMR. Spec. 12 (1978) 41-77.

[8] M. Halse, D.J. Goodyear, B. MacMillan, P. Szomolanyi, D. Matheson, B.J. Balcom, Centric scan SPRITE magnetic resonance imaging, J. Magn. Reson. 165 (2003) 219-229.

[9] M.M. Britton, P.M. Bayley, P.C. Howlett, A.J. Davenport, M. Forsyth, *In situ*, real-time visualization of electrochemistry using magnetic resonance imaging, J. Phys. Chem. Lett. 4 (2013) 3019-3023.

[10] Z. Zhang, J. Martin, J. Wu, H. Wang, K. Promislow, B.J. Balcom, Magnetic resonance imaging of water content across the Nafion membrane in an operational PEM fuel cell, J. Magn. Reson. 193 (2008) 259-266.

[11] R. Bhattacharyya, B. Key, H. Chen, A.S. Best, A.F. Hollenkamp, C.P. Grey, *In situ* NMR observation of the formation of metallic lithium microstructures in lithium batteries, Nature Materials 9 (2010) 504-510.

[12] A. Tannús, M. Garwood, Adiabatic pulses, NMR. Biomed. 10 (1997) 423-243.

[13] R.J. Ordidge, A. Connelly, J.A.B. Lohman, Image-Selected *in vivo* Spectroscopy (ISIS). A new technique for spatially selective NMR spectroscopy. J. Magn. Reson. 66 (1986) 283-294.

[14] O.V. Petrov, B.J. Balcom, Local T_2 distribution measurements with DANTE-Z slice selection, J. Magn. Reson. 215 (2012) 109-114.

[15] A.G. Marshall, Fourier, Hadamard, and Hilbert transforms in Chemistry, Plenum press, New York, 1982.

[16] G. Goelman, J.S. Leigh, Hadamard spectroscopic imaging techniques insensitive to pulse imperfections, J. Magn. Reson. 105 (1993) 78-81.

[17] S. Vashaee, B. Newling, B. MacMillan, B.J. Balcom, B_1 mapping with a pure phase encode approach, J. Magn. Reson. 232 (2013) 68-75.

[18] B.J. Balcom, S. Vashaee, B. Newling, B. MacMillan, Methods of radio frequency magnetic field mapping, U.S. Patent, 8,890,527, November 18, 2014.

[19] S. Vashaee, F. Goora, M.M. Britton B. Newling, B.J. Balcom, Mapping B_1-induced near metallic structures in MR images: a comparison of simulation and experiment, J. Magn. Reson. 250 (2015) 17-24.

[20] S. Vashaee, O.V. Petrov, B.J. Balcom, B. Newling, Region of interest selection of long core plug samples by magnetic resonance imaging: profiling and local T_2 measurement, Meas. Sci. Technol. 25 (2014) 035004-0350014.

[21] S. Vashaee, F. Marica, B. Newling, B.J. Balcom, A comparison of magnetic resonance methods for spatially resolved T_2 distribution measurements in porous media, submitted to Meas. Sci. Technol. 26 (2015) 055601-055617.

Chapter 2 - Magnetic Resonance Background

The goal of this chapter is to provide an outline of those aspects of nuclear magnetic resonance (NMR) theory which are fundamental to the experimental methods employed in this thesis. Basic quantum mechanical NMR theory, which has been elaborated in many reference books [1-3], is not repeated here.

2.1 Three magnetic fields

A magnetic resonance (MR) scanner consists of three main hardware components: a main magnet, a magnetic field gradient system and an RF system. This section briefly describes their functional characteristics. The reader is referred to the literature for more discussion [4].

2.1.1 $\mathbf{B_0}$, the main field

An intrinsic property of nuclei with odd atomic weight and/or odd atomic number is that they possess an angular momentum that is referred to as spin and an associated magnetic moment [4]. Normally, the spins are in random directions, creating a net magnetic moment of zero. However, when a static magnetic flux density $\mathbf{B_0}$ is introduced, by convention in the z or longitudinal direction, magnetic moments orient partially parallel or anti-parallel to the field, as explained by quantum physics. The parallel state is a lower energy state, while the anti-parallel state is a higher energy state. Thus, slightly more nuclei align in the parallel state, creating a net magnetic moment for an ensemble of spins (referred to as the net magnetization, $\mathbf{M}$) aligned parallel to $\mathbf{B_0}$ ($+z$), as shown in Fig. 2-1a.

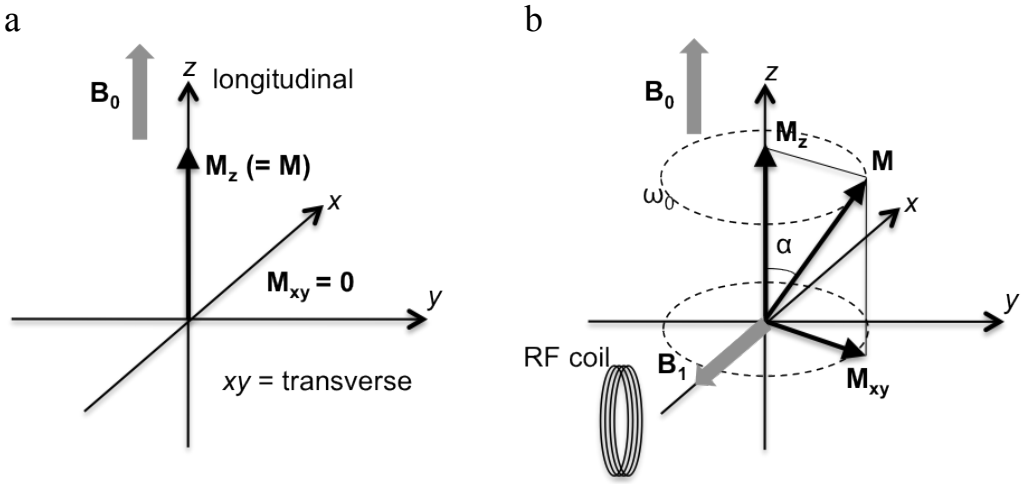

Figure 2-1 (a) Equilibrium condition of magnetization (M) in the presence of the main static magnetic field B_0 (b) B_1 radiofrequency field tuned to the Larmor frequency and applied in the transverse (*xy*) plane rotates the magnetization away from the *z* axis. After cessation of the B_1 excitation, M_{xy} precesses about *z* axis at the Larmor frequency, producing an electromotive force in the receiver coil.

In the presence of field $\mathbf{B_0}$, the angular frequency of the nuclear precession is given by Larmor frequency:

$$\omega_0 = \gamma B_0 \qquad \textbf{(2.1)}$$

where γ is the gyromagnetic ratio (for hydrogen, $\gamma/2\pi$ = 42.57 MHz/T). The equilibrium net magnetization is proportional to the spin density, the number of spins per unit volume and is defined as:

$$\mathbf{M} = M_x\mathbf{i} + M_y\mathbf{j} + M_z\mathbf{k} \qquad \textbf{(2.2)}$$

At equilibrium M is solely in the *z* direction, as shown in Fig. 2-2a. The static magnetic flux density is typically in the range of a few tesla [5]. However, as field density increases, ensuring the field is homogeneous becomes increasingly difficult.

"Shimming", the adjustment of $\mathbf{B_0}$ utilizing small coils or magnets is routinely employed to make the static magnetic flux density more homogeneous.

2.1.2 B_1, the radiofrequency field

A second magnetic field, generated by radio frequency (RF) electromagnetic waves is applied to create observable transverse magnetization. This alternating electromagnetic field, $\mathbf{B_1}$, is tuned to the Larmor frequency and is perpendicular to $\mathbf{B_0}$. The $\mathbf{B_1}$ field applies a torque to the net magnetization vector, causing the net magnetization vector to rotate towards the transverse plane, as shown in Fig. 2-1b. The flip angle α corresponds to the time integral of $B_1(t)$ with the transverse magnetization determined by the resulting angle:

$$\alpha(t) = \gamma \int_{-\frac{t_{pulse}}{2}}^{\frac{t_{pulse}}{2}} B_1(t)\, dt \qquad \textbf{(2.3)}$$

where B_1 is the strength of the applied magnetic field, t_{pulse} is the RF pulse duration and t = 0 is the center of the pulse. The rotation angle can be increased with an increase in pulse duration or an increase in $\mathbf{B_1}$ strength. When the RF pulse ceases, the net magnetization precesses around B_0 and returns to equilibrium along the longitudinal axis.

An RF probe which generates the RF pulse also acts as the receiver coil. The time-varying magnetic flux caused by the rotating sample magnetization establishes an electromotive force in the nearby receiver coil by induction. The RF pulse is typically applied to generate a 90° pulse to rotate sample magnetization into the transverse, *xy*, plane.

If the RF field is inhomogeneous, then the net magnetization vector will be rotated by a different angle at each location in the region of interest (ROI). This causes problems in both excitation and reception. Desirable features of the RF system are a uniform $\mathbf{B_1}$ field and high detection sensitivity [4]. Thus an MR system is equipped with RF coils in different shapes and sizes for different applications. Some examples are solenoid coils, saddle coils, birdcage coils, and surface coils, as shown in Fig. 2-2.

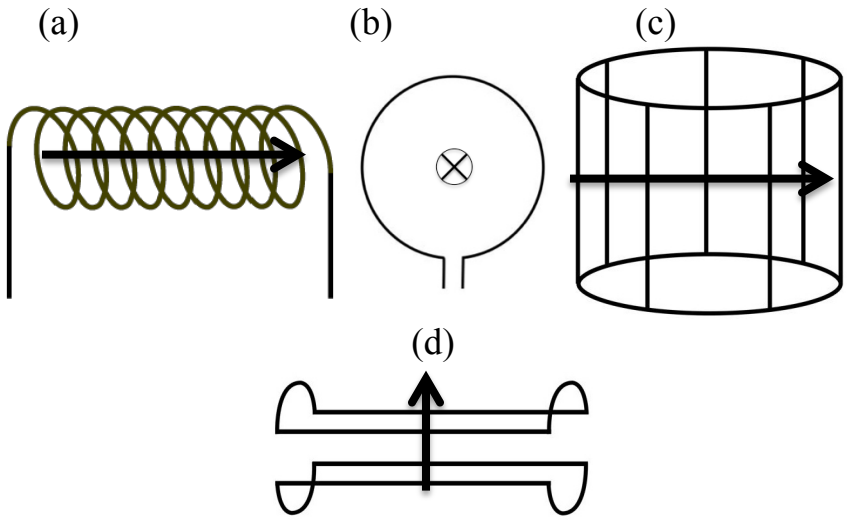

Figure 2-2 Some examples of RF coils. (a) Solenoidal coil, (b) surface coil, (c) birdcage coil, and (d) saddle coil. The arrows show the direction of the B_1 field at the center of the RF probes. ⊗ shows the B_1 direction, pointing into the page.

The arrows show the direction of the $\mathbf{B_1}$ field at the center of the RF probes. Reference [6] shows $\mathbf{B_1}$ field calculations for the above RF coils. There is a direct relationship between the current (I) and B_1 field. Consider a simple circular loop with

radius *a* carryings an electric current I. The $\mathbf{B_1}$ field of the RF coil at any point *P* can be calculated employing the Biot-Savart law:

$$\mathbf{B_1}(\mathbf{r}) = \frac{\mu_0 I}{4\pi}\int_C \frac{d\mathbf{l}\times\mathbf{R}}{R^3} \qquad (2.4)$$

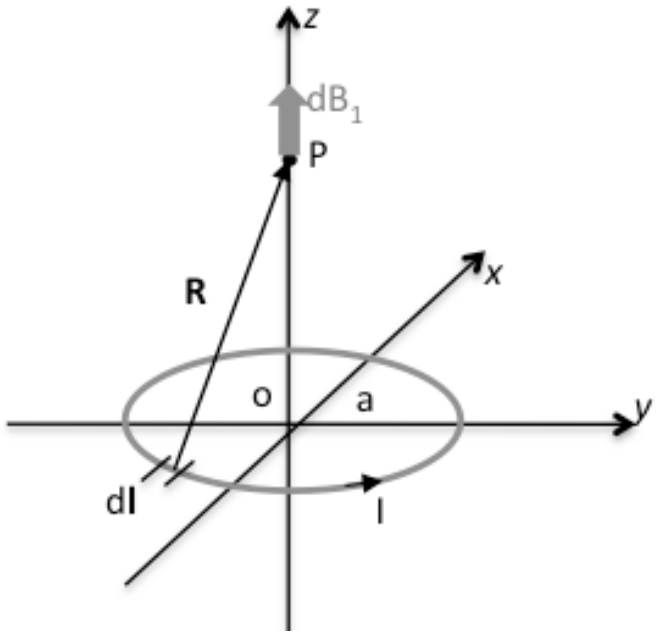

Figure 2-3 Electrical current, I, in a circular loop, with radius *a,* creates a magnetic field. The current element dl produces the field element labeled dB_1 at point P. R and o show the distance from the source element dl to the field point P and the loop center, respectively. The symmetry is such that the B_1 field contributions of all the current elements around the circumference add in the center. The line integral of Eq. (2.4) is the circumference of the circle.

where μ_0 is the permeability of the free space, and vector **R** is the displacement from the source element d**l** to the field point P, as shown in Fig. 2-3. The $\mathbf{B_1}$ field is stronger closer to the current source. If we consider P = (0, 0, *z*), one can show that for a circular loop:

$$\mathbf{B_1}(z) = \frac{\mu_0 I a^2}{2(z^2 + a^2)^{3/2}}\mathbf{k} \qquad (2.5)$$

where **k** is the unit vector along the *z* direction.

At this point it is useful to stress that at the loop center, o = (0, 0,0), $B_1 \propto 1/a$. Hence, an RF probe with smaller radius, *a*, generates stronger $\mathbf{B_1}$ field which also results in higher detection sensitivity as described below.

2.1.2.1 The principle of reciprocity

Consider the magnetic field $\mathbf{B_1}$, produced by a coil *C* carrying an alternating unit current at the Larmor frequency, as shown in Fig. 2-4. The field at point A is much stronger than at point B. Now consider the alternating voltage induced in the same coil by a rotating magnet, first at point A, then removed to point B. Intuitively, one would expect the voltage produced by the magnet at point A to be considerably larger than that generated when the magnet is at point B. At any spatial location, there is a correspondence between the $\mathbf{B_1}$ field strength that would be produced if unit current were to flow in the coil, and the voltage strength induced in the coil by a rotating magnet at that same point [7, 8]. It may be shown that the induced electromotive force (*EMF*) is given by:

$$\zeta = -\left(\frac{\partial}{\partial t}\right)\{\mathbf{B_1} \cdot \mathbf{m}\} \qquad (2.6)$$

where **m** is the magnetic moment. It follows that for a sample of volume V_s, which has been subjected to a 90° pulse, one needs only know the value of $\mathbf{B_1}$ at all points in the

sample to be able to calculate the induced *EMF* in the coil [7, 8]. Thus, if the net magnetization, M_0, for the entire sample lies in the *xy* plane,

$$\zeta = -\int_{sample} \left(\frac{\partial}{\partial t}\right)\{\mathbf{B_1} \cdot \mathbf{M_0}\}\, dV_s \qquad \textbf{(2.7)}$$

The calculation of $\mathbf{B_1}$ is feasible for most RF coils for MR. If $\mathbf{B_1}$ may be considered to be reasonably homogeneous over the sample volume, the calculation is simplified. The integration of Eq. (2.7) gives:

$$\zeta = K\omega_0 B_{1xy} M_0 V_s \cos\omega_0 t \qquad \textbf{(2.8)}$$

where K is an inhomogeneity factor and B_{1xy} is the component of B_1 perpendicular to the main field B_0.

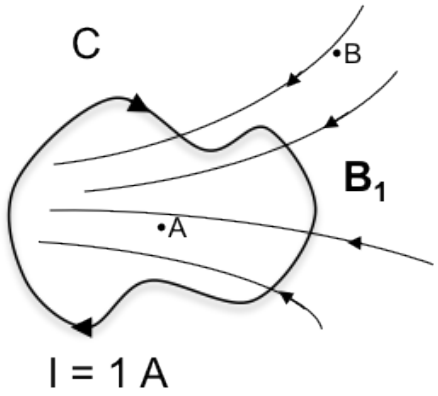

Figure 2-4 The principle of reciprocity. A current of 1A flowing in a coil C produces a field B_1 that is larger at A and smaller at B. A rotating magnet at A induces in the coil an electromotive force ζ which is larger than that induced by the same magnet at point B. The correspondence between ζ and B_1 is known as the principle of reciprocity.

2.1.3 G, the constant magnetic field gradient

A magnetic field gradient superimposed on the static magnetic field, $\mathbf{B_0}$, results in a linear variation in the magnetic field. This causes the resonance frequency to vary as a

function of position. The magnetic field gradient in all three directions can be written in a tensor form [4]. Since the resonance frequency of spins is only affected by the gradient components in the same direction as $\mathbf{B_0}$ (z), thet tensor may be reduced to:

$$\mathbf{G} = G_x\mathbf{i} + G_y\mathbf{j} + G_z\mathbf{k} = \frac{\partial B_z}{\partial x}\mathbf{i} + \frac{\partial B_z}{\partial y}\mathbf{j} + \frac{\partial B_z}{\partial z}\mathbf{k} \qquad \textbf{(2.9)}$$

where ***i***, ***j***, and ***k*** are unit vectors. The overall field can then be expressed as:

$$\mathbf{B}(r) = (B_0 + G_x x + G_y y + G_z z)\mathbf{k} = (B_0 + \mathbf{G}\cdot\mathbf{r})\mathbf{k} \qquad \textbf{(2.10)}$$

By varying the magnetic field gradients, spatial information may be encoded as discussed in section 2.4.

2.2 Relaxation mechanisms

The effect of a resonant RF pulse is to disturb the spin system from thermal equilibrium. A process known as spin-lattice relaxation will restore the z component of magnetization to equilibrium. As the name implies, the process involves an exchange of energy between the spin system and the surrounding thermal reservoir, known as the lattice. Equilibrium is characterized by a state of polarization with magnetization $\mathbf{M_0}$ directed along the longitudinal magnetic field, $\mathbf{B_0}$. The restoration of this equilibrium is therefore alternatively named longitudinal relaxation. The phenomenological description of this process is given by the equation:

$$\frac{dM_z}{dt} = -\frac{(M_z - M_0)}{T_1} \qquad \textbf{(2.11)}$$

where the solution is:

$$M_z(t) = M_z(0)\, e^{-\frac{t}{T_1}} + M_0\left(1 - e^{-\frac{t}{T_1}}\right) \qquad \textbf{(2.12)}$$

where $\mathbf{M_z}$ is the amplitude of the *z* component of the net magnetization and M_0 is the initial net magnetization. $M_z(0)$ is the *z* component of the magnetization immediately after application of an RF pulse and before commencement of longitudinal relaxation. Following a 90° excitation $M_z(0) = 0$; hence:

$$M_z(t) = M_0\left(1 - e^{-\frac{t}{T_1}}\right) \qquad \textbf{(2.13)}$$

The relaxation time T_1 is the time required for the *z* component of **M** to return to 63% of its original value following a 90°excitation pulse [5].

Spin-spin relaxation describes the loss of phase coherence of the nuclei as energy is transferred between nuclei. This results in decay of the *x* and *y* components of the sample magnetization and is governed by the time constant T_2. The phenomenological description of T_2 relaxation is:

$$\frac{dM_{xy}}{dt} = -\frac{M_{xy}}{T_2} \qquad \textbf{(2.14)}$$

where the solution is:

$$M_{xy}(t) = M_{xy}(0)\, e^{-\frac{t}{T_2}} \qquad \textbf{(2.15)}$$

where M_{xy} is the magnitude of the transverse component of the sample magnetization. After a 90° excitation $M_{xy}(0) = M_0$. The relaxation time T_2 is the time required for the transverse component of **M** to decay to 37% of its initial value via irreversible processes.

The manufacturers of MR magnets try to create a homogeneous $\mathbf{B_0}$ field, employing first-, second-, and higher order shim coils for non-uniformity correction. However, it is inevitable that some variation in $\mathbf{B_0}$ occurs across the sample. A free induction decay (FID) signal results following the application of the RF excitation, which decays more rapidly than due T_2 effects alone. The resultant time constant is often labeled T_2^* and is termed the effective transverse lifetime constant:

$$\frac{1}{T_2^*} = \frac{1}{T_2} + \gamma \Delta B_0 \qquad \textbf{(2.16)}$$

T_2^* relaxation depends on T_2, the transverse relaxation time, and ΔB_0, which describes the inhomogeneity of the static magnetic field.

Another form of MR signal is known as an echo. A feature, which distinguishes an echo signal from an FID signal, is the symmetry of the echo signal, which results from rephasing of M_{xy} followed by dephasing of M_{xy}. An echo is produced by employing multiple RF pulses. These signals, called spin echoes (SE), were discovered by Erwin L. Hahn in 1950. A simple two-pulse excitation scheme consists of a 90° pulse followed by a time delay τ and then a 180° pulse (90°- τ -180°- τ). After a period of time, τ, following the applied 180° RF pulse, the components of the transverse magnetization rephase and form SE.

It is possible to measure multiple successive spin echoes with multiple pulse methods. One example is the Carr-Purcell measurement which begins with a 90° pulse followed by a series of 180° pulses. The initial 90° pulse rotates the magnetization vector into the transverse plane. The first 180° pulse is applied after a time τ, and inverts the

phase of the magnetization as it loses coherence. After a time 2τ, following the 90° pulse, a SE is generated. The transverse magnetization loses phase coherence once more, but can be regained with another 180° pulse. Therefore, a train of 180° pulses creates a train of spin echoes that form halfway between the 180° pulses. The magnitude of the spin echoes decays with relaxation time T_2, so T_2 can be determined through:

$$M_{xy} = M_0 \, e^{-\frac{2n\tau}{T_2}} \qquad \textbf{(2.17)}$$

where 2τ is the time between two successive 180° pulses and *n* is the number of echoes collected. In practice, the 180° pulses are phase shifted to minimize artifacts caused by successive imperfect 180° pulses. This modification was proposed by Meiboom and Gill and is therefore known as the Carr-Purcell-Meiboom-Gill (CPMG) sequence [4].

T_2 can be extracted from the CPMG decay by non-linear least square fitting providing a discrete number of T_2 components. It is common practice in petrophysics to fit a distribution of exponential decays employing an Inverse Laplace Transform (ILT) [9].

The principal concern in this thesis is high quality measurements of the T_2 distribution of the pore fluid and access to short T_2s spatially resolved. The ILT approach imposes a smooth distribution that may not be physically correct in some instances. A single exponential decay processed by ILT will yield a symmetrical T_2 distribution in log space, with a width that is not physical. The T_2 distribution shape is not calibrated and not over-interpreted in this work. The interpretation is only based on changes in T_2 distributions (employing bulk CPMG as a control) rather than an absolute interpretation.

2.3 The Bloch equations

The behavior of the spin ensemble may be explained classically in the majority of MRI measurements. Equating the torque to rate of change of the sample magnetization:

$$\frac{d\mathbf{M}}{dt} = \mathbf{M} \times \gamma \mathbf{B_0} \qquad \textbf{(2.18)}$$

When **M** and $\mathbf{B_0}$ are not coaxial, the torque (being orthogonal to both $\mathbf{B_0}$ and **M**) forces a precession of **M** about the *z*-axis, at the Larmor frequency of Eq. (2.1).

The $\mathbf{B_1}$ field effect may similarly be treated classically. The effect of the B_1 field is made clearer by a transformation of the coordinate system to a frame of reference that rotates at the Larmor frequency. Consider an RF pulse applied orthogonal to $\mathbf{B_0}$ that defines the *x*-axis of our first coordinate frame:

$$\mathbf{B}_{rf} = 2B_1 \cos(\omega_1 t)\mathbf{i} \qquad \textbf{(2.19)}$$

$\mathbf{B_{rf}}$ may be expressed as the sum of two counter-rotating components:

$$\mathbf{B}_{rf} = B_1\left[\cos(\omega_1 t)\mathbf{i} + \sin(\omega_1 t)\mathbf{j}\right] + B_1\left[\cos(\omega_1 t)\mathbf{i} - \sin(\omega_1 t)\mathbf{j}\right] \qquad \textbf{(2.20)}$$

one rotating in the same direction as the Larmor precession, and the other in the opposite direction. The component rotating in the opposite direction has negligible interaction with M, as their relative frequency offset is large ($\omega_0 + \omega_1$) and, for all MRI applications described herein, $\mathbf{B_1} << \mathbf{B_0}$.

The interaction of $\mathbf{B_{rf}}$ and **M** is simplified by transforming the coordinate system to one rotating at ω_0 about $\mathbf{B_0}$ (Fig. 2-5). The apparent static field in the rotating

coordinate frame is $(B_0 + \omega_0/\gamma)\ \mathbf{k} = 0$. The only torque on **M** is caused by the RF field, and the counter-rotating component of that field becomes:

$$B_1\left[\cos\left(\left\{\omega_1 - \omega_0\right\}t\right)\mathbf{i}' + \sin\left(\left\{\omega_1 - \omega_0\right\}t\right)\mathbf{j}'\right] \qquad \textbf{(2.21)}$$

where prime quantities are in the rotating coordinate system. For on-resonance RF pulse application, $\omega_0 = \omega_1$ and thus $\mathbf{B_{rf}} = \mathbf{B_1} = B_1\mathbf{i'}$. In analogy to Eq. (2.18):

$$\frac{d\mathbf{M}}{dt} = \mathbf{M} \times \gamma\mathbf{B}_1 \qquad \textbf{(2.22)}$$

The evolution of **M** under the application of on-resonance RF excitation is a simultaneous precession about $\mathbf{B_0}$ and $\mathbf{B_1}$ at ω_0 and ω_1 (Fig. 2-5b). The motion is simply a precession about **i'**, in the rotating coordinate system (Fig. 2-5d). The latter description provides a convenient means of categorization for RF pulse application by the precession angle, $\alpha = \gamma B_1 t_{pulse}$, t_{pulse} is the RF pulse duration. A 90° RF pulse, applied to the spin system at equilibrium, has sufficient RF field strength and duration that the resultant magnetization lies solely in the *x'y'*-plane and a 180° RF pulse results in $\mathbf{M} = -M_0\,\mathbf{k}$. In general the components of magnetization after application of $\mathbf{B_{rf}} = 2B_1\cos(\omega_1 t)\ \mathbf{i}$ to $\mathbf{M_0} = M_0\,\mathbf{k}$ are:

$$\begin{aligned} M_{x'} &= 0 \\ M_{y'} &= M_0 \sin\alpha \\ M_{z'} &= M_0 \cos\alpha \end{aligned} \qquad \textbf{(2.23)}$$

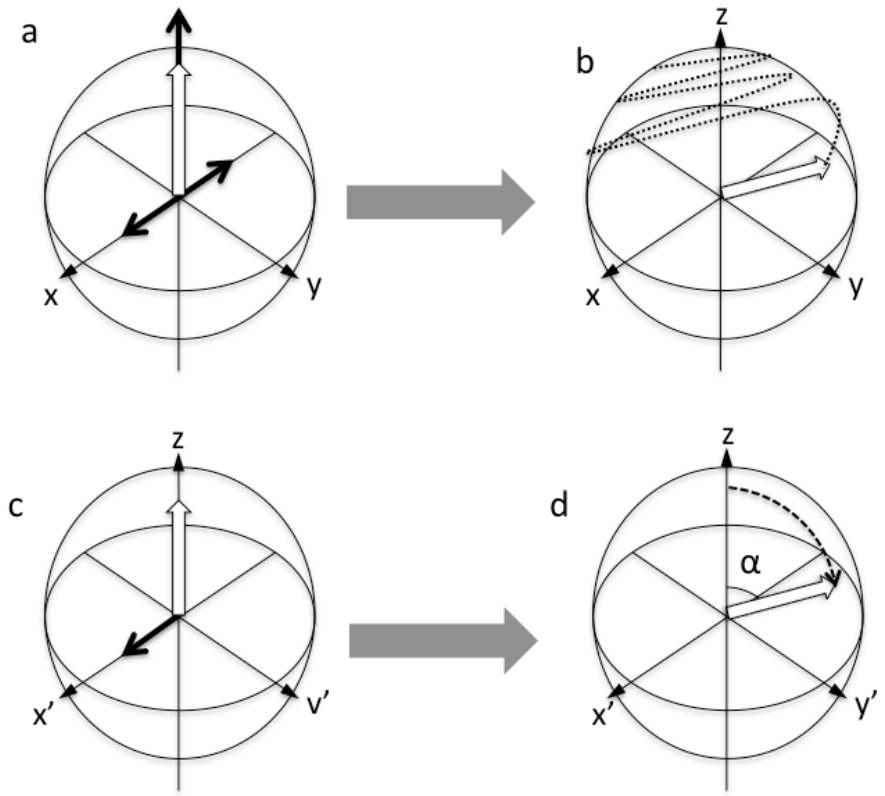

Figure 2-5 (a) The application of a static magnetic field B_0 (vertical bold arrow), and an RF field (along the *x* axis), oscillating at ω_0, causes (b) the ensemble magnetization simultaneously to precess about both fields. (c) In a coordinate system rotating at ω_0, the apparent longitudinal field is zero and the static RF field defines the *x'* axis. Precession (d) is simply a rotation about the *x'* axis.

Relaxation time effects may be combined with Eq. (2.18) or Eq. (2.22), to refine the classical description of spin behavior. The resulting relations are known as the Bloch equations:

$$\frac{dM_x}{dt} = \gamma(\mathbf{M} \times \mathbf{B}_{eff})_x - \frac{M_x}{T_2}$$
$$\frac{dM_y}{dt} = \gamma(\mathbf{M} \times \mathbf{B}_{eff})_y - \frac{M_y}{T_2} \qquad \textbf{(2.24)}$$
$$\frac{dM_z}{dt} = \gamma(\mathbf{M} \times \mathbf{B}_{eff})_z + \frac{M_0 - M_z}{T_1}$$

$\mathbf{B_{eff}}$, the effective magnetic field, is the vector sum of $\mathbf{B_0}$ and $\mathbf{B_{rf}}$ and, when it is used in the rotating coordinate system [2, 4, 10]:

$$\mathbf{B}_{eff} = \left(B_0 - \frac{\omega_1}{\gamma} \right) \mathbf{k'} + B_1 \mathbf{i'} \qquad \textbf{(2.25)}$$

Invoking the on-resonance condition ($\omega_0 = \omega_1$), Eq. (2.25) yields $\mathbf{B_{eff}} = B_1\mathbf{i'}$.

2.4 Spatial encoding

Spatial information may be encoded in MR using either frequency or phase encoding techniques. Both methods require the addition of magnetic field gradients, such that the *z* component of the static magnetic field varies as a function of the Cartesian coordinates. Each method is discussed in the following subsections. The concept of *k*-space provides a connection between spatially encoded measured data, the Fourier transform, and the resulting MR image.

2.4.1 Frequency encoding

The addition of a magnetic field gradient in addition to the static magnetic field across a sample results in the Larmor frequency being a linear function of position:

$$\omega(\mathbf{r}) = \gamma B_0 + \gamma \mathbf{G} \cdot \mathbf{r} \qquad \textbf{(2.26)}$$

where **G** denotes the applied magnetic field gradient and **r** denotes the spatial position [1]. The resulting FID generated from the spins for a given interval d**r** at point **r** , denoted ρ(**r**), is :

$$dS(\mathbf{r},t) \propto \rho(\mathbf{r})\, e^{\left[-i\gamma(B_0+\mathbf{G}\cdot\mathbf{r})t\right]} d\mathbf{r} \qquad \textbf{(2.27)}$$

where i = √-1. The proportionality is partially due to the overall signal dependence on the resulting flip angle of the transverse magnetization into the transverse plane. Neglecting the effect of the flip angle and assuming equality of units on both sides of the equations simplifies Eq. (2.27) to:

$$dS(\mathbf{r},t) = \rho(\mathbf{r})\, e^{\left[-i\gamma(B_0+\mathbf{G}\cdot\mathbf{r})t\right]} d\mathbf{r} \qquad \textbf{(2.28)}$$

It is evident from Eq. (2.28) that the resulting signal frequency, defined by γ (B_0+**G.r**), varies linearly as a function of position. Hence, the applied magnetic field gradient **G** is called a frequency-encoding gradient. The resulting signal from the entire object in the presence of the gradient is:

$$\begin{aligned} S(t) &= \int_{-\infty}^{\infty} \rho(\mathbf{r})\, e^{\left[-i\gamma(B_0+\mathbf{G}\cdot\mathbf{r})t\right]} d\mathbf{r} \\ &= \left[\int_{-\infty}^{\infty} \rho(\mathbf{r})\, e^{\left[-i\gamma(\mathbf{G}\cdot\mathbf{r})t\right]} d\mathbf{r}\right] e^{-i\omega_0 t} \end{aligned} \qquad \textbf{(2.29)}$$

The term $e^{-i\omega_0 t}$ is considered as a carrier signal [1]. Demodulation of the resulting MR signal results in:

$$S(t) = \int_{-\infty}^{\infty} \rho(\mathbf{r})\, e^{\left[-i\gamma(\mathbf{G}\cdot\mathbf{r})t\right]} d\mathbf{r} \qquad \textbf{(2.30)}$$

The frequency-encoded signal from Eq. (2.30) can be rewritten as:

$$S(\mathbf{k}) = \int_{-\infty}^{\infty} \rho(\mathbf{r}) e^{[-i2\pi(\mathbf{k}\cdot\mathbf{r})]}\, d\mathbf{r} \qquad \textbf{(2.31)}$$

Where:

$$\mathbf{k} = \frac{\gamma}{2\pi}\mathbf{G}t \qquad \textbf{(2.32)}$$

From the relationship between **G** and **k**, it is apparent that the frequency-encoding gradient **G** can be used to map a time domain signal to a corresponding *k*-space signal. This results in the spatial information about a sample being uniquely encoded.

2.4.2 Phase encoding

The signal may be alternatively mapped in *k*-space by employing phase encoding. In phase encoding, the value of **k** is fixed by a given gradient **G** and phase encode time t_p, as shown in the following equation:

$$\mathbf{k} = \frac{\gamma}{2\pi}\mathbf{G}t_p \qquad \textbf{(2.33)}$$

The resulting signal from the entire object in the presence of the gradient is:

$$S(t) = \left[\int_{-\infty}^{\infty} \rho(\mathbf{r}) e^{-i\gamma(\mathbf{G}\cdot\mathbf{r})t_p}\, d\mathbf{r}\right] e^{-i\omega_0 t} \qquad \textbf{(2.34)}$$

where the $e^{-i\omega_0 t}$ term represents the carrier frequency and will be removed after demodulation. The magnetic field gradients applied along each of the three Cartesian axes (G_x, G_y, G_z) result in the possibility of three-dimensional imaging.

In general, the applied phase encode gradient varies as a function of time. Letting this time varying phase encode gradient be denoted $\mathbf{G_{phase}}(t)$, the resulting value of **k**:

$$\mathbf{k} = \frac{\gamma}{2\pi}\int_0^{t_p} \mathbf{G_{phase}}(t)dt \qquad (2.35)$$

Therefore, only the area of applied gradient is of importance for spatial encoding and mapping the time domain signal to space.

2.5 Slice selection

To selectively excite spins in a slice, two things are essential: a magnetic field gradient and a shaped RF pulse. Both are discussed in this section.

2.5.1 Slice selective magnetic field gradients

It is necessary to apply a magnetic field gradient during the excitation period for slice selection. An RF pulse is only frequency selective, and spins at different spatial locations are excited in the same way if they resonate at the same frequency. To make an RF pulse spatially selective, it is necessary to make the spin resonance frequency position-dependent. A simple way to achieve this is to augment the homogeneous $\mathbf{B_0}$ field with a constant magnetic field gradient during the excitation period. Such a magnetic field gradient is called a slice selective gradient, $\mathbf{G}_{ss}$, in order to distinguish it from a phase encoding gradient or frequency encoding gradient. Recall from section 2.1.3 that a constant magnetic field gradient is by definition a magnetic field that points along the *z* direction but has amplitude varying linearly along a particular gradient direction [4]. The slice selective gradient is denoted as:

$$\mathbf{G}_{ss} = (G_x, G_y, G_z) = G_{ss}\boldsymbol{\mu}_G \qquad \textbf{(2.36)}$$

where $\boldsymbol{\mu}_G$ specifies the slice selective magnetic field gradient direction and $\boldsymbol{G}_{ss} = \sqrt{G_x^2 + G_y^2 + G_z^2}$ is the overall magnetic field gradient strength.

2.5.2 Slice selective RF pulses

One should translate the desired frequency selectivity, established by the slice selective gradient, to the temporal waveform of an RF pulse. An amplitude modulated RF pulse is characterized by an excitation frequency ω_{rf} and an envelope function $B_1^e(t)$ as:

$$B_1(t) = B_1^e(t)\, e^{-i\omega_{rf}t} \qquad \textbf{(2.37)}$$

in which ω_{rf} and $B_1^e(t)$ should be determined [4].

2.5.2.1 The Fourier Transform approach to selective RF pulse design

Consider the case shown in Fig. 2-6. It is convenient to define a spatial selection function as:

$$p(z) = \prod\left(\frac{z - z_0}{\Delta z}\right) = \begin{cases} 1 & |z - z_0| < \dfrac{\Delta z}{2} \\ 0 & \text{otherwise} \end{cases} \qquad \textbf{(2.38)}$$

which is a "boxcar" function of width Δz centered at $z = z_0$. The necessary slice selection gradient is:

$$\mathbf{G}_{ss} = (0, 0, G_z) \qquad \textbf{(2.39)}$$

The Larmor frequency at z is given by:

$$\omega(z) = \omega_0 + \gamma G_z z \qquad \textbf{(2.40)}$$

or:

$$f(z) = f_0 + \frac{\gamma}{2\pi} G_z z \qquad \textbf{(2.41)}$$

The desired frequency selection function is:

$$p'(f) = p\left(\frac{2\pi f}{\gamma G_z}\right) = \prod\left(\frac{f - f_c}{\Delta f}\right) \qquad \textbf{(2.42)}$$

where:

$$f_c = f_0 + \frac{\gamma}{2\pi} G_z z_0 \qquad \textbf{(2.43)}$$

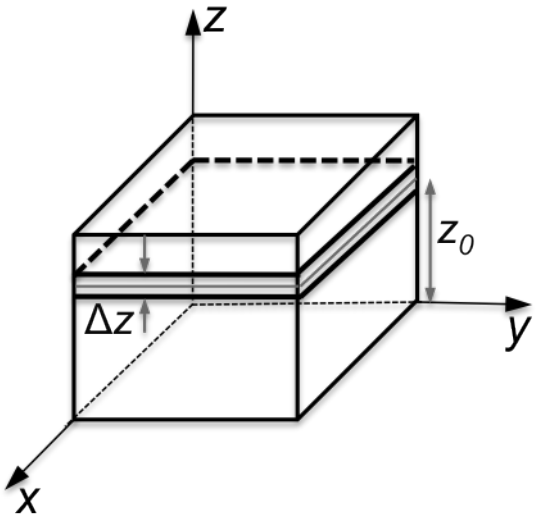

Figure 2-6 slice selected along the z axis. The corresponding slice equation is given in Eq. (2.38). z_0 is the displacement of the slice from the origin and Δz is the slice thickness.

and

$$\Delta f = \frac{\gamma}{2\pi} G_z \Delta z \qquad \textbf{(2.44)}$$

With $p'(f)$, one can determine the necessary excitation function $B_1(t)$.The assumption of Fourier Transform approach is:

$$B_1(t) \propto \int_{-\infty}^{\infty} p'(f)\, e^{-i2\pi ft} df \qquad \textbf{(2.45)}$$

Inserting Eq. (2.43) into Eq. (2.46) and employing:

$$\operatorname{sinc}(\pi at) \leftrightarrow \frac{1}{a} \prod\left(\frac{f}{a}\right) \qquad \textbf{(2.46)}$$

yields:

$$B_1(t) \propto \Delta f \operatorname{sinc}(\pi \Delta f t) e^{-i2\pi f_c t} \qquad \textbf{(2.47)}$$

Comparing the above equation to Eq. (2.37):

$$\omega_{rf} = 2\pi f_c = \omega_0 + \gamma G_z z_0 \qquad \textbf{(2.48)}$$

the pulse envelope function is:

$$B_1^e(t) = A \operatorname{sinc}(\pi \Delta f t) \qquad \textbf{(2.49)}$$

The constant, A, is determined by the desired flip angle. Assume that the pulse is symmetric about the time point $t = t_{pulse}/2$, the pulse envelope function in Eq. (2.43) can be modified to give:

$$B_1^e(t) = A\,\mathrm{sinc}\left[\pi\,\Delta f\left(t - \frac{t_{pulse}}{2}\right)\right], \quad 0 \le t \le t_{pulse} \qquad \textbf{(2.50)}$$

2.5.2.2 The Bloch equation approach to selective RF pulse design

The resulting envelope function yielded from the Fourier approach is not accurate because the spin system behaves nonlinearly during the excitation. One has to resort to the Bloch equations to generate more accurate RF pulses [4]. Ignoring spin relaxation effects during the excitation period, one can write the Bloch equation in the rotating frame:

$$\frac{d\mathbf{M}(z,t)}{dt} = \gamma\mathbf{M}(z,t) \times \mathbf{B}_{eff}(z,t) \qquad \textbf{(2.51)}$$

where:

$$\mathbf{B}_{eff}(t) = B_1^e(t)\mathbf{i}' + \left(B_0 + G_z z - \frac{\omega_{rf}}{\gamma}\right)\mathbf{k}' \qquad \textbf{(2.52)}$$

Setting the RF excitation frequency ω_{rf} to the Larmor frequency of the central slice (Eq. (2.49), We have:

$$\mathbf{B}_{eff}(t) = B_1^e(t)\mathbf{i}' + G_z(z - z_0)\mathbf{k}' \qquad \textbf{(2.53)}$$

Rewriting Eq. (2.46) in scalar form:

$$\begin{aligned}
\frac{dM_{x'}(z,t)}{dt} &= \gamma G_z(z - z_0)M_{y'}(z,t) \\
\frac{dM_{y'}(z,t)}{dt} &= -\gamma G_z(z - z_0)M_{x'}(z,t) + \gamma B_1^e M_{z'}(z,t) \qquad \textbf{(2.54)} \\
\frac{dM_{z'}(z,t)}{dt} &= -\gamma B_1^e M_{y'}(z,t)
\end{aligned}$$

The above equations must be solved numerically. A number of algorithms have been proposed for this task [4].

Many slice selective RF pulses, in practical use, give better selection profiles than the popular sinc pulse. One complicated example is the hyperbolic secant pulse of general form:

$$B_1^e(t) = B_1 \mathrm{sech}(\beta t)^{1+i\mu} \qquad \textbf{(2.55)}$$

This pulse is insensitive to B_1 inhomogeneities and is particularly useful for slice selective spin inversion [4, 11 12]. A detailed discussion of hyperbolic secant pulses follows Chapter 5 of this thesis.

2.6 References

[1] P.T. Callaghan. Principles of nuclear magnetic resonance microscopy. Oxford University Press, Oxford, 1991.

[2] A. Abragam. The principles of nuclear magnetism. Oxford University Press, Oxford, 1 edition, 1960.

[3] M. Goldman. Quantum description of high-resolution NMR in liquids. Oxford University Press, New York, 1988.

[4] Z.P. Liang and P.C. Lauterbur, Principles of magnetic resonance imaging, a signal processing perspective. IEEE Press, 2000.

[5] D.G. Nishimura. Principles of magnetic resonance imaging. Self published, printed by lulu.com, 2010.

[6] J. Mispelter, M. Lupu, A. Briquet, NMR probeheads for biophysical and biomedical experiments, Theoretical principles & practical guidelines, Imperial College Press, London, 2006.

[7] D.I. Hoult, R.E. Richards, The signal to noise ratio of the nuclear magnetic resonance experiment, J. Magn. Reson. 24 (1976) 71-85.

[8] C.N. Chen, D.I. Hoult, Biomedical magnetic resonance technology, Adam Hilger, Bristol, 1989.

[9] J. B. Butler, J. A. Reeds, S. V. Dawson, Estimating Solutions of First Kind Integral Equations with Nonnegative Constraints and Optimal Smoothing, SIAM J. Numer. Anal., 18(1981) 381–397.

[10] R. Freeman. A handbook of nuclear magnetic resonance. 2nd ed. England: Addison Wesley Longman, 1997.

[11] M.A. Bernstein, K.F. King, X.J. Zhou, Handbook of MRI pulse sequences, Elsevier Academic Press, London, UK, 2004.

[12] A. Tannús, M. Garwood, Adiabatic pulses, NMR. Biomed. 10 (1997) 423-243.

Chapter 3 - B_1 Mapping with a Pure Phase Encode Approach: Quantitative Density Profiling

We frequently observe centric scan SPRITE images are very non-uniform for a nominally uniform sample. This chapter shows the non-uniformities over the images are due to B_1 inhomogeneity in the sample space. The B_1 inhomogeneity prevents quantitative density profiling of porous media. Quantitative density profiling is very critical for measurement of fluids in in pore spaces and it is important to be able to measure the B_1 inhomogeneity in order to mitigate its effects. This Chapter discusses a newly developed B_1 mapping technique based on pure phase encode centric scan SPRITE. The B_1 maps are also employed to correct B_1 non-uniformities over the centric scan SPRITE images.

This chapter is largely based on the paper "B_1 mapping with a pure phase encode approach: quantitative density profiling" published in the Journal of Magnetic Resonance, 232 (2013) 68-75. The format of references in this chapter follows that of the original article. The paper was the basis of a related patent "Methods of radio frequency magnetic field mapping", U.S. Patent, 8,890,527, awarded November 18, 2014.

Abstract

In MRI, it is frequently observed that naturally uniform samples do not have uniform image intensities. In many cases this non-uniform image intensity is due to an inhomogeneous B_1 field. The 'principle of reciprocity' states that the received signal is proportional to the local magnitude of the applied B_1 field per unit current. Inhomogeneity in the B_1 field results in signal intensity variations that limit the ability of MRI to yield quantitative information. In this paper a novel method is described for

mapping B_1 inhomogeneities based on measurement of the B_1 field employing centric-scan pure phase encode MRI measurements. The resultant B_1 map may be employed to correct related non-uniformities in MR images.

The new method is based on acquiring successive images with systematically incremented low flip angle excitation pulses. The local image intensity variation is proportional to B_1^2, which ensures high sensitivity to B_1 field variations. Pure phase encoding ensures the resultant B_1 field maps are free from geometry distortions caused by susceptibility variation, chemical shift and paramagnetic impurities. Hence, the method works well in regions of space that are not accessible to other methods such as in the vicinity of conductive metallic structures, including the RF probe itself.

Quantitative density images result when the centric scan pure phase encode measurement is corrected with a relative or absolute B_1 field map. The new technique is simple, reliable and robust.

3.1 Introduction

Magnetic resonance imaging is commonly employed for clinical diagnostic imaging but its routine application to spatially resolved analysis of fluids in porous media is still developing. Recent developments in quantitative MRI of reservoir rock core plugs have led to the development of new core analysis methods for capillary pressure and other petro-physical parameters [1-4]. The essential element in quantitative MRI of such systems is a reliable measure of fluid quantity in the pore space. Quantitative imaging is impaired in many cases by non-uniform B_1 fields in the sample space.

According to the 'principle of reciprocity' [5,6], the received MR signal for each point in space is proportional to the local B_1 field strength per unit excitation current. The spatial variation of the RF field sensitivity for excitation and reception is one principal reason for non-uniform images of nominally uniform samples. Non-uniformities across the MRI image will affect the image-based quantification and interpretation of porous media properties.

One may solve the B_1 inhomogeneity problem by limiting the sample space in a larger RF probe [7] but this is not a very good utilization of the experimental sample space that is costly and at a premium. In quantitative MRI one solution is to measure a B_1 map and correct the intensity inhomogeneities that arise from B_1 variation [8-15].

Mapping of the B_1 field can be undertaken with a variety of MRI-based methods. With double angle techniques [14, 16, 17] B_1 maps are acquired by measurement of the magnitude of the signal after α and 2α excitations. The imaging technique is usually based on spin echo imaging or echo planar imaging. Another method is based on the acquisition of a spin echo and a stimulated echo and the local B_1 is determined by the ratio of images [18]. The actual flip angle imaging (AFI) method employs FLASH imaging [19] with the interleaved acquisition of two echoes, applying the same flip angle but for different repetition times [20, 21]. The phase sensitive method for B_1 mapping employs a series of RF pulses that generate a transverse magnetization whose phase is a function of the flip angle [22]. In another method that is based on gradient echo imaging with large excitation angles, signal intensity variations are produced by employing flip angles that are distributed around 180° [23]. B_1 mapping employing the Bloch-Siegert shift [24, 25] has recently been introduced; it encodes the B_1 information into the signal

phase by irradiating with an off-resonance RF pulse following conventional spin excitation. Nagashima has recently employed a nutation-based experiment to find 1D B_1 profiles in a spectroscopy RF probe [26].

The B_1 mapping method presented in this work is based on measurements of image intensities acquired with a series of low flip angle excitation pulses employing centric scan SPRITE [27-29]. Centric scan SPRITE MRI is employed for spin-density measurements of porous media due to its innate reliability and immunity to image distortions caused by susceptibility variation, chemical shift and paramagnetic impurities. The SPRITE signal in each pixel (or voxel) is proportional to B_1^2 due to B_1 sensitivity in both excitation and reception. The B_1^2 sensitivity makes the method very sensitive to B_1 variation in the sample space. This sensitivity to local B_1^2, with a low flip angle excitation pulse was first discussed by Hoult [7] but he did not pursue B_1 mapping and it seems the idea was not pursued in the literature.

As a pure phase encode method, the B_1 mapping procedure presented will work well even in the presence of conductive structures that support eddy currents. The new B_1 mapping technique may be employed to determine the B_1 map in the vicinity of RF probe structures. B_1 mapping methods based on frequency encoding, essentially all the above referenced methods, will often suffer from B_0 inhomogeneity artifacts. Many of these literature methods may be undertaken with pure phase encoding to solve this problem, but it is not common practice.

Many methods have been developed to correct non-uniform MRI images due to B_1 inhomogeneity [8-15, 30-35]. In this work a simple method is proposed for correcting B_1 inhomogeneity effects employing B_1 field maps. Corrected SPRITE images result

from dividing the original image by relative maps of B_1^2 [8]. This method permits correction of non-uniformities due to excitation and reception and the intensity of the corrected image represents the sample distribution. If one knows how the image intensity depends on B1 field strength for other commonly employed MRI experiments, the image may be corrected through knowledge of absolute B_1 maps [34]. The new B_1 mapping technique is readily translated to both high field and low field systems.

The B_1 mapping methods outlined, with associated B_1 correction of SPRITE density images are simple, robust and reliable with facile data handling and data manipulation. Because the method requires acquisition of six to eight discrete images it will however be slower than many B_1 mapping methods in the literature.

3.2 Theory

3.2.1 B_1 mapping methodology

The transverse magnetization M_{xy} at any point **r**, generated by a centric scan SPRITE imaging sequence [27-29], free from T_1 weighting, is given by the following equation:

$$M_{xy}(\mathbf{r}) = M_0(\mathbf{r})\exp(-\frac{t_p}{T_2^*})\sin\alpha \qquad \textbf{(3.1)}$$

Where $M_0(\mathbf{r})$ is the local equilibrium longitudinal magnetization proportional to the quantity of material, t_p is the phase encoding time between RF excitation and signal reception and α is the RF pulse flip angle, and T_2^* is the effective spin-spin relaxation time. If the sequence parameters satisfy $t_p << T_2^*$ the transverse magnetization is directly proportional to $M_0(\mathbf{r})$.

Employing the 'principle of reciprocity' [5,6] the received signal S_{local} from precessing nuclei in a small volume δV centered at any point **r** in the RF probe is proportional to:

$$S_{local}(\mathbf{r}) \propto B_{1xy}(\mathbf{r}) M_{xy}(\mathbf{r}) \qquad \textbf{(3.2)}$$

Where $B_{1xy}(\mathbf{r})$ is the component of the RF field produced in the transverse plane at the location of the sample by unit current in the coil during excitation.

The product of the gyromagnetic ratio γ, the B_{1xy} field strength, and excitation pulse length t_{pulse} gives the RF flip angle in Eq. (3.1). The local image intensity from Eqs. (3.1) and (3.2) with the above statement of the RF flip angle becomes:

$$S_{local}(\mathbf{r}) \propto B_{1xy}(\mathbf{r})\, M_0(\mathbf{r}) \exp(-\frac{t_p}{T_2^*}) \sin(\gamma B_{1xy}(\mathbf{r}) t_{pulse}) \qquad \textbf{(3.3)}$$

where the factor $B_{1xy}(\mathbf{r})$, introduced as part of Eq. (3.2) is related to signal reception through the 'principle of reciprocity' [5,6], the sine factor of is $B_{1xy}(\mathbf{r})$ related to excitation and of course the overall signal scales with $M_0(\mathbf{r})$.

The new technique for B_1 mapping is based on mapping the image intensity variation in each pixel that results from increment of the excitation flip angle in successive images. In the case of low flip angles $\sin\alpha \approx \alpha$, and Eq. (3.3) reduces to Eq. (3.4) with a direct dependence of signal on $B^2_{1xy}(\mathbf{r})$.

$$S_{local}(\mathbf{r}) \propto M_0(\mathbf{r}) \exp(-\frac{t_p}{T_2^*})\, \gamma B_{1xy}^2(\mathbf{r}) t_{pulse} \qquad \textbf{(3.4)}$$

Eq. (3.5) is a simple modification of Eq. 4. $S_{local}(\mathbf{r})$ is unitless in image space and a constant of proportionality κ is introduced to make the relationship of Eq. (3.4) an equality. The factor $\rho_0(\mathbf{r})$ introduced as part of Eq. (3.5), considered as grams per unit volume of ^{1}H material at any point $\mathbf{r}$ replaces $M_0(\mathbf{r})$ to simplify the units. To simplify the expression, $B_{1xy}(\mathbf{r})$ is replaced by $B_1(\mathbf{r})$.

Practical measurement of the local B_1 proceeds via Eq. (3.5) by incrementing t_{pulse} in successive images, employing a homogeneous phantom and maintaining the low flip angle limit. Plotting local signal versus t_{pulse} permits determination of B_1^2 via the slope.

$$S_{local}(\mathbf{r}) = \kappa\rho_0(\mathbf{r})\exp(-\frac{t_p}{T_2^*})\gamma B_1^2(\mathbf{r})t_{pulse} \qquad \textbf{(3.5)}$$

3.2.2 Relative B_1 map generation employing a homogeneous phantom

For a B_1 mapping experiment performed with a homogeneous phantom, $\kappa\rho_0\exp(-t_p/T_2^*)$ in Eq. (3.5) can be considered constant. The ratio of slopes, *m* and *m'* from Eq. (3.5), measured at two different physical locations (*x,y,z*) and (*x',y',z'*) will be simply equal to the ratio of B_1^2.

$$\frac{m}{m'} = \frac{(\kappa\rho_0\exp(-\frac{t_p}{T_2^*}))\gamma B_1^2(x,y,z)}{(\kappa\rho_0\exp(-\frac{t_p}{T_2^*}))\gamma B_1^2(x',y',z')} = \frac{B_1^2(x,y,z)}{B_1^2(x',y',z')} \qquad \textbf{(3.6)}$$

Consequently one can determine relative B_1 maps by determination of relative slopes:

$$\frac{m_{local}}{m_{\max}} = \left(\frac{B_{1local}}{B_{1\max}}\right)^2 \qquad \textbf{(3.7)}$$

where m_{max} is the highest slope in the measurement where the local B_1 field has the maximum value, B_{1max}.

3.2.3 Absolute 3D B_1 map generation employing a small reference sample

Knowledge of the absolute B_1 strength in a particular position (x,y,z) in the 3D RF probe volume, permits determination of an absolute B_1 in gauss everywhere else by employing Eq. (3.7).

The local B_1 is most readily determined with a small test sample and a measurement of the 180° pulse length. It does not depend on the material employed to find the 180° pulse length.

3.2.4 Image correction employing relative B_1^2 maps

One can correct spatial non-uniformity in one, two and three-dimensional SPRITE images by determining relative B_1 maps. The correction of the MR image is achieved by dividing the original SPRITE image by a relative B_1^2 map, Eq. (3.7). By applying this method, the non-uniformity of the B_1 field both in excitation and reception can be compensated. The intensity of the corrected image represents the sample ^1H distribution.

$$S_{local_{corrected}} = \frac{S_{local_{measured}}}{\left(\frac{B_{1local}}{B_{1\max}}\right)^2} \qquad \textbf{(3.8)}$$

In this paper, to prove the B_1 mapping method, the measured local image intensity $S_{local_{measured}}$ and the relative B_1 map B_{1local}/B_{1max}, are generated by SPRITE imaging. $S_{local_{corrected}}$ is the local image intensity after B_1 correction.

3.3 Experimental

3.3.1 B_1 mapping in the sample space at 2.4 T and 0.2 T

MRI experiments were performed on both high and low field scanners. The high field scanner was a Tecmag (Houston, TX) Apollo console equipped with a Nalorac (Martinez, CA) 2.4 T 32 cm i.d. horizontal bore superconducting magnet (Nalorac Cryogenics, Martinez, CA). The RF probe was a homebuilt quadrature eight-rung birdcage 4 cm in diameter and 10 cm in length, driven by a 2 kW 3445 RF amplifier (American Microwave Technology, Brea, CA). A 200-mm i.d. gradient set driven by *x, y* and *z* Techron (Elkhart, IN) 8710 amplifiers, provided maximum gradient strengths of 5.9 G/cm, 5.4 G/cm and 10.6 G/cm in this work.

The low field scanner was a Maran DRX-HF (Oxford Instruments Ltd., Oxford, UK) 0.2 T permanent magnet. The RF probe was a vertical solenoid 10 cm in diameter and 20 cm in length, driven by a 1 kW 3445 RF amplifier (TOMCO Technologies, Sydney, Australia). A shielded three-axis gradient coil driven by *x, y, z* Techron (Elkhart, IN) 7782 gradient amplifiers, provided maximum gradients of 26 G/cm, 24 G/cm and 33 G/cm in this work.

The Acciss, Unisort and Unifit processing packages developed in the IDL programming environment (EXELIS, Boulder, CO) by the UNB MRI Centre were employed for image reconstruction, display and signal intensity mapping.

A uniform vial of gel doped with $CuSO_4$, 10 cm in length and 4 cm in diameter, centred in the RF coil along the long axis of the RF coil, was employed as a test phantom on the 2.4 T scanner. The bulk relaxation times were $T_2^* = 4.5$ ms and $T_1 = 15$ ms.

A set of 1D SPRITE images were acquired for 1D B_1 mapping. Double-half *k*-space (dhk) SPRITE [27] imaging sequence parameters were: $G_{max,z} = 3.7$ G/cm; FOV = 130 mm; SW = 250000 Hz; 64 k-space points were acquired each with a phase encoding time of $t_p = 150$ μs with TR = 2 ms, signal averages = 32, $P_{90} = 42$ μs with 50% RF power. The dhk SPRITE pulse length was set to eight different values (1.4 μs, 1.8 μs, 2.2 μs, 2.6 μs, 3 μs, 3.3 μs, 3.6 μs and 4 μs). The shortest and longest pulse durations are equal to 3° and 8.6° flip angles. The phase cycle for both SPRITE RF pulses and the receiver was $X\bar{X}Y\bar{Y}$. The acquisition time for each image was about 52 s.

The same phantom centred along the long axis of the RF coil was employed for 3D B_1 mapping. Conical SPRITE [27] imaging sequence parameters were: $G_{max,z} = 2.8$ G/cm; $G_{max,y} = 5.4$ G/cm; $G_{max,x} = 5.8$ G/cm; FOV = 130 mm × 68 mm × 63 mm; SW = 250000 Hz; 64 *k*-space points were acquired with a phase encoding time of 200 μs and 8 signal averages. Eight 3D images were acquired with the same RF excitation pulse durations as outlined for the 1D measurement. The acquisition time for each 3D image was approximately 16 min.

A uniform rubber phantom, made of amber polyurethane (McMaster-Carr, Atlanta, GA), 10.5 cm in length and 3.8 cm in diameter centred along the long axis of the

RF probe was employed as a test object for scanning at 0.2 T. The bulk relaxation times were T_2^* = 600 μs and T_1 = 18 ms.

A set of 1D SPRITE images were acquired for 1D B_1 mapping. SPRITE imaging parameters were: $G_{max,y}$ = 3.6 G/cm; FOV = 151 mm; SW = 125000 Hz; 64 *k*-space points were acquired with a phase encoding time of 150 μs with TR = 2 ms, signal averages = 4096, P_{90} = 63 μs with 50% RF power. The dhk SPRITE pulse lengths were (1.5 μs, 2 μs, 2.5 μs, 3 μs, 3.5 μs, 4 μs, 4.5 μs and 5 μs). The shortest and longest pulse durations are equal to 2.1° and 7.1° flip angles. The acquisition time for each image was about 6 min.

To show the profile correction at 0.2 T, a water saturated Berea rock core plug, 7.5 cm in length and 3.8 cm in diameter was positioned in the same location as the phantom. The bulk relaxation times were T_2^* = 800 μs and T_1 = 200 ms. A 1D SPRITE image was acquired with: $G_{max,y}$ = 3.6 G/cm; FOV = 151 mm; SW = 125000 Hz; 64 k-space points were acquired with a phase encoding time of 150 μs with TR = 2 ms, signal averages = 8192, P_{90} = 63 μs with 50% RF power. A uniform rubber phantom, made of amber polyurethane (McMaster-Carr, Atlanta, GA), 10.5 cm in length and 7.6 cm in diameter centred along the long axis of the RF probe was employed for 3D B_1 mapping at 0.2 T. The conical SPRITE imaging sequence parameters [27] were: $G_{max,z}$ = 4.5 G/cm; $G_{max,y}$ = 3.7 G/cm; $G_{max,x}$ = 2.7 G/cm FOV = 107 mm × 131 mm × 178 mm; SW = 125000 Hz; 64 *k*-space points were acquired with a phase encoding time of 150 μs and 32 signal averages. Eight 3D images were acquired with the same RF excitation pulse durations as outlined for 1D measurement. The acquisition time for each 3D image was 1 h and 7 min.

3.4 Results

3.4.1 1D B_1 mapping at 2.4 T

Fig. 3-1a shows a 1D axial profile for a vial of uniform doped gel 10 cm in length and 3.8 cm in diameter scanned at 2.4 T. The profile is very non-uniform for a nominally uniform phantom. Note the signal magnitude at the profile edges is enhanced by approximately 23%.

Fig. 3-1b shows the plots of signal versus pulse duration for three different positions along the long axis of the RF probe (Z = 28.5 mm, 61.5 mm, and 100.5 mm). Eight pulse lengths were employed giving flip angles from 3° to 8.5°. The slopes produce $\kappa \rho_0 \exp(-t_p/T_2^*) \gamma B_1^2$ for each pixel according to Eq. (3.5). The uncertainty for each data point is estimated from the mean background noise in a profile. The noise is assumed to be constant for all the images obtained with the same number of scans. The uncertainty for each individual point in Fig. 3-1b is ±0.5% of the maximum signal of the longest pulse duration profile, 4 μs. The uncertainty ranges in Fig. 3-1b are smaller than the data symbol and are not shown.

The pixels that are close to the edge of the profile have greater slopes, in comparison to central pixels, due to a higher local B_1 field. Although the intercept in Eq. 5 is zero, in the experimental plots in Fig. 3-1b one can see the presence of small non-zero intercepts as a result of the effects of the rise and fall time on the shape of the RF pulse. The origin of the non-zero intercept is discussed in more detail in section 3.5.8.

Fig. 3-1c shows a 1D relative B_1 map for the uniform gel phantom at 2.4 T. The relative B_1 value for each pixel was found employing Eq. (3.7). With eight 1D profiles of

the uniform phantom, and 32 signal averages for each profile, the uncertainty in the relative B_1 map is ±0.7%.

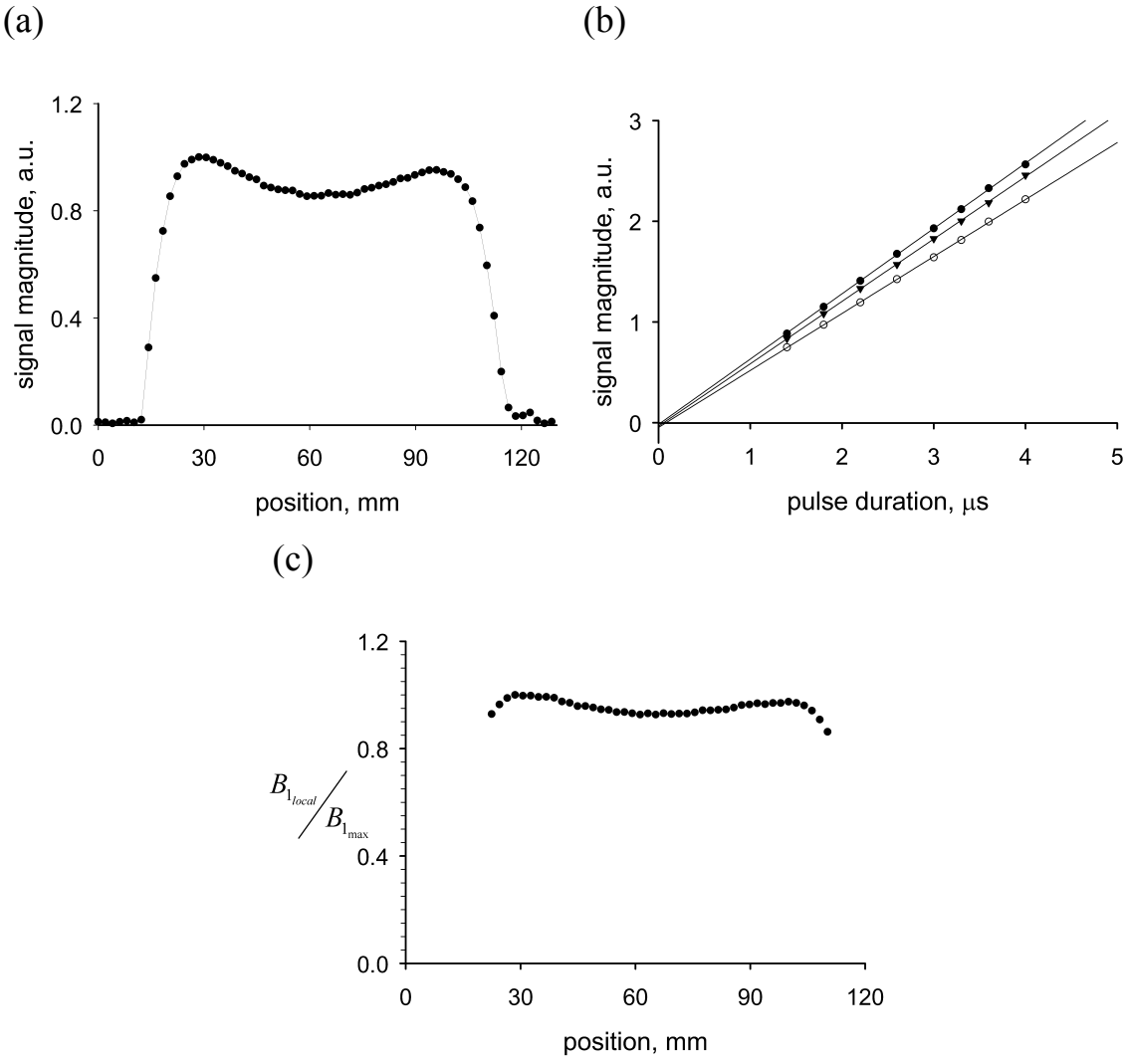

Figure 3-1 (a) A 1D axial profile for a vial of uniform doped gel scanned at 2.4 T with a birdcage probe (b) Linear plots of the signal magnitude versus the pulse duration for eight RF pulse durations at three different positions along the long axis (Z) of the RF probe (●) 28.5 mm, (○) 61.5 mm, (▼) 100.5 mm. The uncertainties are smaller than the data symbol and are not displayed. (c) Relative 1D B_1 map of the RF probe determined according to Eq. (3.7).

3.4.2 1D B_1 mapping and B_1 inhomogeneity correction at 0.2 T

Fig. 3-2a shows a 1D axial profile of an amber polyurethane phantom, 10.5 cm in length and 3.8 cm in diameter. The profile was produced employing dhk SPRITE at 0.2 T. In contrast to Fig. 3-1a the profile shows a 35% signal decrement near the edge of the profile.

Fig. 3-2b shows plots of signal variation versus pulse duration for three different positions along the long axis of the probe (Y = 40.7 mm, 95.9 mm and 119.6 mm) according to Eq. (3.5). Eight RF pulse durations were employed giving flip angles from 2.1º to 7.1º. The uncertainty for each point in Fig. 3-2b is ±0.3% of the maximum signal of the largest pulse duration profile, 5 μs. Once more, non-zero intercepts are observed in Fig. 3-2b.

Fig. 3-2c shows a relative 1D B_1 map for the above phantom centred in the long axis of a solenoid. Data processing was undertaken as for the 2.4 T measurements above. With eight 1D profiles of the amber polyurethane phantom, and 4096 signal averages for each profile the uncertainty in the relative B_1 map is ±0.5%.

Fig. 3-2d and 3-2e show 1D images of the water saturated Berea rock core plug before and after B_1 correction. The corrected 1D image was produced by employing the relative B_1 map of Fig. 3-2c. The test phantom had the same diameter as the Berea sample to ensure similar transverse B_1 averaging. The test phantom was longer than the Berea core plug to ensure proper B_1 correction.

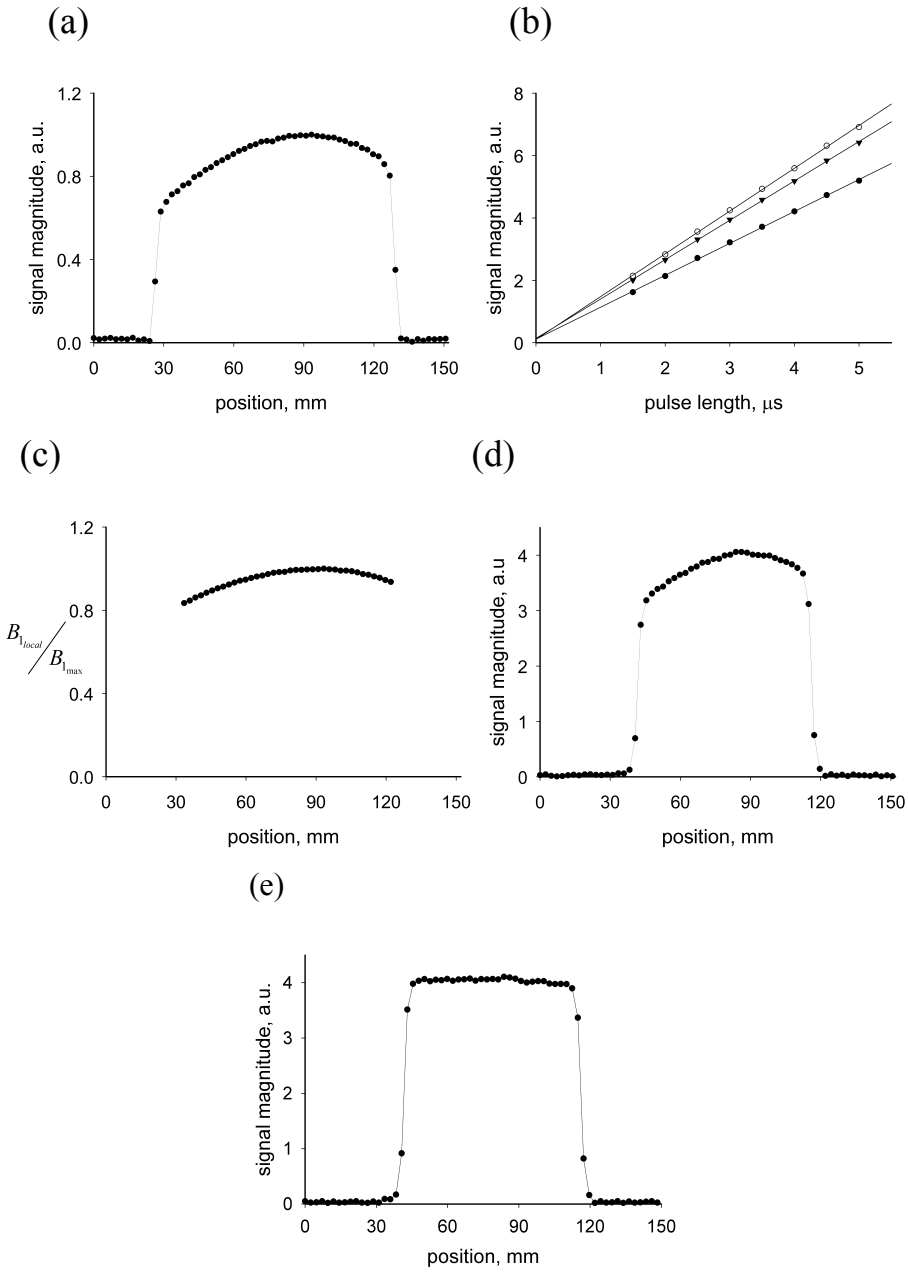

Figure 3-2 (a) A 1D axial profile of the polymer test phantom scanned at 0.2 T with a solenoid RF probe. (b) Linear plots of the signal magnitude versus the pulse duration for eight RF pulse durations at three different positions along the long axis (Y) of the RF probe (●) 40.7 mm, (○) 95.9 mm and (▼) 119.6 mm. The uncertainties are smaller than the data symbol and are not displayed. (c) The relative B_1 map of the RF probe determined according to Eq. (3.7). (d) 1D axial profile of a water saturated Berea core plug before and (e) after correction by employing the relative B_1 map of (c). The test phantom employed was longer than the Berea core plug but has the same diameter.

3.4.3 3D B_1 mapping at 2.4 T

Fig. 3-3 shows XY and XZ, 2D B_1 planes extracted from the 3D B_1 map for the 8-rung birdcage coil employed at 2.4 T. For each orientation three different planes, one in the centre and two close to the edges, are shown. The maximum B_1 value is 1.7 G while the minimum B_1 value is 0.5 G. The 180° pulse length was measured as 42 μs with 50% power for a very small test sample placed in the centre of the RF probe. Eq. (3.8) was employed to determine the absolute B_1 in gauss everywhere else inside the RF probe. The XY 2D planes show a signal increase in proximity to the birdcage coil struts. Signal enhancement occurs because of the strong B_1 field near the edges of the RF probe [36-46]. The B_1 distribution in the central part of the sample space is noticeably more uniform than near the edge of the sample space.

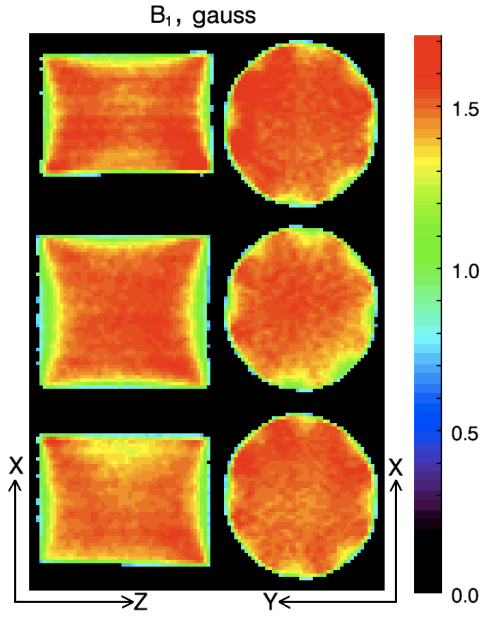

Figure 3-3 2D images of the B_1 field distribution (XZ plane, left column, and XY plane, right column) from 3D B_1 maps for the eight-rung birdcage coil at 2.4 T. For each orientation three different planes, one in the centre and two close to the edges, are shown.

3.4.4 3D B_1 mapping at 0.2 T

Figure 3-4 shows XY and XZ, 2D B_1 planes extracted from the 3D B_1 map for the solenoid employed at 0.2 T. For each orientation three different planes, one in the centre and two close to the edges, are shown. The maximum B_1 value is 0.37 G while the minimum B_1 value is 0.1 G. The 180° pulse length was measured as 68.8 μs with 50% RF power for a very small test sample placed in the centre of the RF probe. Eq. (3.7) was employed to determine the absolute B_1 in gauss everywhere else inside the RF probe. XY 2D planes show signal decrease near the edge of the probe. Signal intensity reduction occurs because of the low B_1 field strength near the ends of the solenoid [35, 44].

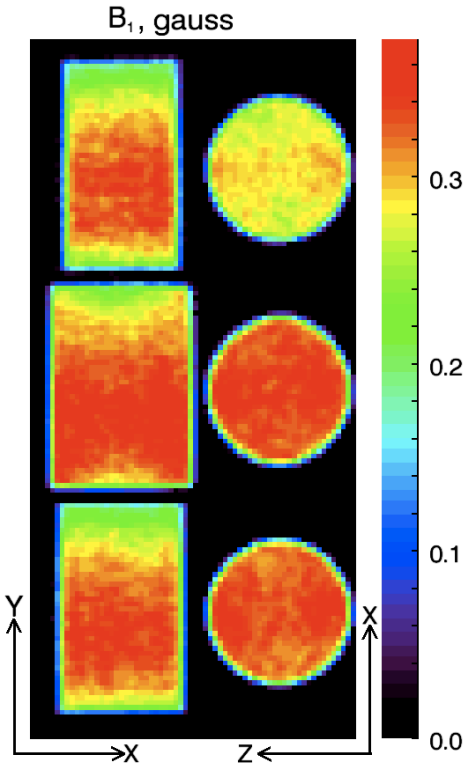

Figure 3-4 2D images of the B_1 field distribution (XZ plane, left column, and XY plane, right column) from 3D B_1 maps for solenoid at 0.2 T. For each orientation three different planes, one in the centre and two close to the edges, are shown.

3.5 Discussion

3.5.1 1D and 3D B_1 mapping at 2.4 T

The non-uniformity in the 1D axial profile for the uniform gel sample in Fig. 3-1a arises from the 3D spatial distribution of B_1 reported in Fig. 3-3. Longitudinally, B_1 is strongest near the ends of the birdcage. Transversely, it is strongest near the conductors. Our results agree well with other 3D B_1 mapping measurements and calculations for birdcage coils [37-46].

3.5.2 1D and 3D B_1 mapping and B_1 correction at 0.2 T

The 1D spatial distribution of B_1 at 0.2 T, Fig. 3-2c, is different from that at 2.4 T. The RF coil at 0.2 T was a solenoid; at 2.4 T it was a birdcage. The B_1 strength inside a solenoid varies greatly along its axis of symmetry. The B_1 mapping results in this paper agree well with other B_1 mapping measurements and calculations of the B_1 field inside a solenoid [35, 44].

B_1 field correction of density profiles, as reported in section 3.4.2 and Fig. 3-2e yield very high quality results with a uniform experimental sample yielding a uniform density profile.

The correction procedure outlined relies on a 1D B_1 measurement. It is of course eminently feasible to do 3D B_1 mapping in order to correct a 1D experimental profile. We note however that low field MRI instruments, such as the 2 MHz MARAN DRX, which are ideally suited to 1D profiling, do not have a 3D gradient set and they are restricted to 1D B_1 mapping.

3.5.3 Choice of phantom

The phantom employed for B_1 mapping and image correction must be uniform. Unless $\kappa\ \rho_0 \exp(-t_p/T_2^*)$ in Eq. (3.6) is constant over the space mapped, the ratio of slopes will not be a simple ratio of B_1^2 field strengths.

The transient longitudinal magnetization, in a SPRITE acquisition modulates the acquired signal in an exponential fashion and acts like an exponential "filter" in conventional NMR [47]. This convolution may blur the profile edges in a way that depends on the flip angle. This makes the profile edges less reliable and they are not considered in this B_1 mapping method. As a result, it is necessary that the phantom for B_1 mapping be longer than any real sample to be imaged, so that the edges of the sample may be properly defined in the corrected image.

For the 1D image correction, it is equally important that the phantom and sample diameters match. Otherwise the transverse B_1 variations, for example as shown in Fig. 3-3, will lead to erroneous correction. The 1D correction inherently assumes that the spins are uniformly distributed, radially, in the sample. If they are not, then the correction will be in error.

3.5.4 SNR consideration

1D axial profiling is very common in low field MRI, typically the imaging axis coincides with the long axis. The results of Figs. 3-2a and 3-2c show that the B_1 field in this orientation will be very inhomogeneous. Hence B_1 correction is critical for the generation of quantitative 1D profiles.

One important application of 1D axial profiling is in the quantitative MRI of fluid saturated reservoir core plugs. Current methodologies correct B_1 inhomogeneity by employing a reference sample that is often a reservoir core plug at a different saturation level. The effects of B_1 inhomogeneities are removed by dividing the sample image by the reference sample image assuming the reference sample was 100% saturated. This method works only so long as there are no other differences, such as relaxation times, between the two samples, and is not an ideal approach. This process also requires two images for a ratio measurement, which degrades the SNR of the corrected profile.

The new method for B_1 correction (Eq. (3.8)) employs the relative B_1^2 map without any sensitivity to differences in relaxation times or other effects within the sample of interest. With a single high precision reference B_1 map, one can acquire a high quality corrected profile of the sample of interest. The B_1 correction procedure will introduce negligible degradation of SNR.

3.5.5 B_1 correction for conductive samples at low field

In order to apply the B_1 map, produced by employing a polymer phantom, for conductive sample profile corrections, one should consider the quality factor alteration of the RF probe in the presence of a conductive sample. The quality factor of an NMR RF probe is the ratio of its admittance ($L\omega$) to the equivalent resistance R:

$$Q = \frac{L\omega_0}{R} \qquad \textbf{(3.9)}$$

where ω_0 is the Larmor frequency, L corresponds to the self-conductance [44]. The alternating B_1 from the RF coil induces eddy currents in a conducting sample in the

sample space. These eddy currents increase the resistance *R* in Eq. (3.9) and consequently *Q* decreases [44,48-50].

If the B_1 field derived for unit current in the *xy* plane is $(B_1)_{xy}$ when the transmitter is on, the irradiating field $(B'_1)_{xy}$ is given by [5]:

$$(B_1^{'})_{xy} = (B_1)_{xy}\sqrt{PQ/L\omega_0} \qquad \textbf{(3.10)}$$

where *P* is the supplied power which is dissipated entirely in the equivalent resistance of the coil and electrically conducting sample [44]. Thus the B_1 field strength varies with the square root of the *Q* factor.

At low field the sample conductivity has negligible effect on the probe *Q* factor and the dependence of B_1 on *Q* is through a square root. For small variations of *Q*, the B_1 field, measured by employing the polymer sample, may still be applied for B_1 correction with a brine saturated rock core plug.

3.5.6 Optimal range of pulse lengths

In order to generate a relative or absolute B_1 map from a plot of signal intensity versus t_{pulse} , Eq. (3.5), an appropriate range of t_{pulse} must be chosen.

The minimum possible t_{pulse} is a function of the hardware, specifically the RF pulse rise and fall times, as well as the exact shape of the RF pulse. The minimum pulse length also needs to generate an image with an acceptable SNR. In the work presented here, the minimum t_{pulse} employed was 1.4 μs, equal to a flip angle of 2.4°.

In considering the maximum flip angle, one should recall that Eq. (3.5) is based on a small angle approximation. The error associated with this approximation increases from 0.05% for a 3° flip angle to 0.6% for an 11° flip angle. In this work, the maximum flip angle of 8° has an associated error of 0.3%. The bandwidth of all pulses employed in the measurement must be sufficient to fully excite the full range of spins across the sample.

After determination of the pulse length range, the remaining question is how to distribute the data points, t_{pulse} in Eq. (3.5) along the *x* axis between a minimum and maximum. As discussed by Draper and Smith [51], if one knows the relation of interest is linear, one should choose minimum and maximum *x* axis points and take half of the experimental measurements at each point. This gives the minimum standard error in the slope to be determined [51].

We have found in practice that data points distributed between the maximum and minimum pulse length is preferred since it provides a simple check on the integrity of the measurement. We have settled on the employment of 6-8 different pulse lengths and a minimum signal to noise ratio of 10, for the shortest pulse duration image. A least squares fitting approach was employed to extract B_1^2. Noise was assumed to be constant for each data point.

In principle it would be possible to increment pulse power changing the flip angle while fixing the pulse length. However, it is difficult in practice to reliably change the pulse power, particularly in the limit of low flip angles [52]. Incrementing the pulse width for fixed power is however very reliable.

3.5.7 B_1 mapping in the vicinity and outside of birdcage and surface coil RF probes

As a pure phase encode method, the new B_1 mapping method will work well in the presence of conductive structures, which both support eddy currents and distort the local B_0 field through susceptibility mismatch.

The B_1 mapping technique may be employed to determine B_1 outside of the ordinary sample space. In such measurements we may employ either the background signal of the probe [36], Fig. 3-5 or we may employ temporary polymer blocks to provide background signal. Thin structures are less reliable since the images will be blurred, so mapping the image intensity variation in each pixel may not be reliable.

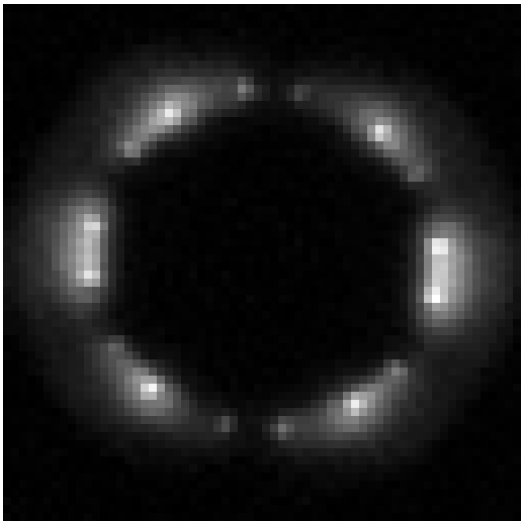

Figure 3-5 A 2D image of an RF probe with significant background signal The background MR signal arises from the polymer material employed in building the probe.

One way to alleviate the blurring problem in B_1 mapping is to reduce the flip angle range in SPRITE but this yields a reduced image SNR. An alternative solution is to

employ a longer TR to carry out full magnetization recovery after excitation. A long TR cannot be employed with SPRITE techniques, because of duty cycle restrictions. An SPI measurement [53,54] with a long TR has the advantage of avoiding T_1 blurring effects and will make relative B_1 mapping possible for thin structures. 3D SPI imaging however requires tens of hours for phantoms with a T_1 of hundreds of ms.

The other possibility to solve the T_1 blurring problem and maintain the time efficiency of the SPRITE measurement is to add, "dummy scans" at the beginning of the acquisition to allow the magnetization to stabilize in the steady state. Neither approach has been implemented in the current work to map B_1 through the probe background signal.

3.5.8 RF pulse rise/fall time measurement

The intercepts in Figs. 3-1b and 3-2b are consistently non-zero with opposite polarity for the two instruments employed. The RF pulse rise and fall time variations alter the effective time of the RF pulse and, as a result, the effective flip angle [52].

To quantify the effect of the pulse length on the RF pulse shapes, the minimum acceptable pulse length and effective time of the pulse, a pickup coil and an oscilloscope were employed to register the waveform of the RF pulses directly from the solenoid at 0.2 T and the birdcage at 2.4 T. Plots of the pulse area versus nominal pulse length showed the minimum acceptable pulse duration was 1 μs for both RF probes. For pulse durations less than this minimum the RF pulse is affected by non-stabilized rise and fall times. The 2.4 T birdcage RF probe had rise and fall times of 1.30 μs and 1.05 μs. The

0.2 T solenoid RF probe had rise and fall times of 1.25 μs and 1.40 μs. Rise and fall times were based on 10-90% amplitudes.

Effective pulse lengths were compared with the nominal pulse length by Eq. (3.11):

$$T_{eff} = \frac{\int f(t)\,dt}{< RF_{\max} >} \qquad \textbf{(3.11)}$$

where $\int$ f(t) dt is the area under the RF waveform magnitude and $<RF_{max}>$ is the average value for the highest amplitudes in the RF pulse envelope. Fig. 3-6 shows a non-ideal 8.5 MHz, 4 μs pulse duration, measured with a pickup coil positioned inside the solenoidal RF probe.

The different effective pulse lengths explain the negative and positive intercepts in Figs. 3-1b and 3-2b. For the birdcage probe T_{eff} was less than the nominal pulse duration for each pulse length so the images produced have less signal intensity than anticipated. T_{eff} less than the nominal pulse length caused the plots in Fig. 3-1b to be shifted in the negative direction along the signal magnitude axis. This yields negative intercepts.

Effective pulse lengths, which are longer than the nominal pulse length, yield intercepts, which are positive in plots such as those of Fig. 3-2b.

The intercept values calculated with Eq. (3.11) agree with the intercept values in Figs. 3-1b and 3-2b.

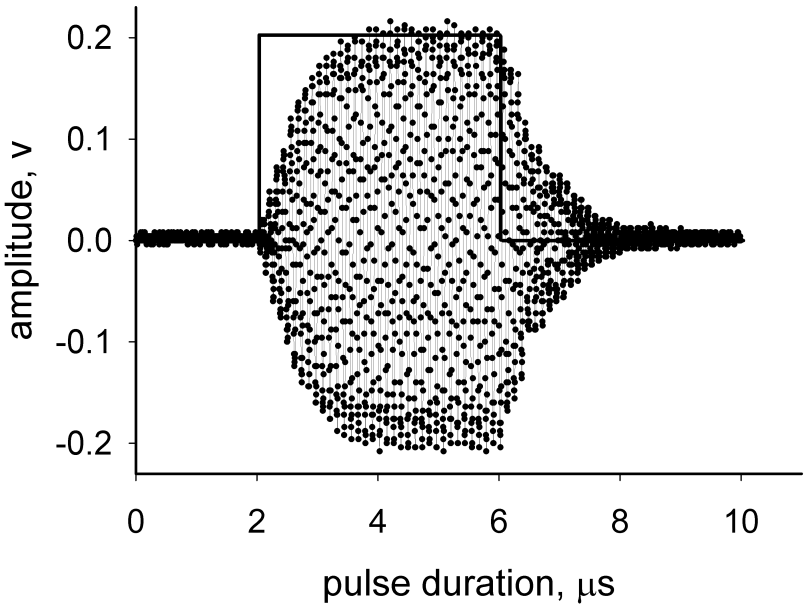

Figure 3-6 A 4 μs RF pulse waveform measured by a pickup coil and a 100 MHz bandwidth oscilloscope for the solenoid at 0.2 T compared to an ideal 4 μs RF pulse. Employing Eq. (3.11), the area under the RF pulse envelope was compared to an ideal rectangular RF pulse with the same amplitude and pulse length equal to T_{eff}. T_{eff} was calculated to be 4.110 μs ± 0.005 and 3.920 μs ± 0.001 for the solenoid and the birdcage, respectively.

3.6 Conclusion

A new technique for producing B_1 maps and correcting image non-uniformities due to B_1 variation was demonstrated. The B_1 mapping method is based on measurements of image intensities acquired with a series of low flip angle excitation pulses employing centric scan SPRITE. Unlike B_1 mapping techniques that are based on frequency encode images, B_1 mapping based on SPRITE as a pure phase encode approach is largely immune to eddy current and B_0 inhomogeneity effects and free from image distortions caused by susceptibility variations, chemical shift and paramagnetic impurities. The local

image intensity is proportional to B_1^2, ensuring high sensitivity to local B_1 variation in the sample space.

The relative B_1^2 maps produced by the new method were employed to correct non-uniformities due to excitation and reception in SPRITE images. The intensity of the corrected image better represents the sample distribution. The B_1 mapping technique is multi-dimensional and readily translated to both high field and low field systems.

3.7 References

[1] O.V. Petrov, B.J. Balcom, Two-dimensional T_2 distribution mapping in porous solids with phase encode MRI, J. Magn. Reson. 212 (2011) 102-108.

[2] O.V. Petrov, G. Ersland, B.J. Balcom, T_2 distribution mapping profiles with phase encode MRI, J. Magn. Reson. 209 (2011) 39-46.

[3] L. Li, Q. Chen, A.E. Marble, L. Romero-Zeron, B. Newling, B.J. Balcom, Flow imaging of fluids in porous media by magnetization prepared centric-scan SPRITE, J. Magn. Reson. 197 (2009) 1-8.

[4] Q. Chen and B.J. Balcom, Measurement of rock core capillary pressure curves using a single-speed centrifuge and one-dimensional magnetic resonance imaging, J. Chem. Phys. 122 (2005) 1-8.

[5] D.I. Hoult, R.E. Richards, The signal-to-noise ratio of the nuclear magnetic resonance experiment, J. Magn. Reson. 24 (1976) 71-85.

[6] D.I. Hoult, The principle of reciprocity in signal strength calculations-a mathematical guide, Concepts Magn. Reson. 12(4) (2000) 173-187.

[7] D.I. Hoult, The NMR receiver: A description and analysis of design, Prog. NMR. Spec. 12 (1978) 41-77.

[8] H. Mihara, N. Iriguchi, S. Ueno, A method of RF inhomogeneity correction in MR imaging, Magn. Reson. Mater. Phys. Biol. Med. 7 (1998) 115-120.

[9] S. Volz, U. Nöth, A. Rotarska-Jagiela, R. Deichmann, A fast B_1- mapping method for the correction and normalization of magnetization transfer ratio maps at 3T, NeuroImage, 49 (2010) 3015-3026.

[10] C.D. Sinclair, J.M. Morrow, M.G. Hanna, M.M. Reilly, T.A. Yousry, X. Golay, J.S. Thornton, Correcting radiofrequency inhomogeneity effects in skeletal muscle magnetization transfer maps, NMR. Biomed. 25(2) (2012) 262-270.

[11] J. Wang, M. Qiu, Q.X. Yang, M.B. Smith, R.T. Constable, Measurement and correction of transmitter and receiver induced non-uniformities *in vivo,* Magn. Reson. Med. 53 (2005) 408-417.

[12] E.R. McVeigh, M.J. Bronskill, R.M. Henkelman, Phase and sensitivity of receiver coils in magnetic resonance imaging, Med. Phys. 13 (1986) 806-814.

[13] F.O. Zelaya, W.U. Roffmann, S. Crozier, S. Teed, D. Gross, D.M. Doddrell, Direct visualization of B_1 inhomogeneity by flip angle dependency, Magn. Reson. Imaging. 15 (1997) 497-504.

[14] E.K. Insko, I. Bolinger, Mapping of the radiofrequency field, J. Magn. Reson. 103 (1993) 82-85.

[15] R. Treier, A. Steingoetter, M. Fried, W. Schwizer, P. Boesiger, Optimized and combined T_1 and B_1 mapping technique for fast and accurate T_1 quantification in contrast-enhanced abdominal MRI, Magn. Reson. Med. 57 (2007) 568-576.

[16] R. Stollberger, P. Wach, Imaging of the active B_1 field *in vivo*, Magn. Reson. Med. 35 (1996) 246-251.

[17] C.H. Cunningham, J.M. Pauly, K.S. Nayak, Saturated double-angle method for rapid B_1 mapping, Magn. Reson. Med. 55 (2006) 1326-1333.

[18] S. Akoka, F. Franconi, F. Seguin, A. Lepape, Radiofrequency map of an NMR coil by imaging, Magn. Reson. Imaging. 11 (1993) 437-441.

[19] A. Haase, Snapshot FLASH MRI-applications to T_1, T_2, and chemical-shift imaging, Magn. Reson. Med. 13 (1990) 77-89.

[20] V.L. Yarnkh, Actual flip angle imaging in the pulsed steady state: a method for rapid three-dimensional mapping of the transmitted radiofrequency field, Magn. Reson. Med. 57 (2007) 192-200.

[21] K. Nehrke, On the steady-state properties of actual flip angle imaging (AFI). Magn. Reson. Med. 61 (2009) 84-92.

[22] G.R. Morrell, A phase sensitive method of flip angle mapping, Magn. Reson. Med. 60 (2008) 889-894.

[23] N.G. Dowell, P.S. Tofts, Fast, accurate and precise mapping of the RF field in vivo using the 180 degree signal null, Magn. Reson. Med. 58 (2007) 622-630.

[24] L.I. Sacolick, F. Wiesinger, I. Hancu, M.W. Vogel, B_1 mapping by Bloch-Siegert shift, Magn. Reson. Med. 63 (2010) 1315-1322.

[25] F. Bloch, A. Siegert, Magnetic resonance for non-rotating fields, Phys. Rev. 57 (1940) 522-527.

[26] K. Nagashima, B_1 mapping of liquid NMR transversal RF coils: Analysis of heterogeneity and nonlinearity, Concepts. Magn. Reson. Part B (Magnetic Resonance Engineering). 41 (2012) 1-12.

[27] M. Halse, D.J. Goodyear, B. MacMillan, P. Szomolanyi, D. Matheson, B.J. Balcom, Centric scan SPRITE magnetic resonance imaging, J. Magn. Reson. 165 (2003) 219-229.

[28] M. Halse, J. Rioux, S. Romanzetti, J. Kaffanke, B. MacMillan, I. Mastikhin, N.J. Shah, E. Aubanel, B.J. Balcom, Centric scan SPRITE magnetic resonance imaging:

optimization of SNR, resolution and relaxation time mapping, J. Magn. Reson. 169 (2004) 102-117.

[29] Q. Chen, M. Halse, B.J. Balcom, Centric scan SPRITE for spin density imaging of short relaxation time porous materials, Magn. Reson. Imaging. 23 (2005) 263-266.

[30] C.R. Meyer, P.H. Bland, J. Pipe, Retrospective correction of intensity inhomogeneities in MRI. IEEE Trans. Med. Imaging. 14 (1995) 36-41.

[31] Z. Hou, A review on MR image intensity inhomogeneity correction, Int. J. Biomed. Imaging. 2006 (2006) Article ID 515, 1-11.

[32] P. Irarrazabal, C.H. Meyer, D.G. Nishimura, A. Macovski, Inhomogeneity correction using an estimated linear fit map, Magn. Reson. Med. 35 (1996) 278-282.

[33] M.S. Cohen, R.M. Dubois, M.M. Zeineh, Rapid and effective correction of RF inhomogeneity for high field magnetic resonance imaging, Human. Brain. Mapp. 10 (2000) 204-221.

[34] J.D. Gispert, S. Reig, J. Pascau, J.J. Vaquero, P. Garcia-Barreno, M. Desco, Method for bias field correction of brain T_1 weighted magnetic resonance images minimizing segmentation error, Human. Brain. Mapp. 22 (2004), 133-144.

[35] K.R. Minard, R.A. Wind, Solenoidal micro coil design. Part 1. Optimizing rf homogeneity and coil dimensions, Concepts. Magn. Reson. 13 (2001) 128-142.

[36] H. Hui, M. Oullette, B. MacMillan, F. Goora, R. MacGregor, D. Green, B.J. Balcom, High pressure vessel magnetic resonance imaging with metallic vessels, J. Magn. Reson. 213 (2011) 90-97.

[37] J.P. Hornak, J. Szumowski, R.G. Bryant, Magnetic field mapping, Magn. Reson. Med. 6 (1988) 158-163.

[38] W. Liu, C.M. Collins, P.J. Delp, M.B. Smith, Effects of end-ring/Shield configuration on homogeneity and signal-to-noise ratio in a birdcage-type coil loaded with human head, Magn. Reson. Med. 51 (2004) 217-221.

[39] M. Alecci, C.M. Collins, M.B. Smith, P. Jezzard, Radio frequency magnetic field mapping of a 3T birdcage coil: Experimental and theoretical dependence on sample properties, Magn. Reson. Med.46 (2001) 379-385.

[40] C.E. Hayes, W.A. Edelstein, J.F. Schenck, O.M. Mueller and M. Eash, An efficient highly homogeneous radiofrequency coil for whole-body NMR imaging at 1.5 T. J. Magn. Reson. 63 (1985) 622–628.

[41] M.C. Leifer, Theory of the quadrature elliptic birdcage coils. Magn. Reson. Med. 38 (1997) 732–767.

[42] C.E. Hayes, Birdcage and other high homogeneity RF coils for MR, Encyclopedia of NMR, Wiley, 1996, New York.

[43] F.D. Doty, G. Entzminger Jr, C. D. Hauck, J. P. Staab, Practical aspects of birdcage coils, J. Magn. Reson. 138 (1999) 144-154.

[44] J. Mispelter, M. Lupu, A. Briquet, NMR probeheads: for biophysical and biomedical experiments, theoretical principles & practical guidelines, Imperial College Press, London, 2006.

[45] C. Wang, G.X. Shen, B_1 field, and SNR comparisons for birdcage, TEM, and Microstrip coils at 7 T, J. Magn. Reson. Imaging. 24 (2006) 439-443.

[46] C.M. Collins, S. Li, Q.X. Yang, M.B. Smith, A method for accurate calculation of B_1 fields in three dimensions. Effects of shield geometry on field strength and homogeneity in the birdcage coil, J. Magn. Reson. 125 (1997) 233-241.

[47] I.V. Mastikhin, B.J. Balcom, P.J. Prado, C.B. Kennedy, SPRITE MRI with prepared magnetization and centric k-space sampling, J. Magn. Reson. 136 (1999) 159-168.

[48] D.I. Hoult, P.C. Lauterbur, The sensitivity of the zeugmatographic experiment involving human samples, J. Magn. Reson. 34 (1979) 425-433

[49] D.G. Gadian, F.N. H. Robinson, Radiofrequency losses in NMR experiments on electrically conducting samples, J. Magn. Reson. 34 (1979) 449-445

[50] B. Maravaglia, Physics of NMR spectroscopy in biology and medicine, North-Holland, Oxford, 1988.

[51] N.R. Draper, H. Smith, Applied regression analysis, 3rd edition, Wiley series in probability and statistics, 1998, New York.

[52] F. Balezeau, P.A. Eliat, A.B. Cayamo, H. Saint-Jalmes, Mapping of low flip angles in magnetic resonance, Phys. Med. Bio. 56 (2011) 6635-6647.

[53] D.E. Axelson, A. Kantzas, A. Nauerth, ^{1}H magnetic resonance imaging of rigid polymeric solids, Solid State Nucl. Magn. Reson. 6 (1996) 309-321.

[54] S. Gravina, D.G. Gory, Sensitivity and resolution of constant-time imaging, J. Magn. Reson. 104 (1994) 53-61.

Chapter 4 - Mapping B_1-induced Eddy Current Effects Near Metallic Structures in MR Images: A Comparison of Simulation and Experiment

The B_1 mapping method based on pure phase encode SPRITE which was introduced in Chapter 3 is largely immune to gradient-induced eddy currents, B_0 inhomogeneity and magnetic susceptibility variations. The purpose of this Chapter is to employ the new B_1 mapping method to isolate and determine B_1-induced intensity distortion effects in the sample space adjacent to metal structures.

This chapter is largely based on the paper "B_1 mapping with a pure phase encode approach: quantitative density profiling" published in the Journal of Magnetic Resonance, 250 (2015) 17-24. However, a significantly greater level of detail and mathematical rigor is provided herewith. The format of references in this chapter follows that of the original article.

Abstract

Magnetic resonance imaging (MRI) in the presence of metallic structures is very common in medical and non-medical fields. Metallic structures cause MRI image distortions by three mechanisms: (1) static field distortion through magnetic susceptibility mismatch, (2) eddy currents induced by switched magnetic field gradients and (3) radio frequency (RF) induced eddy currents. Single point ramped imaging with T_1 enhancement (SPRITE) MRI measurements are largely immune to susceptibility and gradient induced eddy current artifacts. As a result, one can isolate the effects of metal objects on the RF field. The RF field affects both the excitation and detection of the

magnetic resonance (MR) signal. This is challenging with conventional MRI methods, which cannot readily separate the three effects.

RF induced MRI artifacts were investigated experimentally at 2.4 Tesla by analyzing image distortions surrounding two geometrically identical metallic strips of aluminum and lead. The strips were immersed in agar gel doped with contrast agent and imaged employing the conical SPRITE sequence. B_1 mapping with pure phase encode SPRITE was employed to measure the B_1 field around the strips of metal. The strip geometry was chosen to mimic metal electrodes employed in electrochemistry studies.

Simulations are employed to investigate the RF field induced eddy currents in the two metallic strips. The RF simulation results are in good agreement with experimental results. Experimental and simulation results show that the metal has a pronounced effect on the B_1 distribution and B_1 amplitude in the surrounding space. The difference in electrical conductivity between the metals has a minimal effect.

4.1 Introduction

Magnetic resonance imaging (MRI) is an essential measurement and diagnostic tool in medical and non-medical fields. Metal implants like screws, hip prostheses and clips are very common clinically. The presence of metallic structures in the sample space causes image distortions. Recently, the challenges of imaging near metal surfaces in electrochemical MRI studies have been investigated. MRI has enormous potential for the development of energy devices such as batteries and fuel cells, and can also be extended to investigate other electrochemical processes [1-3]. In materials science, MRI has been developed for spatially resolved analysis of fluids in porous media [4-7], MR

measurements employing metal vessels enclosing both probe and sample at high pressure and variable temperature provide unique information about the microscopic behavior of liquids [8]. Metal vessels may lead to severe image distortions, but these distortions can be mitigated by careful choice of MRI method.

Metals produce local artifacts that distort MR images in regions close to the metal. Artifacts due to metallic objects may be caused by (1) static field magnetic susceptibility mismatch, (2) eddy currents induced by switched magnetic field gradients or (3) radio frequency (RF) field eddy currents [9-18].

Susceptibility artifacts arise from local static field (B_0) inhomogeneities caused by discontinuities in magnetic susceptibility at the boundaries of the metallic material and are characterized by geometric distortions in the readout direction of the image, perturbation in the selected slice and signal intensity variations. The severity of the artifact depends on the metallic object geometry, orientation with respect to the static field, the magnetic susceptibility difference, and the strength of the B_0 field [18-23]. Methods for B_0 inhomogeneity correction have been suggested in the literature [24-27]. Metallic objects generally have reduced susceptibility artifacts when their long axis is parallel to B_0 [18].

Switched magnetic field gradients and RF pulses can induce eddy currents in a metallic object, which may result in image distortion and image artifacts [20, 28-33]. In each case the varying field alters the magnetic flux through the conductive object and induces eddy currents due to Faraday's law. Lenz's law states that the eddy current flows so as to oppose the flux change inside the current path. RF eddy currents induced in the metallic object can result in B_1 enhancement or cancellation near the surface of the object

[12, 17]. B_1 homogeneity in the sample space can be significantly altered. Due to the principle of reciprocity, any variation in the B_1 field has an effect both on signal excitation and signal detection. The time varying B_1 field caused by eddy currents is superimposed upon the originally applied B_1 field [16].

The severity of metal-related image distortions is determined by the pulse sequence and sequence parameters. Gradient recalled echo (GRE) methods are very sensitive to the presence of metal [34]. Intravoxel dephasing is the dominant cause of signal loss in GRE imaging, resulting in signal loss around the metal in the processed images. Decreasing the echo time and decreasing the voxel size will reduce the degree of intravoxel dephasing due to B_0 inhomogeneity [34]. Spin echo sequences apply refocusing RF pulses that correct for static/fixed magnetic field inhomogeneity [34]. Misregistration artifacts occur in the frequency encoding direction but not in the phase encoding direction [20, 35-37]. A technique called view angle tilting (VAT) has been shown to reduce metal related artifacts. VAT suffers from image blurring across the image field of view (FOV) and low image signal to noise ratio (SNR) [38-40]. Single point imaging methods [35-37] with longer times for gradient stabilization can solve these problems to a significant extent. SPRITE imaging, one type of single point imaging method, may be employed to isolate B_1 related distortions since B_0 inhomogeneity, chemical shift, magnetic susceptibility, and magnetic field gradient induced eddy current artifacts are largely eliminated.

Ilott et al. [9] have recently undertaken an experimental and simulation study of the electrical effects associated with lithium MRI studies of metallic lithium. Their study

concentrated on the B_1 induced eddy current distribution in the lithium conductor and its spatial variation due to the skin effect.

In the current work, B_1 mapping has been undertaken to measure distortions in the B_1 field in the sample space surrounding metal conductors. We also analytically measure the local B_1 field in the sample space with a recently introduced B_1 mapping method [41]. The SPRITE MRI signal in each pixel (or voxel) is proportional to B_1^2 due to B_1 sensitivity in both excitation and reception. Therefore, the method is very sensitive to B_1 variation in the sample space [41].

Simulations of B_1 field induced eddy currents are also presented. The B_1 induced eddy currents result in distortion of the B_1 field in the sample space. The B_1 simulation results are in good agreement with experimental results and show the significant effects of metal on the B_1 field distribution and B_1 amplitude in surrounding space. B_1 field distortion around good conductors is largely independent of the conductivity value. Thus, the difference in electrical conductivity of the metals has a minimal effect.

4.2 Theory

4.2.1 Theoretical consideration of B_1-induced artifacts

Eddy currents are induced in metallic structures by the time-varying magnetic field components of B_1. Faraday's law of induction explains this phenomenon. For a static conductor exposed to time varying magnetic flux:

$$EMF = -\frac{\partial \Phi}{\partial t} = -\frac{\partial}{\partial t}\int_S \vec{B}_1 \cdot \vec{n}\, ds \qquad \textbf{(4.1)}$$

where EMF is the induced electromotive force due to changing flux Φ through a conductive object. $\vec{B}_1$ is the magnetic field applied for excitation and $\vec{n}$ is the normal vector perpendicular to the surface S. The induced electromotive force causes an electrical current to flow in the conductor. The induced currents produce local time-varying magnetic fields and as a result, the uniformity of $\vec{B}_1$ in the sample space will be disturbed. $\vec{B}_1$ intensity distortion may result in a higher or lower amplitude of $\vec{B}_1$ locally around a metallic object, which increases or decreases the local excitation flip angle. By the principle of reciprocity, the local RF artifacts are compounded by altered receive sensitivity of the MR coil [12].

The change in transmit and receive sensitivity due to the presence of a metallic structure, assuming linear RF polarization, can be understood by considering a simple circuit model [12]. When current I, at frequency ω_0 is applied to a RF probe, the total effective magnetic field, B_1 (transverse to B_0), produced by the RF coil in the presence of the metallic structure is given by:

$$B_1(\vec{r}) = I\left[B_{1,app}(\vec{r}) + \frac{j\omega_0 M}{Z_{metal}} B_{1,ind}(\vec{r})\right] \qquad \textbf{(4.2)}$$

where $B_{1,app}$ is the transverse field per unit current applied by the RF coil in the absence of the metallic structure and $B_{1,ind}$ is the transverse field induced per unit current in the metallic structure. Only the transverse components will be considered because they are involved in exerting a torque on the net magnetic moment [12]. M is the mutual inductance between the RF coil and the metallic structure and Z_{metal} is the total impedance of the metallic structure. Z_{metal} is split into R_{metal} (resistance) and $j\omega_0 L_{metal}$

(reactance), ignoring the small capacitance. In calculating the transmit sensitivity, one should be concerned solely by the magnitude of B_1. Any phase variation will be exactly cancelled in receive mode, provided the same RF coil is employed for transmission and reception [12, 17].

The fractional changes in transmit and receive sensitivity of the RF coil, θ_{TS} and θ_{RS} [12], because of the presence of a metallic structure, are:

$$\theta = \theta_{TS}(\vec{r}) = \theta_{RS}(\vec{r}) = \frac{\left| B_{1,app}(\vec{r}) + \frac{j\omega_0 M}{Z_{metal}} B_{1,ind}(\vec{r}) \right|}{\left| B_{1,app}(\vec{r}) \right|} \qquad \textbf{(4.3)}$$

in which, $Z_{metal} = R_{metal} + j\omega_0 L_{metal}$. The term $j\omega_0 M/Z_{metal}$ is dependent upon the electrical parameters of the metallic structure and M would normally include a geometrical factor. At high frequency, $\omega_0 L_{metal}$ is much greater than R_{metal} [17], which contributes only 0.5% to the overall impedance, so the resistive term can be ignored. Dominant terms therefore only depend on metal geometry and are independent of the metal's conductivity σ_{metal}, which has an effect only through $R_{metal} \propto 1/\sigma_{metal}$. In this case Eq. (4.3) can be simplified as:

$$\theta = 1 + \left| \frac{j\omega_0 M}{Z_{metal}} \left(\frac{B_{1,ind}(\vec{r})}{B_{1,app}(\vec{r})} \right) \right| \qquad \textbf{(4.4)}$$

The induced field, $B_{1,ind}$ of Eq. (4.4) is geometry dependent and can be calculated by applying the Biot-Savart law [12] (assuming quasi-static conditions).

4.2.2 Electromagnetic field analysis

The electromagnetic field may be expressed employing the differential form of Maxwell's equations [42,43]. In particular:

$$\vec{\nabla} \times \vec{E} = -\frac{\partial \vec{B}}{\partial t} \qquad \textbf{(4.5)}$$

$$\vec{\nabla} \times \vec{H} = \vec{J} + \frac{\partial \vec{D}}{\partial t} \qquad \textbf{(4.6)}$$

$$\vec{\nabla} \cdot \vec{B} = 0 \qquad \textbf{(4.7)}$$

in which (for linear, isotropic, and homogeneous media):

$$\vec{D} = \varepsilon \vec{E} \qquad \textbf{(4.8)}$$

$$\vec{H} = \frac{\vec{B}}{\mu} \qquad \textbf{(4.9)}$$

where permittivity ε is the constant of proportionality between the electric flux density (electric displacement) vector $\vec{D}$ and the electric field intensity vector $\vec{E}$. The

permeability μ is the constant of proportionality between the magnetic field intensity vector $\vec{H}$ and the magnetic flux density vector $\vec{B}$. $\vec{J}$ is the density of free currents [43]. Eq. (4.5) is another statement of Faraday's law, shown earlier as Eq. (4.1).

$\vec{J}$ may be expressed as the sum of $\vec{J}_0$ (input current) and induced eddy current, $\vec{J}_{ind}$ current. Applying Ohm's law ($\vec{J}_{ind} = \sigma\vec{E}$), where σ is the electrical conductivity, for the latter current results in $\vec{J}$ being expressed as:

$$\vec{J} = \vec{J}_0 + \sigma\vec{E} \qquad \textbf{(4.10)}$$

In this work, RF radiation of the sample including a metal strip surrounded by a gel is considered and there are only induced eddy currents ($\vec{J}_0 = 0$). Substituting Eqs. (4.8) and (4.10) in Eq. (4.6):

$$\vec{\nabla} \times \vec{H} = \sigma\vec{E} + \varepsilon\frac{\partial\vec{E}}{\partial t} \qquad \textbf{(4.11)}$$

Note that the displacement current ($\frac{\partial\vec{D}}{\partial t} = \varepsilon\frac{\partial\vec{E}}{\partial t}$) is negligible inside the metal strip (i.e. $\sigma\vec{E} >> \varepsilon\frac{\partial\vec{E}}{\partial t}$) and the current density ($\vec{J} = \sigma\vec{E}$) is negligible inside the gel phantom where σ is low (i.e. $\sigma\vec{E} << \varepsilon\frac{\partial\vec{E}}{\partial t}$).

By taking the curl of Eq. (4.11) and considering that the del operator and the time derivative operators (whether taken once or twice) will commute:

$$\vec{\nabla} \times \vec{\nabla} \times \vec{H} = \sigma(\vec{\nabla} \times \vec{E}) + \varepsilon \frac{\partial(\vec{\nabla} \times \vec{E})}{\partial t} \qquad \textbf{(4.12)}$$

Applying Faraday's law, Eq. (4.5), to Eq. (4.12) given that $\vec{\nabla} \times \vec{\nabla} \times \vec{H} = \vec{\nabla}(\vec{\nabla} \cdot \vec{H}) - \vec{\nabla}^2 \vec{H}$ and $\vec{\nabla} \cdot \vec{H} = 0$:

$$\vec{\nabla}^2 \vec{H} = \sigma\mu \frac{\partial \vec{H}}{\partial t} + \varepsilon\mu \frac{\partial^2 \vec{H}}{\partial t^2} \qquad \textbf{(4.13)}$$

The term on the left hand side of Eq. (4.13) is the Laplacian of the vector field $\vec{H}$, which may be written in Cartesian coordinates as:

$$\vec{\nabla}^2 \vec{H} = \frac{\partial^2 \vec{H}}{\partial x^2} + \frac{\partial^2 \vec{H}}{\partial y^2} + \frac{\partial^2 \vec{H}}{\partial z^2} \qquad \textbf{(4.14)}$$

Sinusoidal oscillations are assumed for the temporal field variation. It is possible to define a vector field $\vec{H}(x,y,z,t)$:

$$\vec{H}(x,y,z,t) = \vec{H}_0(x,y,z,t)\, e^{j\omega t} \qquad \textbf{(4.15)}$$

Details outside this assumption are beyond the scope of this thesis. Therefore Eq. (4.13) may be written as:

$$\vec{\nabla}^2 \vec{H} = j\omega\sigma\mu\vec{H} - \omega^2\mu\varepsilon\vec{H} \qquad \textbf{(4.16)}$$

The differential equation for the case of a single component of the magnetic field H_y inside a sample including a metal strip surrounded by a gel, is determined from Eq. (4.16):

$$\begin{aligned}\vec{\nabla}^2 H_y &= j\omega\sigma\mu H_y - \omega^2\mu\varepsilon H_y \\ &= j\omega\mu(\sigma + j\omega\varepsilon)H_y\end{aligned} \qquad \textbf{(4.17)}$$

Note that this single component field is applicable to an MR measurement where a linearly polarized RF field is applied along a given direction. The vector wave equation in Eq. (4.17) may be expressed as:

$$\vec{\nabla}^2 H_y - k^2 H_y = 0 \qquad \textbf{(4.18)}$$

where k is a propagation constant [42]. Hence, we may rewrite Eq. (4.17) as:

$$\vec{\nabla}^2 H_y - j\omega\mu(\sigma + j\omega\varepsilon)H_y = 0 \qquad \textbf{(4.19)}$$

and

$$k^2 = j\omega\mu(\sigma + j\omega\varepsilon) \qquad \textbf{(4.20)}$$

The propagation constant k is the sum of attenuation and phase constants, which are typically denoted as α and β, respectively (i.e. $k = \alpha + j\beta$). Rewriting Eq. (4.20) in terms of α and β [42]:

$$\alpha = \omega\sqrt{\mu\varepsilon}\left\{\frac{1}{2}\left[\sqrt{1+\left(\frac{\sigma}{\omega\varepsilon}\right)^2}-1\right]\right\}^{1/2} \quad \textbf{(4.21)}$$

$$\beta = \omega\sqrt{\mu\varepsilon}\left\{\frac{1}{2}\left[\sqrt{1+\left(\frac{\sigma}{\omega\varepsilon}\right)^2}+1\right]\right\}^{1/2} \quad \textbf{(4.22)}$$

The attenuation constant α is expressed in Nepers per meter (Np/m) and shows the attenuation of the field as it propagates through a medium. The phase constant β in rad/m will determine the amount of phase shift. The distance the wave must travel in a lossy medium to reduce its value by a factor of e^{-1} is defined as the skin depth ($\delta = 1/\alpha$).

In this work a metal strip was surrounded by a low conductivity gel. The conductivity of the metal strip is large relative to that of the gel. Hence, $(\sigma/\omega\varepsilon)^2 >> 1$ within the metal strip and Eqs. (4.21) and (4.22) are dominated by the conduction current density term. Similarly, $(\sigma/\omega\varepsilon)^2 << 1$ for the gel and Eqs. (4.21) and (4.22) are dominated by the displacement current density term. For each of these two cases, the exact forms of α and β as shown in Eqs. (4.21) and (4.22) can be approximated by simpler forms [42] as summarized in Table 4.1.

From these simplified terms, it is apparent that the B_1 field in a high conductivity metal is highly attenuated and does not effectively penetrate the conductor while experiencing rapid phase changes. In contrast, the B_1 field in the low conductivity gel is not significantly attenuated and does effectively penetrate while experiencing moderate phase changes.

Solutions to Eq. (4.17) are not readily determined analytically. We have therefore resorted to numerical simulation in order to calculate RF magnetic field distributions in and around the sample space. In electromagnetic simulations, it is natural to employ $\vec{H}$, since permeability and susceptibility effects may be determined from $\vec{H}$. However, since $\vec{B}$ contains induced magnetization as well as the direct effect of $\vec{H}$, it is the appropriate quantity to use in MR of finite permeability materials [44].

Table 4.1 Propagation constants in a good dielectric and a good conductor

	Good dielectric $\left(\frac{\sigma}{\omega\varepsilon}\right)^2 << 1$	Good conductor $\left(\frac{\sigma}{\omega\varepsilon}\right)^2 >> 1$
Attenuation constant, α	$\frac{\sigma}{2}\sqrt{\frac{\mu}{\varepsilon}}$	$\sqrt{\frac{\omega\mu\sigma}{\varepsilon}}$
Phase constant, β	$\omega\sqrt{\mu\varepsilon}$	$\sqrt{\frac{\omega\mu\sigma}{\varepsilon}}$

4.2.3 B_1 mapping around metallic structures

The new technique for B_1 mapping, described in Chapter 3, was employed to map B_1 around the objects of interest [41].

Practical measurement of the local B_1 proceeds via Eq. (4.23) by incrementing t_{pulse}, the excitation pulse duration, in successive images while maintaining the low flip angle limit [41]. Plotting local signal versus t_{pulse} permits determination of B_1 via the slope in each pixel or voxel.

$$S_{local}(\vec{r}) = \kappa \rho_0(\vec{r}) \exp(-\frac{t_p}{T_2^*}) \gamma B_1^2(\vec{r}) t_{pulse} \qquad \textbf{(4.23)}$$

S_{local} is a unitless signal intensity in image space and κ is a constant of proportionality. ρ_0 is measured in grams of ^1H per unit volume material at any point $\vec{r}$, t_p is the phase encoding time between RF excitation and signal reception and T_2^* is the effective spin-spin relaxation time. For $t_p << T_2^*$, the exponential term may be neglected. B_1 is the component of the RF field produced in the transverse plane and γ is the gyromagnetic ratio [41].

4.3 Experimental

MRI experiments were performed on a Tecmag (Houston, TX) Apollo console equipped with a Nalorac (Martinez, CA) 2.4 T 32 cm i.d. horizontal bore superconducting magnet (Nalorac Cryogenics, Martinez, CA). The RF probe was a homebuilt quadrature eight-rung birdcage 4.5 cm in diameter and 10 cm in length, driven by a 2 kW (American Microwave Technology, Brea, CA) 3445 RF amplifier. A 200 mm i.d. gradient set driven by *x*, *y* and *z* Techron (Elkhart, IN) 8710 amplifiers, provided maximum gradient strengths of 5.9 G/cm, 5.4 G/cm and 10.6 G/cm, respectively, in this work. The RF probe was employed with a single mode of excitation and reception (linear polarization of B_1).

A conical SPRITE [36] image was acquired for a uniform cylindrical vial of gel doped with 0.2 mM $GdCl_3$ enclosing a rectangular strip of aluminum (Al), which is minimum purity 95.8% (Metal Supermarkets, Mississauga, ON, Canada). The electrical parameters of Al are summarized in Table 4.2. The Al strip was 3 cm in length, 1 cm in width, and 2.3 mm in thickness. The gel was 4 cm in length and 4.4 cm in diameter with bulk relaxation times of T_2^* = 2.5 ms (measured from a single exponential fit to the free

induction decay) and T_1 = 21 ms. Conical SPRITE imaging sequence parameters were: FOV = 10×6.5×6.5 cm^3, SW = 250000 Hz; 64 k-space points were acquired each with a phase encoding time t_p = 100 μs with TR = 2 ms, signal averages = 32, 90° pulse duration 33 μs with 60% RF power. The conical SPRITE pulse length was set to 4 μs, which corresponds to a 6.6° flip angle. The phase cycle for both the RF pulses and the receiver was $x\bar{x}y\bar{y}$. The acquisition time for each image was 1 h and 17 min.

Table 4.2 The physical properties of the metal strips employed in the experiments and in the simulations

Parameters	Al	Pb
Conductivity, σ (S/m)	3.5×10^7	4.8×10^6
Relative Permeability, μ_r	1.00002	0.99998

For the 3D B_1 mapping experiments, a uniform cylindrical vial of gel, doped with 0.2 mM $GdCl_3$, 6 cm in length and 3.5 cm in diameter enclosed a rectangular strip of Al, or lead (Pb), minimum purity 98% (McMaster-Carr, Elmhurst, IL). The electrical parameters of Pb are summarized in Table 4.2. The strips were 5.5 cm in length 8.5 mm in width and 2.3 mm in thickness. A set of 3D SPRITE images was acquired for 3D B_1 mapping [41]. Conical SPRITE [36] imaging sequence parameters were: FOV = 13×6×6 cm^3, SW = 250000 Hz, 64 k-space points were acquired each with a phase encoding time of t_p = 100 μs with TR = 2 ms, signal averages = 32, 90° pulse duration 33 μs with 60% RF power. The conical SPRITE RF pulse length was set to 3 μs, 3.5 μs, 4 μs, 4.5 μs, 5 μs, and 5.5 μs. The shortest and longest pulse durations are equal to 5° and 8° flip angles,

respectively. The phase cycle for both the RF pulses and the receiver was $x\bar{x}y\bar{y}$. The acquisition time for each image was 1 h and 17 min.

The Acciss, Unisort and Unifit processing packages, developed in the IDL (EXELIS, Boulder, CO) programming environment by the UNB MRI Centre were employed for image reconstruction, display and signal intensity mapping.

CST Microwave Studio (Framingham, MA), a finite element analysis software [45], was employed for the RF eddy current simulations. CST Microwave Studio is an electromagnetic field analysis program that can calculate eddy currents and resulting magnetic fields. As input parameters, the shape of the object, permeability, permittivity, electrical conductivity, and RF field frequency are given. As output parameters, CST provides the spatial distribution of the magnetic field intensity $\vec{H}$ along with induced current distributions $\vec{J}$ on conductive structures. In the electromagnetic simulation, the space was divided into many small mesh elements. The resulting mesh was generated such that regions-of-interest are meshed to a finer degree than those of less interest [28]. The number of mesh cells impacts the accuracy of the solution as well as the simulation run time. The simulations were completed using a PC with a 2.66 GHz Intel Core i7-M620 CPU with 8 GB of RAM installed.

4.4. Results and discussions

The dimensions and orientations of the metal strips, employed in two different experimental geometries, are illustrated in Fig. 4-1. Figs. 4-1a and 4-1b illustrate the first geometry in which the surface of the metal strip is perpendicular to the B_1 field but parallel to B_0. *x, y*, and *z* are the laboratory frame of reference which correspond to our

imaging (gradient) axes. Note that the B_1 field direction of the birdcage probe employed is not aligned with the laboratory axes. It makes a 45° angle with the *y* axis. We have chosen 45° off axis to represent the general case for a birdcage probe where the B_1 field direction is not naturally aligned with the laboratory frame of reference, unlike the case of a solenoid RF probe. The B_1 field orthogonal to the metal structure is a geometry employed in our simulations, other theoretical calculation [18], and experimental results in the literature [1].

Figs. 4-1c and 4-1d show the second experimental geometry. Fig 4-1c shows the position of the metal strip in the $GdCl_3$ doped gel. Fig 4-1d shows the B_1 and B_0 field orientations. The surface of the metal strip in this case is in the same plane as the B_1 field (*xy* plane) and perpendicular to B_0. Once again the B_1 field is oriented 45° off the *y* axis and is representative of a birdcage RF probe. The physical properties of the metal strips are reported in Table 4.2.

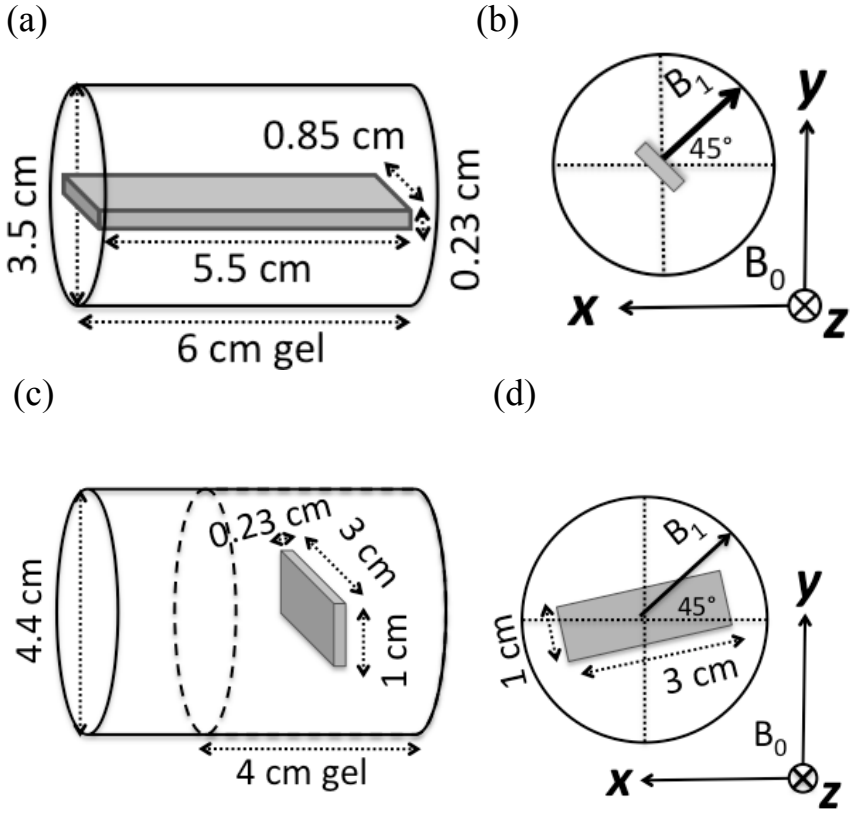

Figure 4-1 The dimensions and orientations of the metal strips employed in two different experimental geometries. (a) and (b) show the first case in which the surface of the metal strip was perpendicular to the B_1 field and parallel to B_0. *x, y,* and *z* are laboratory (imaging) axes. The RF probe is a birdcage probe where the B_1 field direction is not automatically aligned with lab axes *x* or *y*. (c) and (d) show the second case in which the surface of the metal strip is in the same plane as the B_1 field (*xy* plane) and perpendicular to B_0. (c) shows the position of the metal strip in the $GdCl_3$ doped gel in the second case, (d) shows the directions of B_1 and B_0 with respect to the metal strip. A birdcage RF probe was employed to generate B_1.

As stated in Section 4.2.2, the B_1 field penetrates the gel with little attenuation (α small) but is significantly attenuated (α large) by the metal and results in the formation of RF eddy currents. Similarly, phase changes through the gel are moderate while there are rapid changes through the metal.

We now consider experimental results with the first geometry where the surface of the metal strip is parallel to B_0 and perpendicular to B_1. Fig. 4-2a shows 2D slices of the relative B_1 field distribution (B_1/B_{1max}) (*xy* and *xz* planes) from experimental 3D B_1 maps for a uniform vial of gel doped with $GdCl_3$ enclosing a strip of Al, with orientation as shown in Fig. 4-1a and 4-1b. For each orientation, five different planes, one in the center and four displaced from the center, are shown. The B_1 field homogeneity outside the metal strip is severely distorted with a very characteristic dipole pattern of enhanced B_1 and suppressed B_1 apparent in the transverse plane maps. B_1 artifacts will be maximized when the B_1 field is perpendicular to the surface of the strip (Eq. (4.1)). The dipole pattern in the *xy* planes is in agreement with theory [18], experiments [1] and the simulation results that are reported below, confirming the excellent performance of our B_1 mapping method to measure B_1 in the presence of metallic structures.

Regions with enhanced and reduced B_1 in the *xy* planes are symmetric due to the symmetric shape of the metal strip. Near the eddy current, B_1 is stronger but the decrease in B_1 strength is inversely proportional to distance from the current source (Biot-Savart law). Midway between the long edges of the strip, the superposition of the induced fields exactly cancels the applied field giving a net B_1 field of zero.

Asymmetry in the B_1 field alteration above and below the metal strip in the *xz* plane (longitudinal slice, right side of Fig. 4-2a, is a result of the metal strip making an angle of 45° with the imaging axes (*x,y*), as shown in Fig. 4-1b. The central longitudinal slice is far from induced currents (along the long edges of the strip). No intensity distortions due to $B_{1,ind}$ (the B_1 caused by induced eddy currents) will be observed above and below for the central longitudinal slice. As the *xz* planes displayed are displaced from

the central plane, the region of the *xz* plane closest to the induced currents will experience greatest B_1 distortion ($B_{1i} = B_{1i,ind} + B_{1,app}$, $i = x', y'$), while the other side further from the induced currents, experience a reduced B_1.

Fig. 4-2b shows 2D slices of the relative B_1 field distribution (B_1/B_{1max}) (*xy* and *xz* planes) from experimental 3D B_1 maps for a uniform vial of gel doped with $GdCl_3$ enclosing a strip of Pb ($\sigma_{Pb}/\sigma_{Al} = 1.37 \times 10^{-1}$), with orientation as shown in Figs. 4-1a and 4-1b. The results are qualitatively the same as Fig. 4-2a, suggesting that that the electrical conductivity of the metal has a minimal effect on the B_1 field in the surrounding space. In agreement with expectation (section 4.2.1), these results confirm that the B_1 field distortion around conductors is largely independent of the conductivity values.

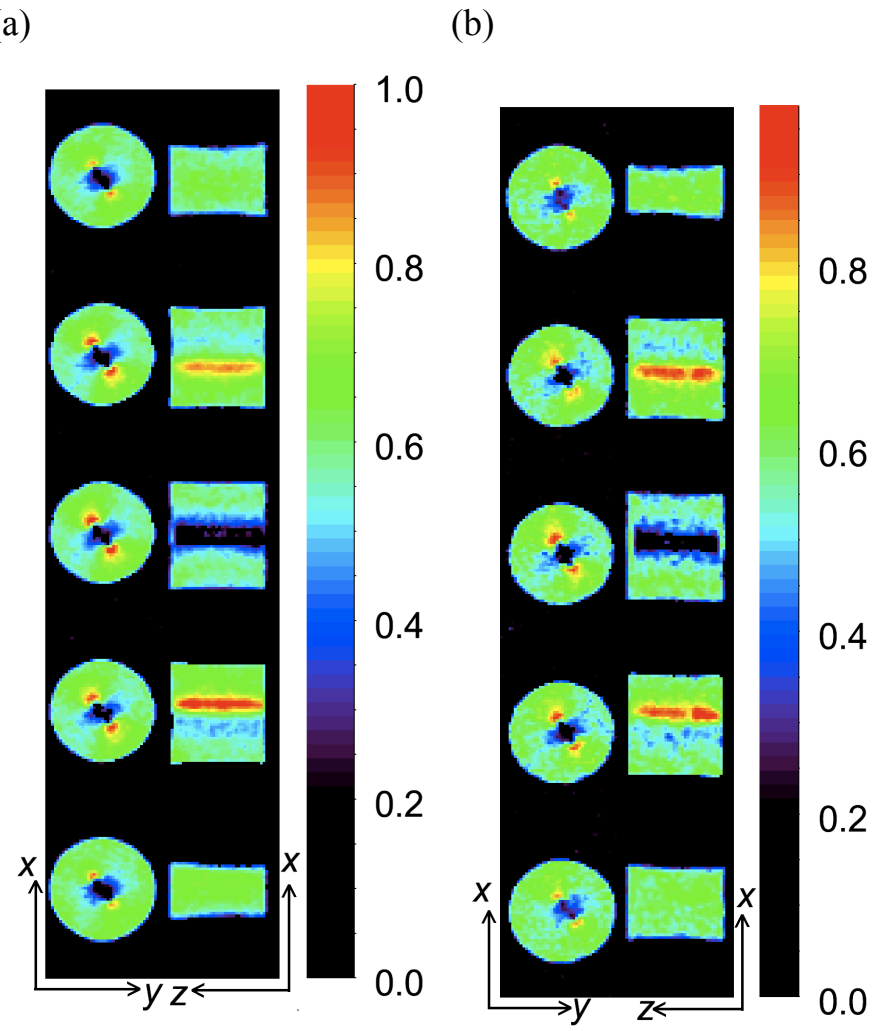

Figure 4-2 (a) and (b) 2D slices of the relative B_1 field distribution (B_1/B_{1max}) in the *xy* (to the left of each figure) and *xz* (to the right) planes. 2D slices are from 3D B_1 maps for a uniform vial of gel doped with $GdCl_3$ enclosing (a) a strip of Al or (b) a strip of Pb, for the geometry in Fig. 4-1a and 4-1b. For each orientation (*xy* and *xz*), five different planes, one in the centre of the object and four displaced from centre, are shown.

We now consider the second geometry of Fig. 4-1 in which the surface of the metal strip is parallel to B_1 and perpendicular to B_0. Fig. 4-3 shows 2D slices (*xz* and *xy* planes) from a 3D SPRITE image of a uniform vial of gel doped with $GdCl_3$ enclosing a strip of Al, Figs. 4-1c and 4-1d. The colour bar shows signal intensity in arbitrary units. For each orientation, one slice in the center of the object is shown. No B_1 distortions due

to RF eddy currents were observed in the 2D *xz* slices although B_1 is spatially heterogeneous as expected for a birdcage coil (see Chapter 3). B_1 artifacts will be minimized when the B_1 field is parallel to the surface of the strip (EMF ≈ 0 according to Eq. (4.1)). Note that eddy currents may still be induced in the thickness of the strip (0.23 cm), but they are negligible due to the geometry factor (surface S in Eq. (4.1) is very small). The results are in accordance with the theory (Eq. (4.1)); images are free from B_1 artifacts in this case. The 2D images are free from geometrical distortion due to switched magnetic field gradients or magnetic susceptibility variations.

The *xy* transverse 2D slice does show a petal shaped signal variation in proximity to the birdcage coil struts, Fig. 4-3, where the B_1 field is very strong. The struts on the left and right side of the metal strip surface in the *xy* slice were the reason for the signal enhancement at top and bottom of the *xz* slice in Fig. 4-3 (longitudinal slice).

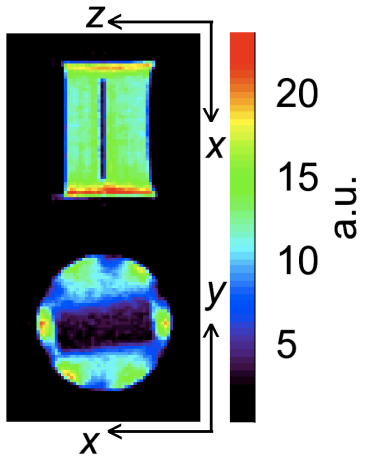

Figure 4-3 2D slices (*xy* and *xz* planes) from a 3D SPRITE image for a uniform vial of gel doped with $GdCl_3$ enclosing a strip of Al for the geometry in Fig. 4-1c and 4-1d. The colour bar shows signal intensity in arbitrary units. For each orientation one slice in the center of the object is shown. Signal enhancement occurs near the end of the sample in the *xy* and *xz* 2D slices are due to the strong B_1 field near the birdcage coil struts.

Since no $B_{1,ind}$ artifacts were observed for the case in which the surface of metal strip is parallel to B_1 and perpendicular to B_0, no simulations were undertaken. The $B_{1,ind}$ profoundly affects the first experimental geometry, Figs. 4-1a and 4-1b. Electromagnetic simulations were undertaken to match the experimental results to the theory. Fig. 4-4a illustrates the dimensions and orientations of the metal strips employed in the simulations. The dimensions were identical to the samples studied in Fig. 4-2. Note that the simulation axes (*x',y',z'*) are different from the imaging axes (*x,y,z*). They are rotated about the *z* axis by 45°.

The direction of the applied B_1 field, $B_{1y',app}$, was along *y'*. Fig. 4-4a shows a perspective view of the development of B_1 induced eddy currents when $B_{1y',app}$ is perpendicular to the surface of a metallic strip. According to Faraday's law of induction, Eq. (4.1), $B_{1y',app}$ induces an EMF which results in eddy currents. These eddy currents are concentrated at the edge of the metal strip due to the skin effect at high frequencies [18] resulting from a large attenuation constant α (theory section 4.2.2). The eddy currents induce a RF magnetic field $B_{1,ind}$. At the mid-point of the *z*-directed edge, $B_{1,ind}$ possesses only components in the *x'* ($B_{1x',ind}$) and *y'* ($B_{1y',ind}$) directions.

Fig. 4-4b shows a side on view of a central *x'y'* section (cross section view) of the metal strip in Fig. 4-4a. The induced eddy currents I+ and I− are into and out of the *x'y'* plane, respectively. The $B_{1,ind}$ fields are represented by the dashed lines, with a direction indicated by the arrowheads. The amplitude of the induced fields is inversely proportional to the distance from the current source in accordance with the Biot-Savart law [43]. In the proximity to the induced current, $B_{1,ind}$ effects are maximal. In areas far from the currents, the influence of $B_{1,ind}$ is minimal. At points shown by (×), midway between the

induced currents, the superposition of the induced fields exactly cancels out the applied field, giving a net magnetic field of zero. Knowing the direction and amplitude of $B_{1x',ind}$ and $B_{1y',ind}$, one can predict the direction and amplitude of the net B_1 field at each point in space ($B_{1i} = B_{1,ind} + B_{1,app}$, $i = x', y'$).

CST Microwave Studio was employed to simulate the spatial distribution of the magnetic field intensity $\vec{H}$ around the metal strip. $\vec{H}$ and magnetic flux density vector $\vec{B}$ are proportional by a constant of proportionality μ as shown in Eq. (4.9). In the simulations, the medium surrounding the electrode and gel was specified to be free space (i.e. and $\mu = \mu_0$, $\varepsilon = \varepsilon_0$).

The spatial distribution of the magnetic field intensities $H_{1x'}$ and $H_{1y'}$ in units of A/m from simulations, near and outside the modeled Al strip are shown in Figs. 4-5a and 4-5b. In each figure, a central *x'y'* plane is shown. The H_{1x} and H_{1y} distributions are superposition of $H_{1x',ind}$ and $H_{1y',ind}$ with the applied H_1, $H_{1,app}$, $H_{1i} = H_{1i,ind} + H_{1,app}$, $i = x', y'$. The extent of the region in which $H_{1,ind}$ is significant is proportional to the amplitude of the RF induced eddy currents. Large amplitude eddy currents will flow at low electrical resistance (high σ) and high EMF (induced voltage), resulting from the high rate of change of the applied magnetic flux (i.e. large $\frac{\partial \vec{B}_1}{\partial t}$). At high frequency, the impedance of the metal strip will be dominated by a reactive component ($Z_{metal} = R_{metal} + j\omega_0 L_{metal}$), thus the resistance of the metal, R_{metal}, will have negligible effects.

(a)

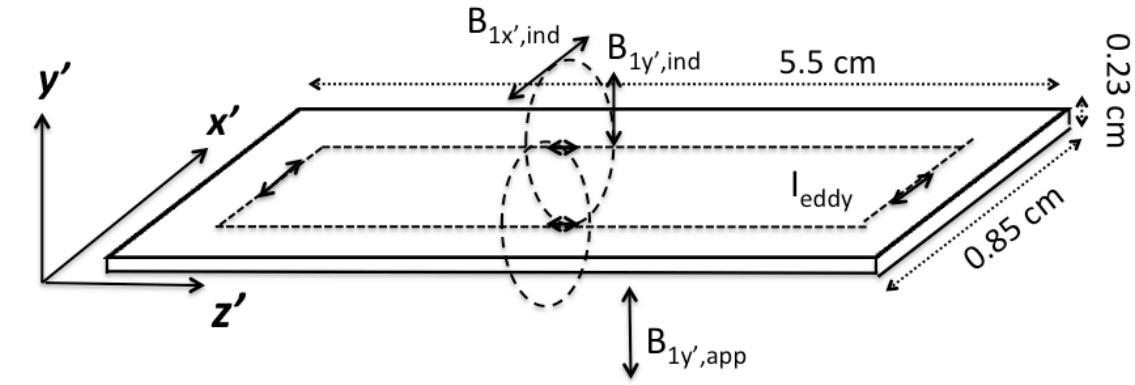

(b)

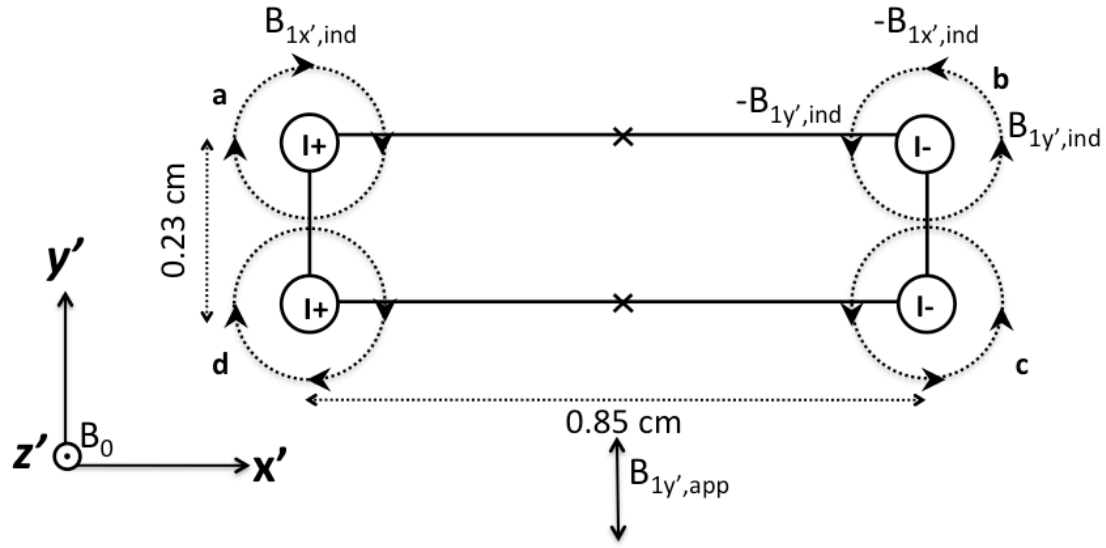

Figure 4-4 (a) The dimensions and orientations of the metal strips employed in the simulation. The simulation axes (*x'*,*y'*,*z'*) are different from the imaging axes (*x*,*y*,*z*). They are rotated about the *z* axis by 45°. A perspective view of the development of B_1 induced eddy currents in the metal when $B_{1y',app}$ is perpendicular to the surface of the metal strip is shown. (b) The side on view of a central *x'y'* cross section of the metal strip in (a). The induced eddy currents I+ and I− are into and out of the *x'y'* plane, respectively. The $B_{1,ind}$ fields are represented by the dashed lines. Arrows indicate the direction of the field. The $B_{1,ind}$ fields are represented by the dashed lines. Arrows indicate the direction of the field. At points shown by (×), midway between the induced currents, the superposition of the induced fields exactly cancels out the applied field, giving a net magnetic field of zero.

Calculations were also undertaken based on Eq. (4.4) for Al and Pb samples with the same geometry. Direct calculations show the effects are negligibly small (< 0.008% change in $j\omega_0 M/Z_{metal}$). Simulation results are in agreement with both the theory and the experimental results. Local changes of H_1 caused by the presence of metal are approximately the same (0.1% difference) for Al and Pb and are determined by the experimental geometry, which is identical. The electrical conductivity of the metal had negligible effects on the spatial distribution and amplitude of H_1.

Fig. 4-5a shows $H_{1x'}$, the superposition of $H_{1x',ind}$ and $H_{1,app}$ ($H_{1x'} = H_{1x',ind} + H_{1,app}$) near the Al strip. Note that $H_{1,app}$ is along the *y'* axis for this simulation so $H_{1x'}$ has the same amplitude and distribution as $H_{1x',ind}$. One can interpret the H_1 pattern as shown in Fig. 4-5a by considering the eddy current and $B_{1,ind}$ directions as shown in Figs. 4-4a and 4-4b, respectively. $H_{1x',ind}$ is directed along the +*x* axis at the top and bottom of loops **a** and **c**, respectively. Similarly, $H_{1x',ind}$ is directed along the -*x* axis at the top and bottom of loops **b** and **d**, respectively. The maximum of $H_{1'ind}$ occurs in the region near the induced current. The amplitude of $H_{1x',ind}$ decreases as the distance from the top and bottom of each loop increases although the orientation of the field does not change.

Fig. 4-5b shows H_{1y}, which is the superposition of $H_{1y',ind}$ and $H_{1y',app}$ ($H_{1y'} = H_{1y',ind} + H_{1y',app}$) near the Al strip. One can interpret the B_1 pattern as shown in Fig. 4-5b by considering the eddy current and $B_{1,ind}$ directions as shown in Figs. 4-4a and 4-4b, respectively. At the points on left side of the loops **a** and **d** as well as right sides of the loop **b** and **c**, $H_{1y',ind}$ is positive with maximum strength near the induced currents. Further from the currents the strength will be reduced. At points on right side of the loops **a** and **d** as well as left sides of the loop **b** and **c,** $H_{1y',ind}$ is along –*y*' with maximum

strength near the induced currents. The superposition of the induced fields exactly cancels out the applied field, resulting in a net magnetic field of zero at the midway points labelled as ($\times$) in Fig. 4-4b, midway between the induced currents.

Simulation was also undertaken to account for the effect of the gel with an electrical conductivity of 1 S/m. No effect of gel conductivity was observed (results not shown). However, simulation for a gel with higher electrical conductivity ($\sigma > 100$ S/m*)* showed the gel behaving more as an RF shield. The first term on the right hand side of Eq. (4.17) (penetration of $\vec{H}$ into the conductor), becomes relatively large and will be large inside the gel. Due to the skin effect, the electric current mainly flows near the surface of the conductive gel.

Simulations for both the Al and the Pb strips were performed. However, the results were essentially the same for both conductors. Therefore, only the results for the Al strips are reported in this work.

Note that the B_1 field was applied perpendicular to the strip surface, as shown in Fig. 4-1b, and the same RF coil was utilized for signal detection (detecting $B_{1y'}$ along *y'*). Based on the principle of reciprocity, the signal can be detected only along $B_{1,app}$ and only the $B_{1,ind}$ components corresponding to the $B_{1,app}$ direction produce a signal. Therefore, Fig. 4-5(b) $H_{1y'}$ distributions ($H_{1y'} = H_{1y',ind} + H_{1y',app}$) were compared with the experimental B_1 mapping results in Fig. 4-6.

(a) $H_{1x'}$ (b) $H_{1y'}$

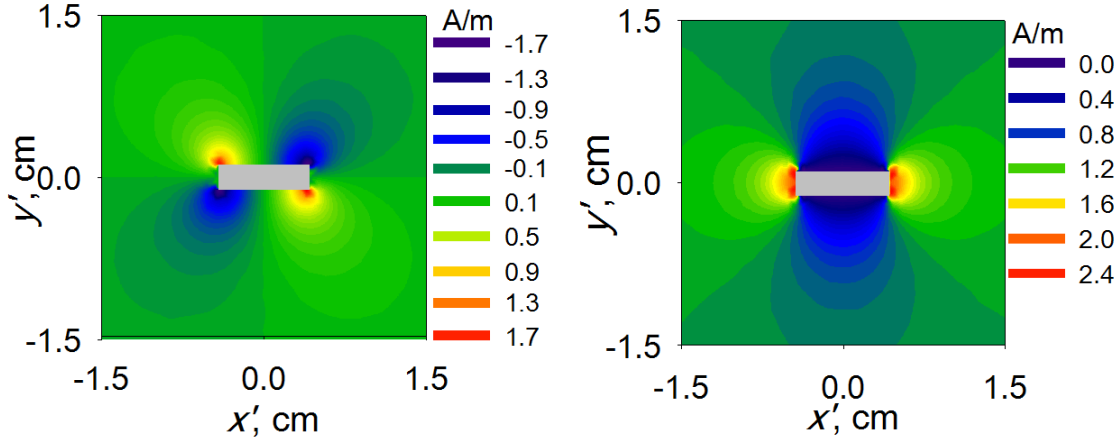

Figure 4-5 Magnetic field intensities $H_{1x'}$ and $H_{1y'}$ distributions from the simulation, outside the modeled Al strip for the geometry of Fig. 4-4b. H is measured in units of amperes per meter (A/m). (a) shows $H_{1x'}$ which is equal to $H_{1x',ind}$ near and around the Al strip. There is no component of applied field in the *x'* direction ($H_{1x',app} = 0$) (b) shows H_{1y} which is superposition of $H_{1y',ind}$ and $H_{1y',app}$ near and around the Al strip.

Figs. 4-6a and 4-6b show the central 2D slices of the relative B_1 field distribution (B_1/B_{1max}) (*xy* planes) produced from the B_1 mapping experiment for the Al and Pb strips, respectively. Figs. 4-6a and 4-6b are in a good agreement with Fig. 4-6c which is the normalized version of the results in Fig. 4-5b. The normalized version of Fig. 4-5b was employed to facilitate comparisons of local B_1 changes between the experimental and simulation results. In Fig. 4-6c H is replaced by B/μ in which μ will be cancelled in the normalization process ($B_1/B_{1max} = H_1/H_{1max}$). Local B_1 changes in the experiment and simulation are in excellent qualitative agreement.

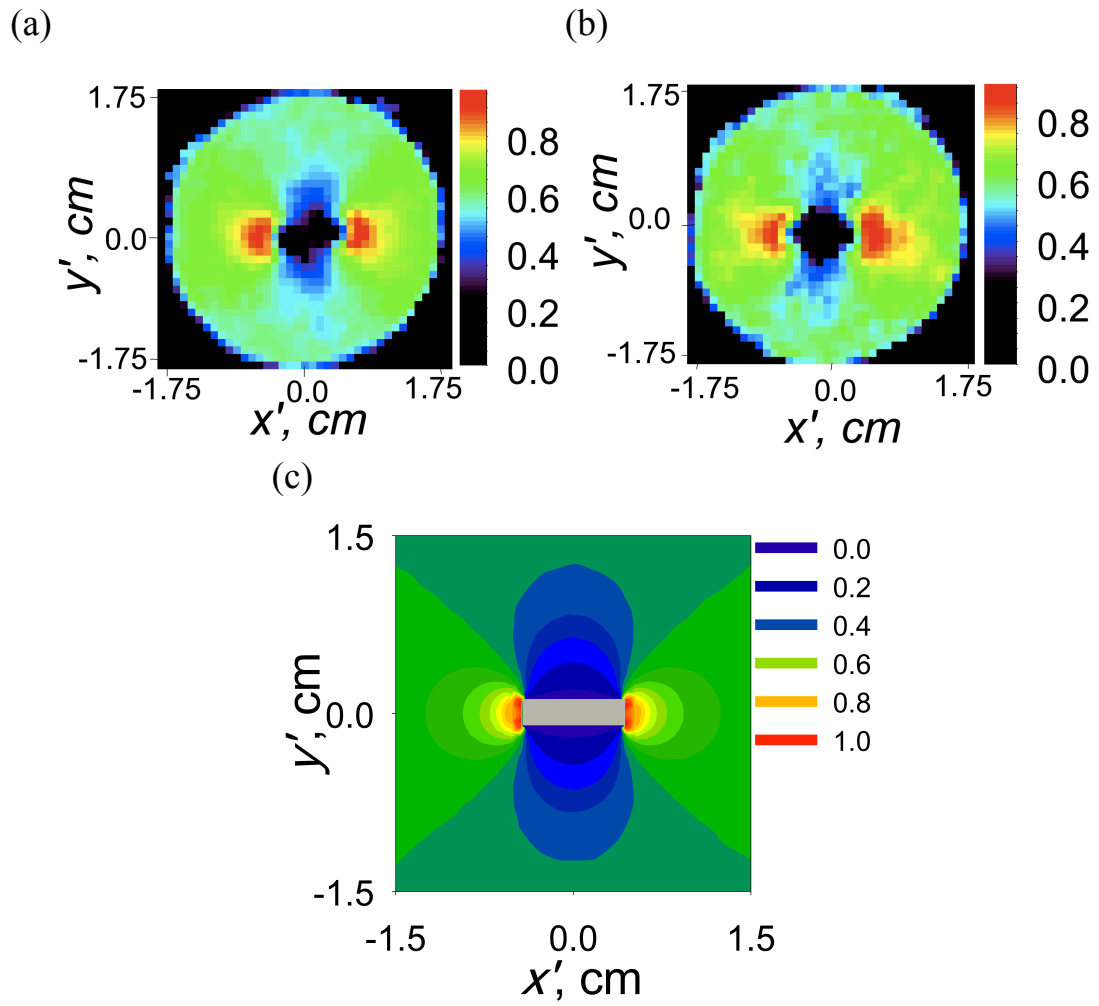

Figure 4-6 A comparison of relative B_1 distribution (B_1/B_{1max}) produced from the B_1 mapping experiment for the Al and Pb strips and the simulation result for the geometry in Figs. 4-4b. (a) and (b) show central 2D *xy* planes of the relative B_1 field distribution for Al and Pb, respectively. (c) shows normalized versions of the H_1 simulations as shown in Fig. 4-5b for the Al strip. The *x'* and *y'* axes were rotated to overlap the *x* and *y* axes in order to facilitate the comparison of the simulation and experimental results.

4.5 Conclusion

B_1 induced artifacts in the presence of metal strips which mimic electrodes were investigated. The B_1 induced distortions depend on the orientation between the metal strip

and the B_1 field. Two geometries were considered: (1) the surface of the metal perpendicular to B_1 and parallel to B_0 and (2) the surface of the metal parallel to B_1 and perpendicular to B_0. The first geometry lead to non-intuitive B_1 distortions, the second geometry was free from metal related B_1 artifacts.

A recently developed B_1 mapping technique was employed to measure distortions in the B_1 field in the presence of the metal strips for the first geometry. Simulations of B_1 field induced eddy currents were also undertaken. The B_1 induced eddy currents result in distortion of the B_1 field in the sample space for the first geometry. The B_1 simulation results were in good agreement with experimental results and illustrated the significant effects of the conductors on the B_1 field distribution and B_1 amplitude in surrounding space. The electrical conductivity of the metal has a negligible effect.

The results are particularly important for NMR and MRI of batteries and other electrochemical devices. In electrochemical MRI, orienting the electrodes such that they are largely parallel to the B_1 field (B_0 field either parallel or perpendicular) will significantly reduce B_1 eddy current induced effects.

The objects utilized in this work were electrode-like strips of metals, but one can employ the B_1 mapping experiment and/or simulations to quantify B_1 related effects around arbitrarily complex structures.

4.6 References

[1] M.M. Britton, P.M. Bayley, P.C. Howlett, A.J. Davenport, M. Forsyth, *In situ*, real-time visualization of electrochemistry using magnetic resonance imaging, J. Phys. Chem. Lett. 4 (2013) 3019-3023.

[2] Z. Zhang, J. Martin, J. Wu, H. Wang, K. Promislow, B.J. Balcom, Magnetic resonance imaging of water content across the Nafion membrane in an operational PEM fuel cell, J. Magn. Reson. 193 (2008) 259-266.

[3] R. Bhattacharyya, B. Key, H. Chen, A.S. Best, A.F. Hollenkamp, C.P. Grey, *In situ* NMR observation of the formation of metallic lithium microstructures in lithium batteries, Nature Materials 9 (2010) 504-510.

[4] L. Li. Q. Chen, A.E. Marble, L. Romero-Zeron, B. Newling, B.J. Balcom, Flow imaging of fluids in porous media by magnetization prepared centric-scan SPRITE, J. Magn. Reson. 197 (2009) 1–8.

[5] Q. Chen, B.J. Balcom, Measurement of rock core capillary pressure curves using a single-speed centrifuge and one dimensional magnetic resonance imaging, J. Chem. Phys. 122 (2005) 214720.

[6] Y. Zhao, Y. Song, T. Wang, Y. Liu, L. Jiang, N. Zhu, W. Yang Visualization of water flooding and subsequent supercritical CO_2 flooding in fractured porous media with permeability heterogeneity using MRI, Energy Procedia 37 (2013) 6942–6949.

[7] J.L.A. Williams, G. Maddinelli, D.G. Taylor, Selective magnetic resonance imaging of chemicals in sandstone cores during flow, J. Magn. Reson. 109 (1994) 124–128.

[8] M. Ouellette, H. Han, B. MacMillan, F. Goora, R. MacGregor, M. Hassan, B.J. Balcom, Design of a magnetic resonance imaging compatible metallic pressure vessel, J. Pres. Ves. Technol. 135 (2013) 045001-7.

[9] A.J. Ilott, S. Chandrashekar, A. Klöckner, H. Jung Chang , N.M. Trease, C.P. Grey, L. Greengard, A. Jerschow, Visualizing skin effects in conductors with MRI: Li MRI experiments and calculations, J. Magn. Reson. 245 (2014) 143-149.

[10] N. Augustiny, G.K. von Schulthess, D. Meler, P. Bosiger, MR imaging of large nonferromagnetic metallic implants at 1.5 T. J. Comput. Assist. Tomogr. 11 (1987) 678-683.

[11] J.S. Fache, C. Price, E.B. Hawbolt, D.K.B. Li, MR imaging artifacts produced by dental materials. Am. J. Neuroradiol. 8 (1987) 837-840.

[12] C.R. Camacho, D.B. Plewes, R.M. Henkelman, Nonsusceptibility artifacts due to metallic objects in MR imaging, J. Magn. Reson. Imaging 5 (1995) 75-88.

[13] L.H. Bennett, P.S. Wang, M.J. Donahue, Artifacts in magnetic resonance imaging from metals, J. Appl. Phys. 79 (1996) 4712-4714.

[14] A. Shenhav, H. Azhari, Gradient field switching as a source for artifacts in MR imaging of metallic stents, Magn. Reson. Med. 52 (2004) 1465-1468.

[15] U.A. Lauer, H. Graf, A. Berger, C.D. Claussen, F. Schick, Radio frequency versus susceptibility effects of small conductive implants: a systematic MRI study on aneurysm clips at 1.5 and 3 T, Magn. Reson. Imaging 23 (2005) 563-569.

[16] H. Graf, U.A. Lauer, A. Berger, F. Schick, RF artifacts caused by metallic implants or instruments which get more permanent at 3 T: an in vitro study, Magn. Reson. Imaging 23 (2005) 493-499.

[17] H. Graf, G. Steidle, U.A. Lauer, F. Schick, RF enhancement and shielding in MRI caused by conductive implants: dependence on electrical parameters for a tube model, Med. Phys. 32 (2005) 337-342.

[18] H. Graf. G. Steidle, P. Martirosian, U.A. Lauer, F. Schick, Effects on MRI due to altered RF Polarization near conductive implants or instruments. Med. Phys. 33 (2006) 124-127.

[19] S. Posse, W.P. Aue, Susceptibility artifacts in spin-echo and gradient-echo imaging. J. Magn. Reson. 88 (1990) 473-492.

[20] C.J.G. Bakker, R. Bhagwandien, M.A. Moerland, M. Fuderer, Susceptibility artifacts in 2DFT spin-echo and gradient-echo imaging: the cylinder model revisited, Magn. Reson. Imaging 11 (1993) 539-548.

[21] M. O'Donnell, W.A. Edelstein, NMR imaging in the presence of magnetic field inhomogeneities and gradient field nonlinearities, Med. Phys. 12 (1985) 20-26.

[22] A. Ericsson, A. Hemmingsson, B. Jung, G.O. Sperber, Calculation of MRI artifacts caused by static field disturbances. Phys. Med. Biol .10 (1988) 1103-1112.

[23] H. Imai, Y. Tanaka, N. Nomura, Y. Tsutsumi, H. Doi, Z. Kanno, K. Ohno, T. Ono, T. Hanawa, Three-dimensional quantification of susceptibility artifacts from various metals in magnetic resonance images, Acta. Biomater. 9 (2013) 8433-8439.

[24] J.K. Kim, D.B. Plewes, R.M. Henkelman, Phase constrained encoding (PACE): a technique for MRI in large static field inhomogeneities, Magn. Reson. Med. 33 (1995) 497-505.

[25] K. Sekihara, S. Matsui, H. Kohno, NMR imaging for magnets with large inhomogeneities. IEEE. Trans. Med. Imaging 4 (1985) 193-199.

[26] Z.H, Cho, D.J. Kim, Y.K. Kim, The total inhomogeneity correction including chemical shift and susceptibility by view angle tipping, Med. Phys. 15 (1988) 7-11.

[27] H. Chang, J.M. Fitzpatrick, A technique for accurate magnetic resonance imaging in the presence of field inhomogeneites, IEEE Trans. Med. Imaging 11 (1992) 319-329.

[28] F.G. Goora, H. Han, B.G. Colpitts, B.J. Balcom, Simulation and verification of magnetic field gradient waveforms in the presence of a metallic vessel in magnetic resonance imaging, IEEE Trans. Magn. 48 (2012) 2440-2448.

[29] F.G. Goora, H. Han, M. Ouellette, B.G. Colpitts, B.J. Balcom, Investigation of magnetic field gradient waveforms in the presence of a metallic vessel in magnetic resonance imaging through simulation, IEEE Trans. Magn. 49 (2013) 2920-2932.

[30] W.R. Nitz, A. Oppelt, W. Renz, C. Manke, M. Lenhart, J. Link, On the heating of linear conductive structures as guide wires and catheters in interventional MRI, J. Magn. Reson. Imaging 13 (2001) 105-114.

[31] K. El Banan, W. Handler, B. Chronik, S.P. Salisbury, Heating of metallic rods induced by time varying gradient field in MRI, J. Magn. Reson. Imaging 38 (2013) 411-416.

[32] H. Han, B. Balcom, Magnetic resonance imaging inside metallic vessels, Meas. Sci. Technol. 21 (2010) 1-5.

[33] H. Han, M. Ouellette, B. MacMillan, F.G. Goora, R. MacGregor, D. Green, B.J. Balcom, High pressure magnetic resonance imaging with metallic vessels, J. Magn. Reson. 213 (2011) 90-97.

[34] P. Stradiotti, A. Curti, G. Castellazzi, A. Zerbi, Metal-related artifacts in instrumented spine. Techniques for reducing artifacts in CT and MRI: state of the art, Eur. Spine. J. 18 (2009) 102-108.

[35] S. Gravina, D.G. Cory, Sensitivity and resolution of constant-time imaging, J. Magn. Reson. 104 (1994) 53-61.

[36] B.J. Balcom, R.P. MacGregor, S.D. Beya, D.P. Green, R.L. Armstrong, T.W. Bremner, Single-point ramped imaging with T_1 enhancement (SPRITE), J. Magn. Reson. 123 (1996) 131-134.

[37] M. Halse, D. J. Goodyear, B. MacMillan, P. Szomolanyi, D. Matheson, B.J. Balcom, Centric scan SPRITE magnetic resonance imaging, J. Magn. Reson. 165 (2003) 219-229.

[38] M.F. Lee, S. Kim, S.A. Lee, H.T. Song, Y.M. Huh, D.H. Kim, S.H. Han, J.S. Suh, Overcoming artifacts from metallic orthopedic implants at high-field-strength MR imaging and multidetecter CT: RadioGraphics 27 (2007) 791-803.

[39] M.J. Lee, D.L. Janzen, P.L. Munk, A. MacKay, Q.S. Xiang, A. MacGowen, Quantitative assessment of an MR technique for reducing metal artifact: application to spin-echo imaging in a phantom. Skeletal Radiol. 30 (2001) 398-401.

[40] H.G. Potter, B.J. Nestor, C.M. Sofka, S.T. Ho, L.E. Peters, E.A. Salyati,
Magnetic resonance imaging after total hip arthoplasty: evaluation of periposthetic soft tissue, J. Bone Joint. Surg. Am. 86 (2004) 1947-1957.

[41] S. Vashaee, B. Newling, B. MacMillan, B.J. Balcom, B_1 mapping with a pure phase encode approach, J. Magn. Reson. 232 (2013) 68-75.

[42] C. A. Balanis, Advanced Engineering Electromagnetics. Reading Massachusetts Addison Wesley, Inc. USA, 1989.

[43] D.K. Cheng, Field and Wave Electromagnetics, second ed., Addison-Wesley , Inc. USA, 1989.

[44] E. Fukushima, S.B.W. Roeder, Experimental pulse NMR, Addison-Wesley, Massachusetts, USA, 1981.

[45] T. Weiland, Time domain electromagnetic field computation with finite difference methods, Int. J. Numer. Model. El. 9 (1996) 295-319.

Chapter 5 - Region of Interest Selection of Long Core Plug Samples by Magnetic Resonance Imaging: Profiling and Local T_2 Measurement

In Chapter 3, B_1 maps were employed to correct non-uniformity over 1D axial profiles of porous media. In this chapter, a second approach is introduced for quantitative density profiling of porous media. When the sample of interest is longer than sensitive region of the RF probe and the region of constant magnetic field gradient, as shown in Fig. 5-1, the profiles may be heavily distorted and non-quantitative. An adiabatic inversion pulse, which is insensitive to B_1 non-uniformities, is applied in the presence of a slice selective magnetic field gradient to select a small portion (a "slice" or a "slab") of a long sample. An adiabatic inversion pulse slice selection lends itself to a selective T_2 distribution measurement when a CPMG pulse sequence follows the slice selection.

This chapter is largely based on the paper "Region of interest selection of long core plug samples by magnetic resonance imaging: profiling and local T_2 measurement" published in the journal Measurement Science and Technology, 25 (2014) 035004-0350014. The format of references in this chapter follows that of the original article.

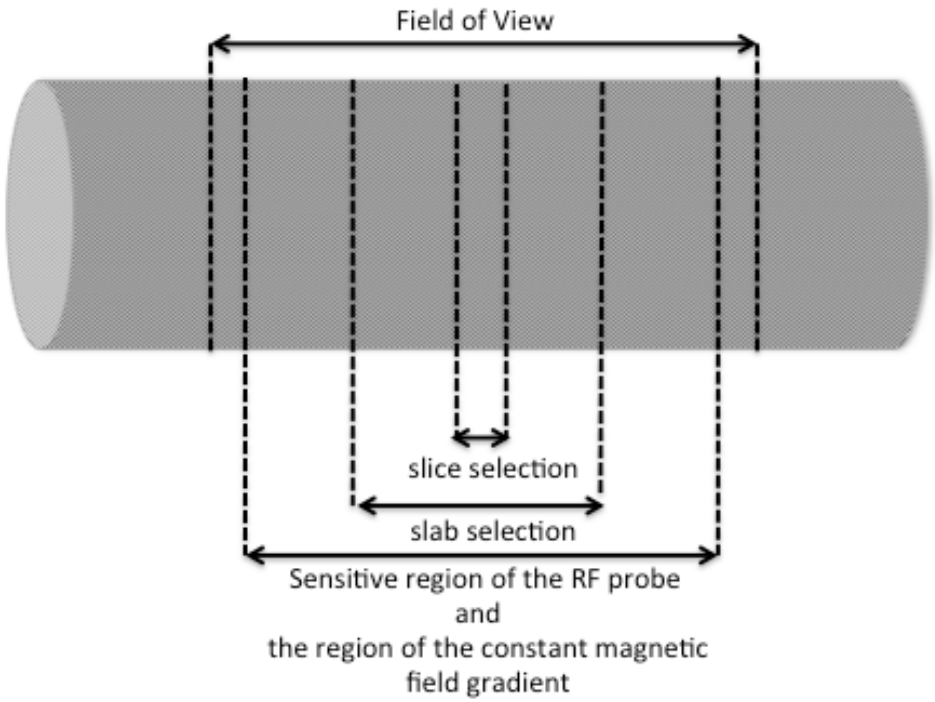

Figure 5-1 A sample of interest longer than sensitive region of the RF probe and the region of constant magnetic field gradient. Slice selection and slab selection are in order of a few millimeters and a few centimeters, respectively.

Abstract

Magnetic resonance imaging (MRI) is increasingly employed as a core analysis technique by the oil and gas industry. In axial profiling of petroleum reservoir core samples and core plugs, the sample of interest may frequently be much longer than the natural field of view (FOV) defined by the radio frequency (RF) sensor and region of constant magnetic field gradient. Profiling such samples with a low field MRI will result in distorted, non-quantitative axial profiles near the edge of the FOV with data from outside the desired FOV folding back into the image, when the gradient magnetic field homogenity region is shorter than the region of RF excitation. The quality of MRI as a

core analysis technique is increased if imaging can be performed on intact samples with the FOV reduced to the region of interest (ROI), either to increase the image resolution or to reduce the total time for imaging. A spatially selective adiabatic inversion pulse is applied in the presence of a slice selective magnetic field gradient to restrict the FOV to an ROI that is a small portion of a long sample. Slice selection is followed by a 1D centric-scan SPRITE measurement to yield an axial fluid density profile of the sample in the ROI. By employing adiabatic pulses, which are immune to RF field non-uniformities, it is possible to restrict the ROI to a region of homogeneous RF excitation, facilitating quantitative imaging. The method does not employ conventional selective excitation, but a subtraction based on images acquired with and without adiabatic inversion slice selection.

The adiabatic slice selection lends itself to a selective T_2 distribution measurement when a CPMG pulse sequence follows the slice selection. The inversion pulse selects a slice on the order of 1 cm at an arbitrary position. The local T_2 distributions measured are of similar quality to bulk CPMG. This method is an alternative to MRI-based techniques for T_2 mapping in short relaxation time samples in porous media when T_2 is required to be measured at only a few positions along the sample, and a resolution of 1 cm is acceptable.

This chapter is largely based on the paper "Region of interest selection of long core plug samples by magnetic resonance imaging: profiling and local T_2 measurement" published in the journal Measurement Science and Technology, 25 (2014) 035004-0350014. The format of references in this chapter follows that of the original article.

5.1 Introduction

Magnetic resonance imaging (MRI) is commonly employed for clinical diagnostic imaging but its routine application to spatially resolved analysis of fluids in porous media is still developing. Bulk magnetic resonance analysis of fluids in reservoir cores and core plugs, measuring absolute fluid content and relaxation time distributions, is a routine part of petroleum reservoir core analysis.

Recent developments in quantitative MRI of reservoir rock core plugs have led to the development of new core analysis methods for capillary pressure, and other measurements [1-8]. MR core analysts seek to measure samples of increasing length.

Centric-scan SPRITE MRI is employed for spin density measurements of rocks [9-11], due to its reliability and immunity to image distortions caused by magnetic susceptibility variation, chemical shift and paramagnetic impurities. SPRITE has inherently no slice selection and therefore requires a more sophisticated approach to limit the region of interest (ROI). In axial profiling of petroleum reservoir core samples and core plugs, the samples of interest may frequently be much longer than the natural field of view (FOV) defined by the radio frequency (RF) probe and region of constant magnetic field gradient. Axial profiling of such samples will result in distorted, non-quantitative profiles near the edge of the FOV due to RF field variation and nonlinear magnetic field variations. In order to solve this problem, and to better resolve small portions of the sample, spatially selective RF pulses may be adapted from clinical MRI to restrict the interrogation to an ROI [12-16] that is a small section of the long core sample.

In this work a technique has been developed to produce an axial profile of the ROI within an extended sample. The experimental goal is slab selection with subsequent

1D imaging in the slab direction, not orthogonal to the slab. A "slab" is a rather thick slice of interest between 1 and 6 cm. MRI derives much of its efficacy from the detection of signals spatially localized to specific ROIs. This is typically accomplished by a combination of methods including selective excitation and outer volume suppression (OVS) [17-34]. Selective excitation is a routine technique in MRI and conventionally rotates the longitudinal magnetization in the slice of interest into the transverse plane [35]. Magnetization in the slice then begins to change through T_2^* and T_2 decay processes. This process will be particularly problematic for a fluid saturated porous medium, where a T_2 distribution is common, and where one wishes in the first instance to generate a map of fluid content. T_2^* and T_2 are characteristic MR exponential decay time constants [36, 37]. In the most common OVS approach, signal suppression is achieved by exploiting one or more frequency-selective pulses that convert the initial magnetization M_0 into transverse magnetization M_{xy} that is subsequently dephased by pulsed magnetic field gradients. Such OVS approaches generally provide excellent signal suppression, provided the RF field is relatively homogeneous so that each position in the sample experiences a flip angle of 90°.

It is natural to consider a spatial localization methodology, which involves manipulating the longitudinal magnetization in the slice. The selected magnetization will evolve from a non-equilibrium condition according to the local T_1. The T_1 time constant describes the initial development of the sample magnetization when placed in the $\vec{B}_0$ magnetic field and recovery of equilibrium longitudinal magnetization after perturbation.

T_1 will also be a distribution, however in porous media T_1 is always substantially longer than T_2 [38].

In the technique herein presented, a frequency-selective adiabatic inversion pulse [39] is applied in the presence of a slice selective magnetic field gradient. This is followed by 1D centric-scan SPRITE [9, 16] to yield an axial profile, which includes an inverted slice within a long core sample. The imaging sequence is applied a second time without the ROI selection to yield an axial profile of the whole sample. The difference of these two profiles yields an axial profile of the ROI alone, with the signal from out-of-slice regions suppressed. This slab selection procedure may be naturally considered an M_z magnetization preparation procedure with a centric-scan SPRITE density imaging read out [17]. This method is conceptually similar to the ISIS technique for spatial localization but its application to porous media and to the determination of the T_2 relaxation time distribution is our goal [40 -42].

Since the slab selection technique ensures the magnetization out of the slice is completely suppressed one can perform the imaging experiment with reduced FOV in order to increase the resolution or to reduce the phase encode imaging time [12-16].

Bulk CPMG can be employed to measure T_2 at different positions with adiabatic slice selection. Other slice selective CPMG sequences have been previously employed in the suppression of unwanted spectral components in T_2 decays. CPMG sequences have been employed with E-BURP-2 [43], RE-BURP [44] and TROSY selection [45] and DANTE-Z slice selection [46]. The advantage of slice selective CPMG employing adiabatic inversion is the immunity to RF field variation.

5.2 Material and methods

5.2.1 Hyperbolic secant frequency-selective adiabatic inversion pulse

Adiabatic pulses are amplitude and frequency modulated pulses, which are widely employed in MR and MRI [39, 47-55]. The sweep of RF pulse frequency from one side of resonance (Larmor frequency, ω_0) to the other generates an RF magnetic field, $\vec{B}_1$ which causes a rotation of sample magnetization $\vec{M}$. The net rotation is insensitive to changes in the RF field amplitude, which is a feature of the adiabatic pulse approach. In the frame rotating at the Larmor frequency ω_0, $\vec{M}$ will precess about the effective RF field ($\vec{B}_{eff}$), Fig 5-2. For a pulse with a frequency which differs from ω_0 by $\Delta\omega$ this effective field is given by [15]:

$$\vec{B}_{eff} = \vec{B}_1 + \frac{\Delta\omega}{\gamma}\hat{z}' \qquad \textbf{(5.1)}$$

As is indicated in Fig. 5-2 the adiabatic sweep is described by rotation of $\vec{B}_{eff}$ with angular velocity $\vec{\Omega}$, which is perpendicular to the plane formed by the direction of $\vec{B}_1$ and z' (aligned with $\vec{B}_0$). The trajectory of $\vec{B}_{eff}$ is generally considered in a frame of reference (x', y', z') rotating at the instantaneous frequency of the RF pulse. The $\vec{B}_{eff}$ axis is shown in Fig. 5-2. In adiabatic fast passage the orientation of $\vec{B}_{eff}$ is changed in such a manner that $\vec{M}$ is able to follow $\vec{B}_{eff}$ throughout the pulse that is the angle between them remains sufficiently small.

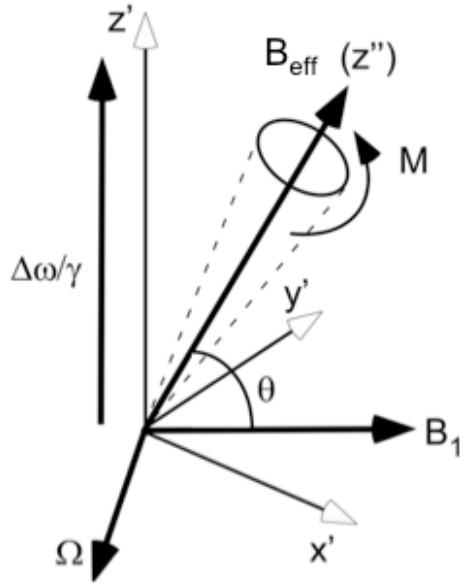

Figure 5-2 The effective magnetic field in the reference frame rotating with the instantaneous radio frequency (RF) pulse frequency. The adiabatic sweep is described by a rotation with angular velocity of $\vec{\Omega}$, Ω = dθ/dt. The axis *z"* rotates with the effective field.

The rate of change of orientation of $\vec{B}_{eff}$ (Ω = dθ/dt) must be sufficiently slow that $\vec{M}$ is able to follow $\vec{B}_{eff}$. Eq. (5.2) represents the condition for adiabaticity in which $\gamma\vec{B}_{eff}$ is the angular velocity of $\vec{M}$ about $\vec{B}_{eff}$ as it precesses:

$$\left|\vec{\Omega}\right| << \left|\gamma\vec{B}_{eff}\right| \qquad \textbf{(5.2)}$$

Adiabatic rotations must be accomplished rapidly relative to the relaxation times T_1 and T_2. Thus the process is called adiabatic fast passage [39, 49, 53, 54, 56]:

$$\frac{2\pi}{T_2} << \left|\vec{\Omega}\right| << \left|\gamma\vec{B}_{eff}\right| \qquad \textbf{(5.3)}$$

If the conditions expressed in Eq. (5.3) are satisfied, spins in the ROI are inverted in manner that avoids T_2 contrast and minimizes T_1 and $T_{1\rho}$ contrast ($T_1 > T_2$ and $T_{1\rho} > T_2$) so as to maintain a density contrast in the final image. ($T_{1\rho}$ is the relaxation time constant, which describes evolution of nonequilibrium sample magnetization, like T_1 but in the presence of an RF field.)

Master equations designed by Tesiram and Bendall, based on numerical analysis of hyperbolic secant adiabatic inversion pulses, were employed to design optimum adiabatic pulses [57]. The amplitude and frequency modulations were as follows:

$$B_1(t) = RF_{\max}\operatorname{sech}\beta\left(1-\frac{2t}{T_p}\right) \qquad \textbf{(5.4)}$$

$$\Delta\nu = \left(\frac{bw}{2}\right)\left[\tanh\beta\left(1-\frac{2t}{T_p}\right)+s\right] \qquad \textbf{(5.5)}$$

where the amplitude truncation is determined by sech $\beta = 0.01$ and $\beta = 5.3$, T_p is the pulse duration in milliseconds, RF_{max} is the necessary maximum amplitude in kHz and the frequency sweep is $\pm bw/2$ in kHz. The bw (bandwidth) can be written as $2\mu\beta$. The parameter μ is dimensionless and determines the degree of phase modulation while β gives the amplitude truncation level. Dimensionless parameter s is the resonance offset of the pulse, where $s = 0$ denotes an on resonance pulse. Since, in the spectrometer employed, the RF pulse is applied in amplitude and phase form, the frequency modulation equation changes to a phase modulation equation as follows:

$$\phi(t) = \pi\,(bw)\left(\frac{-T_p}{2}\right)\left[\frac{1}{\beta}\ln\left|\cosh\beta\left(1-\frac{2t}{T_p}\right)\right|\right] \qquad \textbf{(5.6)}$$

For experimental application of hyperbolic secant pulses, the universal expression below, that forms the basis of the Eqs. (5.4) and (5.5), should be employed [57]:

$$(RF_{\max}T_p)^2 = m_{RF}T_p bw + c_{RF} \qquad \textbf{(5.7)}$$

Excellent linear plots of $(RF_{max}T_p)^2$ or (total power) versus T_p bw for the hyperbolic secant pulses were obtained by Tesiram and Bendall [57]. There is an increasing divergence of data from the fitted straight lines for T_p bw products less than 10, resulting from violation of the adiabatic condition. m_{RF} and c_{RF}, the slope and intercept of Eq. (5.7), can be calculated by employing Eqs. (5.8) and (5.9).

$$\frac{1}{m_{RF}^2} = -2.695\,l_0 + 2.809 \qquad \textbf{(5.8)}$$

$$\frac{1}{c_{RF}} = 2.885\,l_0 - 2.999 \qquad \textbf{(5.9)}$$

l_0 (inversion number) is the amount of $-z$ magnetization after the pulse at the centre of the inversion profile and percent inversion is defined as:

$$\text{percent inversion} = 50\,(1 + l_0) \qquad \textbf{(5.10)}$$

The degree to which the inversion number l_0 is allowed to deteriorate, $\Delta l = l_0 - l_{bw}$, at the extremes of bw_{eff} (effective bandwidth), must be selected. One must choose a

minimum inversion number, l_{bw}, defining the bw_{eff}, and thus an acceptable inversion quality across the ROI. For the hyperbolic secant pulses Δl should be chosen so that the profile wobbles in the shoulder region lie above the l_{bw} value defining bw_{eff}. For experimental application in the presented method, the values $l_0 = 0.996$, $l_{bw} = 0.98$ and $\Delta l = 0.016$ were chosen.

The bw_{eff} is always less than bw because the frequency profile for a hyperbolic secant pulse is not perfectly rectangular and bw reflects the width of the profile at half height. Plots of the dimensionless quantities $T_p bw_{eff}$ versus $T_p bw$ are always linear, Thus the following equation was obtained that is in agreement with Eq. (5.8), [57]:

$$T_p bw_{eff} = T_p bw - c_{bw} \qquad \textbf{(5.11)}$$

In accordance with [57], when $\Delta l < 0.09$, as in the current case, the value for c_{bw} can be obtained from the following equation:

$$c_{bw} = (0.85\Delta l + 0.025)^{-0.5} + 1 \qquad \textbf{(5.12)}$$

For experimental application one needs to know the appropriate values of RF_{max}, T_p, and bw for a chosen effective bandwidth, bw_{eff}, and a chosen amount of inversion guaranteed across bw_{eff}. According to [57] the adiabatic condition will not be satisfied for $T_p bw$ values less than 10. We satisfy the inequality by choosing $bw_{eff} = 15$ kHz and $T_p = 1.5$ ms. bw is then obtained by employing Eq. (5.11). Eqs. (5.8) and (5.9) were applied to obtain m_{RF} and c_{RF} for $l_0 = 0.996$ to guarantee the chosen amount of inversion across

bw_{eff}. Knowledge of values for T_p, bw, c_{RF} and m_{RF}, permits us to calculate RF_{max}, the necessary maximum amplitude, to be 5.7 kHz from Eq. (5.7).

5.2.2 1D centric-scan (dhk) SPRITE imaging

To measure axial profiles of the sample and the ROI inverted by the hyperbolic secant pulse, the 1D SPRITE method (dhk SPRITE) was employed [9]. The experimental goal is a density profile and this is naturally the case for dhk SPRITE. In an MRI measurement the signal acquired in the presence of a magnetic field gradient G is a sample of a reciprocal space ($\vec{k}-$space) defined by:

$$\vec{k} = \frac{\gamma}{2\pi}\int_0^{t_p} \vec{G}\, dt \qquad \textbf{(5.13)}$$

where t_p is the encoding time. SPRITE is a constant time or pure-phase encode MRI measurement [58-60] because $\vec{k}-$space is sampled one point at a time for fixed t_p while changing the value of $\vec{G}$.

In the dhk SPRITE method the centre point of $\vec{k}-$space is first acquired and then subsequent $\vec{k}-$space points are acquired with additional RF pulses as the phase encode gradient increments. This removes T_1 weighting from the image acquired with appropriate measurement parameters. Fig. 5-3 shows the imaging sequence that was employed.

5.2.3 ROI selection employing adiabatic inversion dhk SPRITE and subtraction method

The experiment consists of two successive scans. In the first scan the magnetization will be inverted for the selected slice, M_{slice}. M_{slice} is along $-z$ in the slice. But everywhere else M_{rest} is along $+z$. Thus the first scan is a regular SPRITE experiment for M_{rest}, while for M_{slice} it is a SPRITE experiment with a prepared (inverted) magnetization. In the second scan, the adiabatic inversion pulse is not applied, so at the beginning of the SPRITE acquisition the sample magnetization is along $+z$. The second scan is a regular SPRITE experiment. To produce the 1D profile from the selected slice only, the first scan should be subtracted from the second one. Such a subtraction eliminates M_{rest} out of the slice and doubles M_{slice}. The subtraction can be accomplished employing real and imaginary parts of either the profiles or the signal in k -space. The evolution of prepared and unprepared magnetization during SPRITE acquisition and cancelling the unprepared magnetization after subtraction is described in detail in [1].

5.2.4 Adiabatic inversion CPMG sequence

The adiabatic inversion pulse may be combined with a bulk CPMG pulse train as shown in Fig. 5-3b. T_1 recovery of the inverted slice in adiabatic inversion CPMG takes place between the adiabatic inversion and the CPMG sequence (~500 μs for this paper). The 90° pulse of the CPMG sequence rotates the magnetization from the $-z$ axis to the *xy*-plane, just as in the first (non-selecting, or bulk CPMG) scan. The only difference from the T_1 relaxation point of view between those two scans is the T_1 recovery during

the 500 μs interval after the adiabatic inversion. If T_1 is considerably longer than 500 μs, the effect will be negligible. This T_1 effect is described in [1]

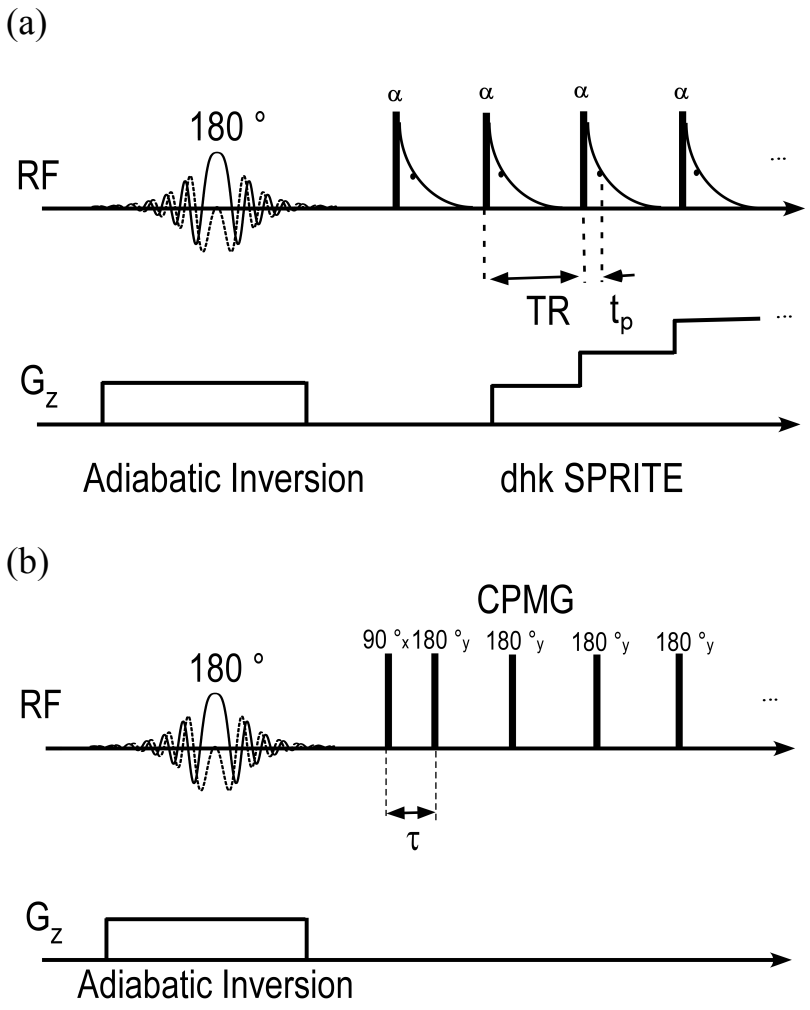

Figure 5-3 (a) 1D axial profiling of a ROI within the sample is achieved by the application of the hyperbolic secant pulse in the presence of a slice selective gradient is followed by a dhk SPRITE acquisition. One half of k-space is sampled and then, after a delay $5T_1$, the hyperbolic secant pulse is repeated and the second half of k-space is sampled. The imaging RF pulses are applied at intervals of TR. A single point from the FID is collected after the phase encoding time t_p. (b) An alternative use of the adiabatic inversion measures a localised T_2. The adiabatic inversion in the presence of a slice selective gradient is followed by a CPMG pulse sequence. 2τ is the interval between the 90^o and the first echo.

5.3 Experimental

ROI measurements were performed on a MARAN DRX spectrometer (Oxford Instruments Ltd, Oxford, UK) with a horizontal bore superconducting magnet (GE NMR 2T/31 magnet system, charged to 0.35 T), employing a home-built 3-axis gradient set with a maximum amplitude of 150 G/cm. A set of three Techron 8606 gradient amplifiers were employed for the imaging measurement. A home-built birdcage RF probe was employed with a 300 W RF power amplifier (Resonance Instruments Ltd, Oxford, UK). All measurements were carried out at ambient magnet temperature of 15 ^{0}C. A Berea reservoir sandstone core plug, 22.5 cm in length and 2.5 cm in diameter, was employed for the experiment. This long core was formed by three 7.5 cm length samples placed end to end to simulate a long core sample. After water saturation, the bulk relaxation times were T_2^* = 572 us, $T_2(1)$ = 18 ms, 54%; $T_2(2)$ = 108 ms, 46 % with T_2 modelled as a bi-exponential decay, $T_2(1)$ and $T_2(2)$ labelled the two exponential decay components. The T_1 was essentially single exponential at 200 ms.

Magnetization preparation and dhk SPRITE imaging sequence parameters were: hyperbolic secant adiabatic inversion T_p = 870 μs, pulse bandwidth = 33 kHz, FOV = 128 mm; filter width = 125 kHz; 64 k-space points were acquired with a phase encoding time of t_p = 130 μs. Although the applied T_p was less than the 1.5 ms employed during the pulse design, the T_pbw product remains constant and so the adiabatic condition is still met. The dhk SPRITE RF pulses were 1.4 μs in duration (8.4^o flip angle) with a repetition time of TR = 2 ms. 32 k-space points were acquired per inversion. Typical profile images were acquired in 1 min and 6 s with 32 signal averages. The phase cycle for the hyperbolic secant pulse (slice selective pulse) and SPRITE RF pulses were $X\bar{X}Y\bar{Y}$ and

for the receiver phase was $\bar{X}X\bar{Y}Y$. Three different magnetic field gradient strengths were applied in slice selection to obtain three different slice thicknesses (*Gss* = 2.5, 2, and 1.6 G/cm). The time interval between slice selection and commencement of the dhk SPRITE sequence was chosen to be 300 μs. This time was required for the slice selective gradient to switch off and was chosen to be much less than T_1 to minimize T_1-mediated recovery of magnetization in the inverted slice.

Slice selective T_2 measurements were performed on a Maran DRX-HF (Oxford Instruments Ltd, Oxford, UK) 0.2 T permanent magnet. The RF probe was a vertical solenoid 10 cm in diameter and 20 cm in length, driven by a 1 kW 3445 RF amplifier (TOMCO Technologies, Sydney, Australia). A shielded three-axis gradient coil driven by *x, y, z* Techron (Elkhart, IN) 7782 gradient amplifiers, provided maximum gradients of 26 G/cm, 24 G/cm and 33 G/cm in this work.

Adiabatic inversion CPMG was tested using a stack of three cylindrical vials of water 1 cm in diameter, doped with $GdCl_3$. T_2 of the doped water was 16 ms, 76 ms and 190 ms. The hyperbolic secant adiabatic inversion with T_p = 870 μs, employed a slice selective magnetic field gradient of 11 G/cm. The carrier frequency range of the adiabatic inversion pulse was -34 and 34 kHz with respect to the central frequency to invert slice to select individual vials. To reduce the effect of gradient eddy currents on the CPMG measurement, trapezoidal gradients with 512 points at 1 μs intervals were employed. *FOV* = 80 mm; filter width = 125 kHz; 64 k-space points were acquired with a phase encoding time of t_p = 150 μs. The phase cycle for the hyperbolic secant pulse (slice selective pulse) and SPRITE RF pulses were $X\bar{X}Y\bar{Y}$ and for the receiver phase was $\bar{X}X\bar{Y}Y$.

The CPMG sequence parameters were: Echo time (2τ) = 1 ms, number of echoes = 1024, repetition delay = 2 s. 40 s were required for 8 signal averages. After ensuring the accuracy of adiabatic inversion CPMG, the measurement was undertaken on 7.5 cm water saturated Berea sandstone core plug with the same experimental parameters.

To test adiabatic inversion dhk SPRITE for zoom imaging with 1D SPRITE axial profiling, the Maran DRX-HF (Oxford Instruments Ltd, Oxford, UK) 0.2 T permanent magnet was employed. A water saturated Berea sandstone core plug was employed as a test sample. Magnetization preparation and dhk SPRITE imaging sequence parameters were: Hyperbolic secant adiabatic inversion T_p = 500 μs, filter width = 125 kHz; 64 k-space points were acquired with a phase encoding time of t_p = 150 μs. The dhk SPRITE RF pulses were 2 μs (7.5^o flip angle) in duration with a repetition time of TR = 1.5 ms. Profile images were acquired in 1 min and 6s with 64 signal averages. The phase cycle for the hyperbolic secant pulse (slice selective pulse) and SPRITE RF pulses were $X\bar{X}Y\bar{Y}$ and for the receiver phase was $\bar{X}X\bar{Y}Y$. The slice selective magnetic field gradient strength was 7.3 G/cm. The time interval between slice selection and commencement of the dhk SPRITE sequence was chosen to be 500 μs.

The Unisort and Acciss processing packages developed in the IDL programming environment (ITT, Boulder, CO) by the UNB MRI Centre were employed for image reconstruction and display. The WinDXP program (Oxford Instruments, Oxford, UK) was employed for T_2 distributions determination. WinDXP is a windows-based software toolbox which allows distributed exponential fitting on data acquired using the RINMR Windows (Oxford Instruments, Oxford, UK) data acquisition software.

5.4 Results and discussion

Fig. 5-4a shows the hyperbolic secant pulse, designed according to the approach of Tesiram and Bendall [57], in complex form. The inversion profile of the pulse, calculated in a homebuilt Bloch equation simulation by Dr. Ben Newling, is shown in Fig. 5-4b. In accordance with [57], the minimum number of digitized time steps in the pulse shape was set to $1000T_p bw_{eff}/70$, which was 321 in this work.

Simulation was employed to optimize the inversion profile for the designed hyperbolic secant pulse (Fig. 5-4b). The inversion parameters l_0 and l_{bw} [57] were measured from the simulated inversion profile. As shown in Fig. 5-3b, the oscillation in the simulated profile is much less than the actual noise level in the experimental profiles (Figs. 5-4 and 5-5). l_0^{sim}, l_{bw}^{sim}, bw^{sim} and bw_{eff}^{sim} are shown in Fig. 5-4b, and are the inversion parameters that were measured in the simulated profile. Δl should be sufficient so the profile wobbles in the shoulder region lie above the l_{bw}^{sim} defining bw_{eff}^{sim} [57]. This is illustrated in the figure inset. The standard deviation in inversion number is equal to 0.002 for one half of bw_{eff}^{sim}, in the simulated inversion profile.

In Fig. 5-5, a 1D axial profile of the complete Berea sample is also shown. The sample was long, 22.5 cm, in comparison to the RF coil length of 10 cm. As shown in Fig. 5-5 the received signal is less than half of the full sample length. Because the sample is long, RF non-uniformity and magnetic field nonlinearity yield a non-ideal profile near the edge of the FOV. The decreased signal near the profile center is due to reduced local B_1 strength, when averaged over the sample diameter [61].

(a)

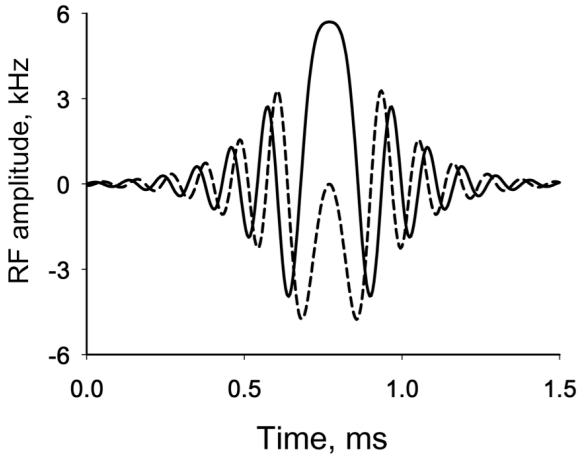

(b)

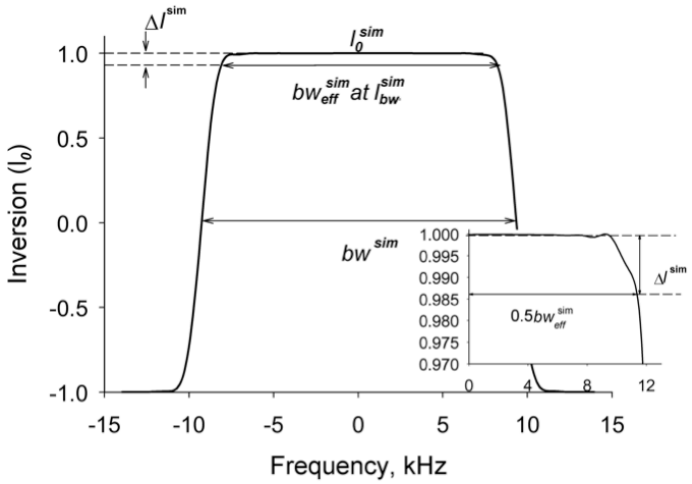

Figure 5-4 The hyperbolic secant adiabatic inversion selective pulse in complex form, the real (—) and imaginary (-----) parts of the RF pulse amplitude are shown. (b) The inverted slice for the HS pulse. A Bloch-equation simulation was employed to optimize inversion profile for hyperbolic secant pulse. I_0^{sim} , I_{bw}^{sim} , bw^{sim} **and** bw_{eff}^{sim} **are the values for inversion numbers, bandwidth and effective bandwidth are measured in the simulated inversion profile (**I_0^{sim} **= 0.9999,** I_{bw}^{sim} **=0.9877 and** ΔI^{sim}**= 0.012).** ΔI **should be sufficient so the profile wobbles in the shoulder region lie above the** I_{bw}^{sim} **defining** bw_{eff}^{sim} **[16]. This is illustrated in the figure inset.**

In Fig. 5-5 an axial profile of the inverted slice is shown. The hyperbolic secant pulse was applied to invert the spins in the ROI and the dhk SPRITE imaging method was employed to image the sample. In order to ensure that the RF pulse power was sufficient to completely invert the spins in the slice of interest, a free induction decay (FID) was measured in the presence of a gradient to calibrate the hyperbolic secant pulse. The pulse duration was selected to be 1 ms and the RF power was increased from 0.5% of the power required for a broadband 90° pulse to larger values up to the signal null point, at 50% of the power required for a 90° broadband pulse. The Fourier transform of the signal from the dhk SPRITE sequence was then considered and the pulse duration and RF power percentage were adjusted to optimize the slice profile [62].

The time-bandwidth product for a typical RF pulse is a constant, so the pulse duration can be changed to obtain a desired bandwidth. The hyperbolic secant pulse, 870 μs in duration with a 3 G/cm slice selective gradient, was employed to obtain the inverted profile in Fig. 5-5. A slice width of 3.1 cm was measured.

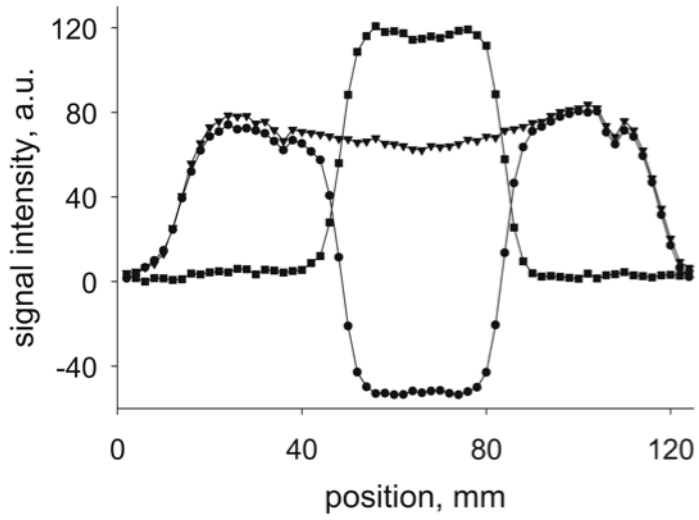

Figure 5-5 A 1D profile of the long Berea core produced by dhk SPRITE imaging (▼), The 1D profile with slab selection employing a spatially selective adiabatic inversion pulse (●) and the longitudinal profile of the ROI produced by subtracting the data (■).The image data are phase corrected and the real channel of the image for all three profiles has been displayed. The non-uniformity of slices is due to the effect of B_1 variation in excitation and detection in dhk SPRITE.

The difference of profiles shown in Fig. 5-5 yields an ROI only image with the signal from out-of-slice completely cancelled. In order to change the ROI width, the slice selective magnetic field gradient strength was changed three times to obtain three different slice widths, Fig. 5-6. The adiabatic inversion is essentially unaffected by B_1 inhomogeneity, but the dhk SPRITE profile of the inverted slice still shows the effects of B_1 variation in excitation and detection. The origin of this effect and its correction are the subject of [61].

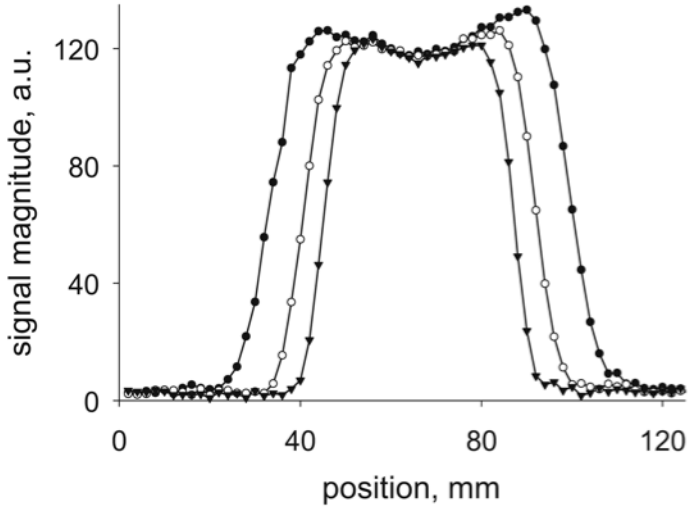

Figure 5-6 Longitudinal slice profiles for three slice widths. The pulse bandwidth was fixed and the slice selective gradient strength altered to change the slice width. For slice selective gradient strengths equal to 2.5 (▼), 2 (○) and 1.6 (●) G/cm, the slice widths were measured to be 3.7, 4.6 and 5.8 cm with the minimum slice width corresponding to the highest gradient strength. The non-uniformity of slices is due to the effect of B_1 variation in excitation and detection in dhk SPRITE.

To ensure that the conditions for the adiabatic fast passage in the inequality of Eq. (5.3) were satisfied, the values for $\gamma\vec{B}_{eff}$, $\Omega(t)$ and $2\pi/T_2$ can be compared. In the current experiment, the function $\Omega(t)$ has its maximum value of 12000 rad/s in the centre of the RF pulse and $\gamma\vec{B}_{eff}$ has a minimum value of 36000 rad/s at the centre. Hence, it is easily shown that the second part of the inequality in Eq. (5.3), the fundamental condition for adiabaticity, is completely satisfied. The ratio of the angular velocity of $\gamma\vec{B}_{eff}$ (in the middle of the pulse) to relaxation rate in the transverse plane ($\Omega_{centre}T_2/2\pi$) was 35 for the short T_2 component (18 ms), and 200 for the long T_2 component (108 ms) of the Berea sandstone. These values show the angular frequencies in the middle of the pulse are much

greater than the relaxation rates in the transverse plane. Hence, the condition for adiabatic fast passage is satisfied for our typical Berea sample. The condition is tested when $\vec{B}_{1\text{eff}}$ passes through the transverse plane, because it is here that the relaxation in the transverse plane will occur. The calculation shows that the adiabatic pulse will work well for samples with T_2 relaxation times longer than 18 ms. It can be predicted that the adiabatic pulse will still work well for $(\Omega_{\text{centre}}T_2/2\pi) > 5$. The ratio 5 corresponds to a minimum T_2 of 2.5 ms. We note that the T_2 of the Berea is a distribution and there will be low amplitude components shorter than 18 ms. The slice selection may be compromised for very short T_2 components of the distribution.

T_2 relaxation has an effect on the inversion percent in the slice of interest, but T_2^* will affect the inversion quality of the inverted slice edges. If the line-width (*lw*) for T_2^* is close to the radio frequency pulse *bw*, the inversion profile will be noticeably rounded because the frequency profiles will be convolved in the frequency domain with the lineshape. In our case T_2^*= 575 μs, which is a typical rock T_2^* value, the ratio *bw/lw* = 19.5 shows that the T_2^* effect on slice edges can be neglected. Good quality slice profiles will still result for *bw/lw* > 5. The ratio 5 corresponds to a minimum T_2^* of 150 μs.

The adiabatic inversion CPMG sequence was tested for slab selection accuracy employing three cylindrical vials of 1 cm diameter. The doped water in these vials had bulk T_2s of 16, 75 and 190 ms. Fig. 5-7a shows a 1D profile of the stack of vials, produced employing non-selective dhk SPRITE. Fig. 5-7b illustrates bulk CPMG measurements on the vials.

Applying a magnetic field gradient field of 12 G/cm and changing the carrier frequency for adiabatic inversion pulses from -34 to 34 kHz with respect to the central

frequency, individual slices were selected, Fig. 5-8a. Fig. 5-8b illustrates that adiabatic inversion CPMG measurements implemented at the selected positions yielded single exponential decays with T_2 values that agree very well with the reference values (T_{2a} = 16 ms, T_{2b}= 78 ms and T_{2c}= 187 ms). The subtraction of the bulk CPMG T_2 decay and the slice selective CPMG T_2 decay yields signal only from within the slice of interest. The amplitude is twice that of the original signal as observed for the profile measurements of Fig. 5-5. Hence the maximum amplitudes of the signal decays are all about two thirds of the bulk CPMG decay and show that the method is accurate and quantitative. The heights of 1D axial profiles in Fig. 5-8a are different due to their different T_1s.

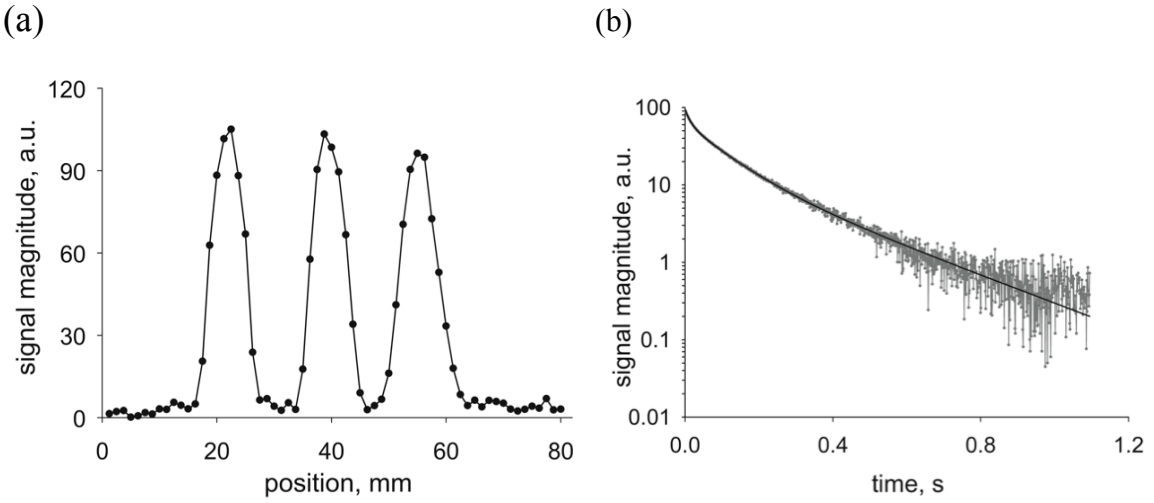

Figure 5-7 (a) A 1D profile of the stack of 1 cm diameter vials of water, produced employing non-selective dhk SPRITE. (b) A bulk CPMG decay from all three vials yields T_2s of 192, 75 and 15 ms.

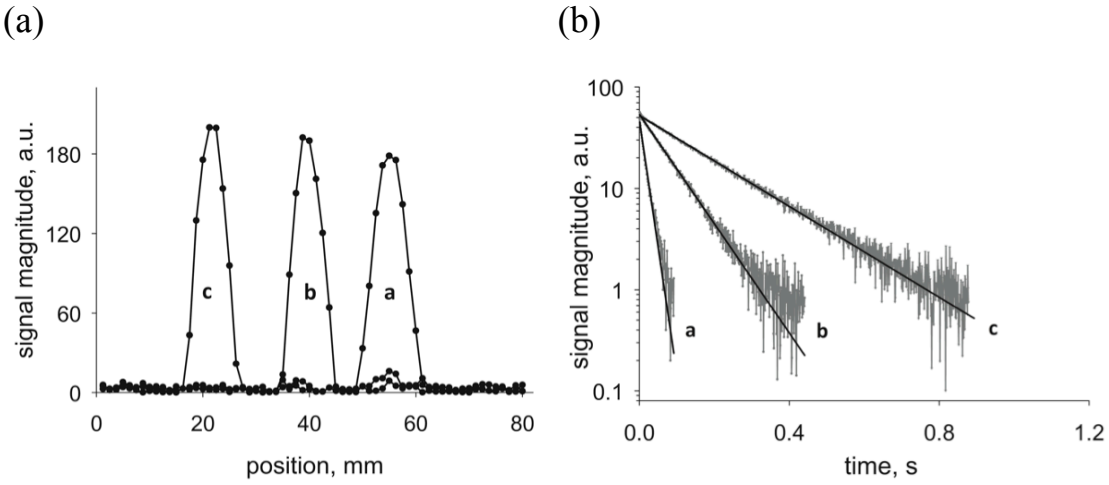

Figure 5-8 (a) Individual profiles selected by adiabatic inversion CPMG. Each vial is isolated by one of three scans. (b) Selective T_2 decays produced with adiabatic inversion CPMG and their single exponential best fits. T_{2a} = 16 ms, T_{2b} = 78 ms and T_{2c} = 187 ms. T_2 values agree very well with the reference values reported in Figure 5-6.

Adiabatic inversion CPMG was implemented on a water saturated Berea sandstone sample, in order to test our ability to measure T_2 distributions. Fig. 5-9 shows the T_2 distributions for the bulk CPMG T_2 measurement and adiabatic inversion CPMG T_2 measurements for three slices of the Berea sample. It is common practice in petrophysics to perform multi exponential fitting. Distributed exponential curve fitting results are consistent with discrete exponential fittings and with literature measurements on similar samples. Bulk CPMG and adiabatic inversion CPMG results are very similar. Selective T_2 measurements are able to measure T_2 components down to 1 ms. The ability of the sequence to cover almost the same T_2 range as bulk CPMG makes the sequence suitable for quantitative analysis. Current techniques for T_2 distribution mapping measure spatially resolved T_2s for the complete sample at image resolution. Adiabatic inversion CPMG is a non-imaging method for T_2 distribution mapping that is significantly faster than image-based methods. This method can be employed as an alternative to multi-echo MRI techniques when T_2 is to be measured at specific positions of the sample and resolution of about 1 cm is acceptable [46].

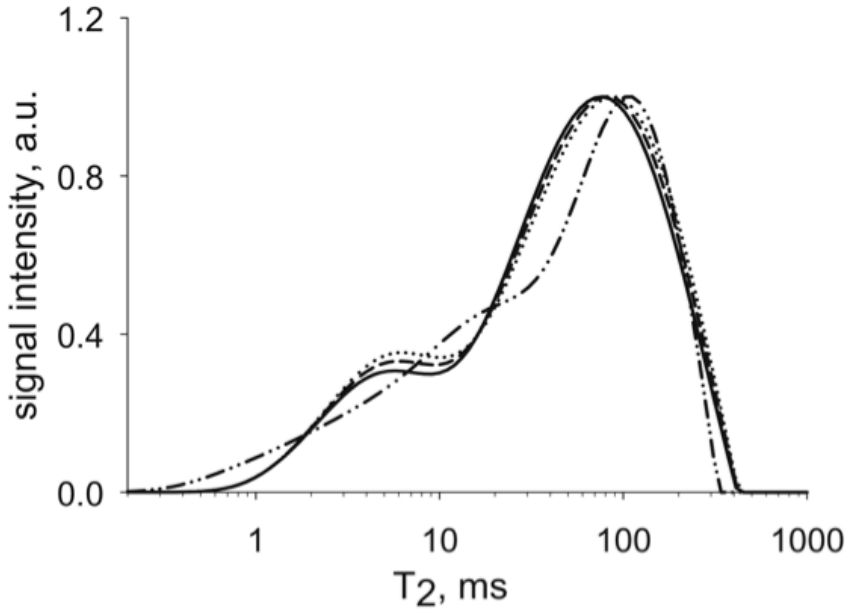

Figure 5-9 T_2 distributions for the bulk CPMG T_2 measurement (⎯ ··) and adiabatic inversion CPMG T_2 measurements for three slices of Berea sample 1 cm in thickness , a central slice placed at origin (⎯), a slice at + 2cm (- - -) and one at -2 cm (…). The slice T_2 distributions agree as expected and they are very close to the T_2 distribution from bulk CPMG.

Fig. 5-10a illustrates implementation of the subtraction method for a 75 mm Berea sample with a FOV of 93 mm to select a 30 mm long slab of interest. Fig. 5-10b illustrates the subtraction method for the same Berea sample but this time with the FOV = 60 mm, shorter than sample. Although there are significant artifacts in dhk SPRITE and adiabatic inversion profiles, they will not have any effect on the slab of interest produced after subtraction. The zoomed slab of interest is free from aliasing artifacts.

(a)

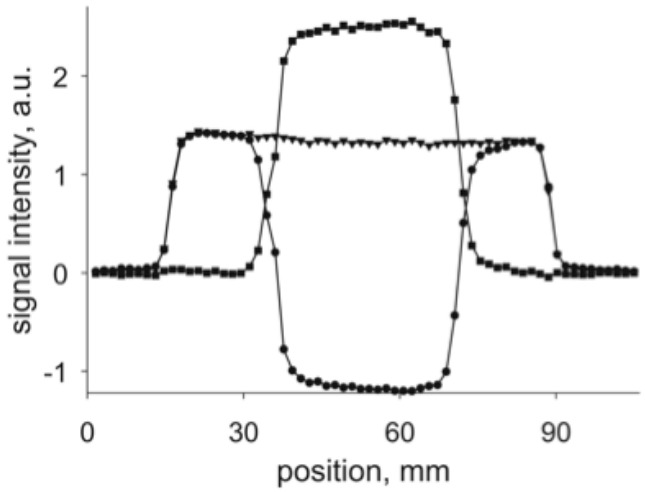

(b)

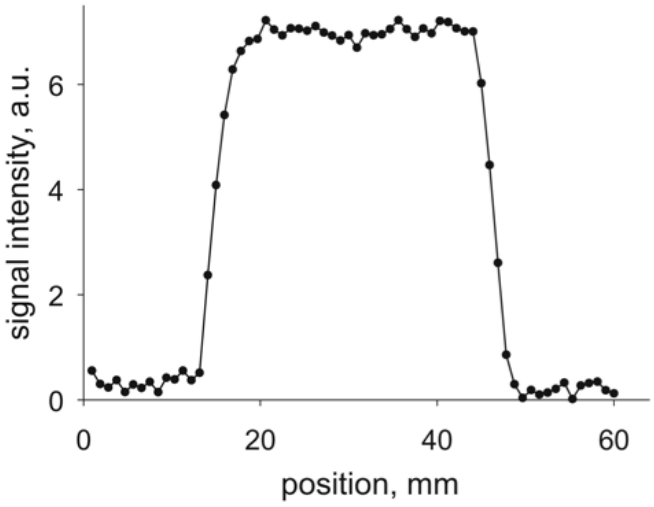

Figure 5-10 (a) A 1D profile of the long Berea core produced by dhk SPRITE imaging with FOV = 93 mm (●), the one dimensional profile with 30 mm slab selection employing a spatially selective adiabatic inversion pulse (▼) and the longitudinal profile of the ROI produced by subtracting the data (■). The image data are phase corrected and the real channel of the image for all three profiles has been displayed. (b) A 30 mm longitudinal profile of the ROI for the same sample but this time with a FOV of 60 mm, less than the sample length. The image data is phase corrected and the real channel of the image is shown.

5.5 Conclusion

The results demonstrate ROI selection within the FOV of long core samples by employing spatially selective adiabatic inversion pulses. This technique allows for reduced FOV, higher resolution imaging and localised relaxation time measurements. Adiabatic inversion pulses are immune to RF field inhomogeneities and, if the adiabatic fast passage conditions are satisfied, and the interval between inversion and imaging kept short ($< T_1$), spins in the ROI are inverted in a manner that avoids relaxation time contrast so as to maintain a density contrast in the final image. In addition, the dhk SPRITE method following the selection will yield naturally density weighted axial profiles of the sample and the inverted ROI. Although spatial encoding and excitation may be non-ideal near the edges of the FOV, subtraction of the inversion profile from the whole profile, yields an undistorted slice.

An alternative method to remove aliasing artefacts is phase-oversampling. Double the number of phase encoding steps, with half the gradient step size between k-space points, may be applied to double the field of view yet retain the same spatial resolution (with no aliasing). However, the most important outcome of the adiabatic inversion slice selection is local T_2 measurement, which is discussed in Chapter 6 in detail.

5.6 References

[1] O.V. Petrov, B.J. Balcom, Two-dimensional T_2 distribution mapping in porous solids with phase encode MRI, J. Magn. Reson. 212 (2011) 102-108.

[2] O.V. Petrov, G. Ersland, B.J. Balcom, T_2 distribution mapping profiles with phase encode MRI, J. Magn. Reson. 209 (2011) 39-46.

[3] Q. Chen, A.E. Marble, L. Romero-Zeron, B.J. Balcom, Flow imaging of fluids in porous media by magnetization prepared centric-scan SPRITE, J. Magn. Reson. 197 (2009) 1-8.

[4] Q. Chen and B.J. Balcom, Measurement of rock core capillary pressure curves using a single-speed centrifuge and one dimensional magnetic resonance imaging, J. Chem. Phys. 122 (2005) 214720.

[5] Y. Zhao, Y. Song, T. Wang, Y. Liu, L. Jiang, N. Zhu, W. Yang, Visualization of water flooding and subsequent supercritical CO_2 flooding in fractured porous media with permeability heterogeneity using MRI, Energy Procedia. 37 (2013) 6942-6949.

[6] J. Mitchell, J. Staniland, R. Chassagne, K. Mogensen, S. Frank, E.J. Fordham, Mapping oil saturation distribution in a limestone plug with low-field magnetic resonance, J. Pet. Sci. Technol. 108 (2013) 14-21.

[7] B.A. Baldwin, E.A. Spinler, In situ saturation development during spontaneous imbibition, J. Pet. Sci. Eng. 35(10) (2002) 23-32.

[8] J.L.A. William, G. Maddinelli, D.G. Taylor, Selective magnetic resonance imaging of chemicals in sandstone cores during flow, J. Magn. Reson. 109(1) (1994) 124-128.

[9] M. Halse, D.J. Goodyear, B. MacMillan, P. Szomolanyi, D. Matheson, B.J. Balcom, Centric scan SPRITE magnetic resonance imaging, J. Magn. Reson. 165 (2003) 219-229.

[10] M. Halse, J. Rioux, S. Romanzetti, J. Kaffanke, B. MacMillan, I. Mastikhin, N.J. Shah, E. Aubanel, B.J. Balcom, Centric scan SPRITE magnetic resonance imaging: optimization of SNR, resolution and relaxation time mapping, J. Magn. Reson. 169 (2004) 102-117.

[11] Q. Chen, M. Halse, B.J. Balcom, Centric scan SPRITE for spin density imaging of short relaxation time porous materials, Magn. Reson. Imaging. 23 (2005) 263-266.

[12] R.M. Heidemann, D. Ivanov, R. Trampel, F. Fasano, H. Meyer, J. Pfeuffer, R. Turner, Isotropic sub-millimeter fMRI in the human brain at 7 T: Combining reduced field of view imaging and partially parallel acquisitions, Magn. Reson. Med. 68 (2012) 1506-1516.

[13] M.E. Brummer, D. Moratal-Pe´rez, C. Hong, R.I. Pettigrew, J. Millet-Roig, W. Thomas Dixon, Nyquist: Reduced field of view imaging by direct fourier inversion, Magn. Reson. Med. 51 (2004) 331-342.

[14] L. Zhao, B. Madore, and L. P. Panych, Reduced Field-of-View MRI with two-dimensional spatially-selective RF excitation and UNFOLD, Magn. Reson. Med. 53 (2005) 1118-1125.

[15] T. Hussain, R.E. Clough, M. Cecelja, M. Makowski, S. Peel, P. Chowienczyk, T. Schaeffter, G. Greil, R. Botnar, Zoom imaging for rapid aortic vessel wall imaging and cardiovascular risk assessment, J. Magn. Reson. 34 (2011) 279-285.

[16] J. Yuan, Ch. Mei, B. Madore, N.J. McDonald, L.P. Panych, Fast fat-suppressed reduced field-of-view temperature mapping using 2D RF excitation pulses, J. Magn. Reson. 210 (2011) 38-43.

[17] S. Singh, B.K. Rutt, S. Napel, Projection presaturation. II. Single-shot localization of multiple regions of interest. J. Magn. Reson. 90 (1990) 313–329.

[18] D.C. Shungu, J.D. Glickson, Band-selective spin echoes for in vivo localized ^{1}H NMR spectroscopy. Magn. Reson. Med. 32 (1994) 277–284.

[19] S. Singh, B.K. Rutt, Henkelman RM. Projection presaturation: a fast and accurate technique for multidimensional spatial localization. J. Magn. Reson .87 (1990) 567–583.

[20] D. Kunz, Use of frequency-modulated radio frequency pulses in MR imaging experiments. Magn. Reson. Med. 3 (1986) 377–384.

[21] U. Klose, Space-selective saturation by frequency modulated pulses. In: Proc SMR, San Francisco, 1998, vol. 2. P 1059.

[22] A. Haase, Localization of unaffected spins in NMR imaging and spectroscopy (LOCUS spectroscopy), Magn. Reson. Med. 3 (1986) 963–969.

[23] D.D. Doddrell, G.J. Galloway, W.M. Brooks, J. M.Bulsing, J.C. Field, M.G. Irving, H. Baddeley, The utilization of two frequency-shifted sinc pulses for performing volume-selected in vivo NMR spectroscopy. Magn. Reson. Med. 3 (1986) 970–975.

[24] J. Rauschenberg, A.J. Krafft, F. Maier, P. Zamecnik, W. Semmler, M. Bock, Outer volume suppression in steady state sequences (OVSuSS) for percutaneous interventions, Magn. Reson. Med. 66 (2011) 123-134.

[25] T.B. Smith, K.S. Nayak, Reduced field of view MRI with rapid, B_1-robust outer volume suppression, J. Magn. Med. 67 (2012) 1316-1323.

[26] A.T. Hsu, W.W. Hunter, P. Schmalbrock , A.G. Marshall, Stored waveform inverse Fourier-Transform (SWIFT) excitation for water-suppressed whole-body slice-selected proton chemical shift spectra at 1.5 Tesla. J. Magn. Reson. 72 (1987) 75–88.

[27] E. Ozhinsky, D.B. Vigneron, S.J. Nelson, Improved spatial coverage for brain 3D PRESS MRSI by automatic placement of Outer-Volume Suppression Saturation Bands, J. Magn. Reson. Imaging. 33 (2011) 792-803.

[28] Y. Luo, R.A. de Graaf, L. DelaBarre, A. Tannús, M. Garwood, BISTRO: An outer-volume suppression method that tolerates RF Field inhomogeneity, Mag. Reson. Med. 45 (2001) 1095-1102.

[29] P. Le Roux, R.J. Gilles, G.C. McKinnon, P.G. Carlier, Optimized outer volume suppression for single-shot fast spin-echo cardiac imaging, J. Magn. Reson. Imaging. 8 (1998) 1022-1032.

[30] A. Chu, J.R. Alger, G.J. Moore, S. Posse, Proton echo-planar spectroscopic imaging with highly effective outer volume suppression using combined pre-saturation and spatially selective echo dephasing, Magn. Reson. Med. 49 (2003) 817-821.

[31] N. Amor, B. Blümich, Low-power MRI by Frank-sequence excitation, J. Magn. Reson. 211 (2011) 143-148.

[32] A. Henning, A. Fuchs, J.B. Murdoch, P. Boesiger, Slice-selective FID acquisition, localized by outer volume suppression (FIDLOVS) for (1)H-MRSI of the human brain at 7 T with minimal signal loss, NMR. Biome. 22(7) (2009) 683-696.

[33] J. Pauly, P. Le Roux, D. Nishimura, A. Macovski, Parameter relations for the Shinnar-Le Roux selective excitation pulse design algorithm [NMR imaging], IEEE. Trans. Med. Imaging. 10(1) (1991) 53-65.

[34] A. Henning, M. Schär, R.F. Schulte, B.Wilm, K.P. Pruessmann, P. Boesiger, SELOVS: Brain MRSI localization based on highly selective T_1 and B_1 insensitive outer-volume suppression at 3T, Magn. Reson. Med. 59 (2008) 40-51.

[35] G.A. Morns, R. Freeman, Selective excitation in fourier transform nuclear magnetic resonance, J. Magn. Reson. 29 (1978) 433-462.

[36] P.T. Callaghan, Principles of nuclear magnetic resonance microscopy, Clarendon press, Oxford, 1991.

[37] E. Fukushima, S.B.W. Roeder, Experimental pulse NMR: a nuts and bolts approach, Westview Press, USA, 1993.

[38] R. L. Kleinberg, S.A. Farooqui, M.A. Horsfield, $T1/T2$ ratio and frequency dependence of NMR relaxation in porous sedimentary rocks, J. Colloid. Interf. Sci. 158 (1993) 195-198.

[39] A. Tannús, M. Garwood, Adiabatic pulses, NMR. Biomed. 10 (1997) 423-243.

[40] R. Tycko, A. Pines, Spatial localization of NMR signals by narrowband inversion, J. Magn. Reson. 60 (1984) 156-160.

[41] R.J. Ordidge, P. Mansfield, Volume selection using gradients and selective pulses, Ann N Y Acad Sci, 508 (1987) 376-385.

[42] R.J. Ordidge, A. Connelly, J.A.B. Lohman, Image-Selected *in vivo* Spectroscopy (ISIS). A new technique for spatially selective NMR spectroscopy. J. Magn. Reson. 66 (1986) 283-294.

[43] A. Tintaru, F. Ziarelli, A. Thevand, B. Ancian, E-BURP-2 excitation in the CPMG sequence for improving reliability of relaxation data in the study of guest/host interactions in inclusion complexes in water, Chemical Physics Letters. 381 (2003) 458–463.

[44] R. Ishima, J. Baber, J.M. Louis, D.A. Torchia, Carbonyl carbon transverse relaxation dispersion measurements and ms–micros timescale motion in a protein hydrogen bond network, J. Biomol. NMR. 29 (2004) 187– 198.

[45] J.P. Loria, M. Rance, A.G. Palmer, A TROSY CPMG sequence for characterizing chemical exchange in large proteins, J. Biomol. NMR. 15 (1999) 151–155.

[46] O.V. Petrov, B.J. Balcom, Local T_2 distribution measurements with DANTE-Z slice selection, J. Magn. Reson. 215 (2012) 109-114.

[47] J. M. Warnking, G.B. Pike, Bandwidth-modulated adiabatic RF pulses for uniform selective saturation and inversion, Magn. Reson. Med. 52(5) (2004) 1190-1199.

[48] J. Shen, D.L. Rothman, Adiabatic slice-selective excitation for surface coils, J. Magn. Reson. 124(1) (1997) 72-79.

[49] D. Rosenfeld, S.L. Panfil, Y. Zur, Design of selective adiabatic inversion pulses using the adiabatic condition, J. Magn. Reson. 129 (1997) 115-124.

[50] D.G. Norris, Adiabatic radiofrequency pulse forms in biomedical nuclear magnetic resonance, Concept. Magnetic. Reson. 14(2) (2002) 89-101.

[51] M.A. Bernstein, K.F. King, X.J. Zhou, Handbook of MRI pulse sequences, Elsevier Academic Press, London, UK, 2004.

[52] Z. Starcuk, V. Mlynárik, M. Roden, J. Horký, E. Moser, Low-power water suppression by hyperbolic secant pulses with controlled offsets and delays (WASHCODE), J. Magn. Reson. 152 (1) (2001) 168-178.

[53] S. Conolley, D. Nishimura, A. Macovski, Sweep-Diagram Analysis of Selective Adiabatic Pulses, J. Magn. Reson. 83 (1989) 549-564.

[54] M. Garwood, L. DelaBarre, The return of the frequency sweep: Designing adiabatic pulses for contemporary NMR, J. Magn. Reson. 153 (2001) 155-177.

[55] E. Lunati, P. Cofrancesco, M. Villa, P. Marzola, A. Sbarbati, Evolution strategy optimization for adiabatic pulses in MRI, J. Magn. Reson. 138 (1999) 48-53.

[56] D.G. Norris, H. Lüdemann, D. Leibfritz, An analysis of the effects of short T_2 values on the hyperbolic-secant pulse, J. Magn. Reson. 92 (1991) 94-101.

[57] Y.A. Tesiram, M.R. Bendall, Universal equations for linear adiabatic pulses and characterization of partial adiabaticity, J. Magn. Reson, 156 (2002) 26-40.

[58] K. Deka, M.B. MacMillan, A.V. Ouriadov, I.V. Mastikhin, J.J. Young, P.M. Glover, G. R. Ziegler, B.J. Balcom, Quantitative density profiling with pure phase encoding and a dedicated 1D gradient, J. Magn. Reson. 178 (2006) 25-32

[59] P. Ghosh, D.H. Laidlaw, K.W. Fleischer, A.H. Barr, R.E. Jacobs, Pure-phase encoded MRI and classification of solids, IEEE. Trans. Med. Imaging. 14 (1995) 616-620.

[60] B.J. Balcom, R.P. Mac Gregor, S.D. Beyea, D.P. Green, R.L. Armstrong , T.W. Bremner, Single-point ramped imaging with T_1 Enhancement (SPRITE), J. Magn. Reson. 123 (1996) 131-134.

[61] S. Vashaee, B. Newling, B. MacMillan, B.J. Balcom, B_1 mapping with a pure phase encode approach: Quantitative density profiling, J. Magn. Reson. 232 (2013) 68-75.

[62] C. Coarna, B. Newling, Short, Shaped Pulses in a Large Magnetic Field Gradient, J. Magn. Reson. 196 (2009) 127-132.

Chapter 6 - A Comparison of Magnetic Resonance Methods for Spatially Resolved T_2 Distribution Measurements in Porous Media

The most important outcome of Chapter 5 was a local T_2 measurement employing adiabatic inversion pulses. In this chapter local T_2 measurement results produced by adiabatic inversion pulses are compared with two other classes of spatially resolved T_2 distribution measurement methods; Spin Echo Single Point Imaging (SE-SPI) and DANTE-Z CPMG.

This chapter is largely based on a paper "A Comparison of Magnetic Resonance Methods for Spatially Resolved T_2 Distribution Measurements in Porous Media" which is published in the journal Measurement Science and Technology. The format of references in this chapter follows that of the journal to which the paper will be submitted.

Abstract

Naturally occurring porous media are usually characterized by a distribution of pore sizes. If the material is fluid saturated, the ^1H magnetic resonance (MR) signal depends on the pore size, the surface relaxivity and the fluid itself. Measurement of the transverse relaxation time T_2 is a well-established technique to characterize material samples by means of MR. T_2 distribution measurements, including T_2 distribution mapping, are widely employed in clinical applications and in petroleum engineering. T_2 distribution measurements are the most basic measurement employed to determine the fluid-matrix properties in MR core analysis.

Three methods for T_2 distribution mapping, namely spin-echo SPI (SE-SPI), DANTE-Z CPMG and adiabatic inversion Carr-Purcell-Meiboom-Gill (CPMG) (see section 6.2) are compared in terms of spatial resolution, minimum observable T_2 and sensitivity. Bulk CPMG measurement is considered to be the gold standard for T_2 determination. Bulk measurement of uniform samples is compared to the three spatially resolved measurements.

SE-SPI is an imaging method, which measures spatially resolved T_2s in samples of interest. A variant is introduced in this work that employs pre-equalized magnetic field gradient waveforms and is therefore able to measure shorter T_2s than previously reported.

DANTE-Z CPMG and adiabatic inversion CPMG are faster, non-imaging, local T_2 distribution measurements. The DANTE-Z pulse train and adiabatic inversion pulse are compared in terms of T_1 or T_2 relaxation time effects during the RF pulse application, minimum pulse duration, requisite RF pulse power, and inversion profile quality. In addition to experimental comparisons, simulation results are presented.

6.1 Introduction

Magnetic resonance imaging **(**MRI) is well known for clinical diagnostic imaging but can be employed to image fluid saturation and fluid dynamics in porous media such as reservoir rock cores. Conventional magnetic resonance (MR) measurements of porous media are bulk measurements. Bulk Carr-Purcell-Meiboom-Gill (CPMG) measurement is considered to be the gold standard for T_2 determination. Many processes that occur in porous media are macroscopically inhomogeneous, or the sample may be macroscopically heterogeneous. Therefore, spatial resolution of the sample is necessary

for accurate measurement [1]. MR measures the ^{1}H signal from fluids within the pore space. It is a non-destructive method that can provide quantitative, spatially resolved data. These features make it an effective approach for analyzing rock cores and other porous media [2, 3].

T_2 distribution measurements, including T_2 distribution mapping, are employed in clinical applications and petroleum reservoir core analysis. They are the most basic measurements employed to determine the matrix/fluid properties in MR core analysis. It is highly desirable to develop T_2 mapping approaches that have a wide dynamic range of measurable T_2s for complete analysis of relaxation data.

A high signal to noise ratio (SNR) for the T_2 decay is also important, since low field MRI instruments are generally employed for relaxation measurements and low static field B_0 yields low sensitivity. Low B_0 field is often advantageous to limit micro and macro scale, susceptibility-driven field distortion.

An accurate interpretation of the T_2 distributions is complicated in porous media due to existence of different regimes of behavior (surface/diffusion-limited relaxation, diffusion in inhomogeneous fields, dependence of the apparent T_2 on the echo time of CPMG measurement) [4, 5]. When measurements are taken at low static magnetic field strength, the internal magnetic field gradient is small, and when a short echo time is employed, relaxation due to diffusion is negligible compared to relaxation due to surface relaxation [1].

Most methods for measuring spatially resolved T_2 (T_2 mapping) employ multiple-echo methods with frequency encode magnetic field gradients [6]. A multi-echo back-projection imaging method has been proposed to generate T_2 maps. A one-dimensional

pulsed gradient version of the multi-echo imaging measurement has been demonstrated [7]. The multi-slice multi-echo method [8] offers a more sophisticated but less quantitative method of obtaining relaxation time maps. Relaxation time mapping can be appended to any fast imaging method by pre-conditioning RF pulses [9, 10]. Frequency encode MRI methods for T_2 mapping may suffer from image artifacts and difficulty in observing and quantifying short T_2 lifetime species.

Imaging methods for T_2 distribution mapping based on MRI with phase encoding, for example spin echo single point imaging (SE-SPI), have been introduced [11, 12]. While robust and quantitative, conventional SE-SPI suffers from minimum measurable T_2 values of approximately 2 ms [11]. These drawbacks are significant when measuring reservoir rock cores with very short T_2 signal lifetime components. This paper shows the minimum T_2 measurement problem may be diminished by employing pre-equalized magnetic field gradients with SE-SPI [13].

Slice selective CPMG measurements for rock cores have recently been developed [14, 15] to yield spatially resolved, but non-imaging, T_2 distribution measurements. T_2 is measured within a discrete slice and the slice can be displaced to measure T_2 at different locations in the sample. A DANTE-Z pulse train scheme [15, 16] or a hyperbolic secant (HS) adiabatic inversion pulse [17, 18] can be employed [14, 15].

The magnetization selected by the DANTE-Z pulse train and the adiabatic inversion pulse lies along the *z* axis (longitudinal axis), and is thus affected only by T_1 relaxation during the waiting period for eddy current dissipation after switching off the slice select gradient. This is advantageous for short T_2 samples with $T_1 > T_2$ (the inequality typical for fluid saturated rocks) [14, 15]. Furthermore, the DANTE-Z pulse

train and the adiabatic inversion pulse do not create phase problems when combined with other MR measurements (for example CPMG). Phase dispersion occurs for selective excitation of transverse magnetization with a traditional sinc pulse. The DANTE-Z and the adiabatic inversion pulse do not require a refocusing gradient lobe for the slice selection gradient thus enabling an earlier start to the acquisition.

Slice selective CPMG methods are advantageous when T_2 needs to be measured in only a few representative positions in the sample. When the sample of interest has a well-defined large-scale structure, this approach has clear merit. [14, 15].

Herein, three MR techniques intended to measure spatially resolved T_2 distributions are compared. SE-SPI, DANTE-Z CPMG and adiabatic inversion CPMG are compared in terms of spatial resolution, minimum observable T_2, and sensitivity.

The performance of slice selective CPMG depends on the selective pulse performance. Therefore, the DANTE-Z pulse train and the adiabatic inversion pulse are compared in terms of T_1 or T_2 relaxation time effects during the RF pulse application, minimum pulse duration, requisite RF pulse power, and inversion profile quality. Simulation results are also presented.

6.2 Materials and methods

6.2.1 SE-SPI measurements

The SE-SPI method is illustrated in Fig. 6-1. Transverse magnetization is phase encoded during the first pulse interval τ_0. XY-16 phase cycling [19] is applied to preserve transverse magnetization components during the CPMG echo train. Eq. (6.1) gives the

transverse magnetization after the *n*th echo. The signal observed from each echo is directly proportional to the transverse magnetization.

$$M_{xy} = M_0 \, e^{-\frac{2\tau_0}{T_2}} \, e^{-\frac{(n-1)2\tau}{T_2}} \qquad \textbf{(6.1)}$$

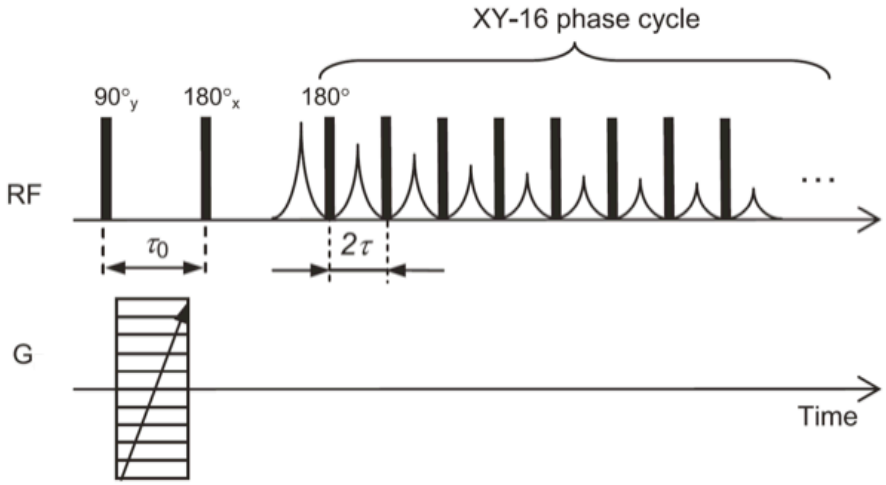

Figure 6-1 T_2 mapping spin echo single point imaging (SE-SPI) method. Transverse magnetization is phase encoded during the first pulse interval and then read out through multiple refocusing. To preserve the imposed phase shift upon refocusing, a XY-16 phase cycle is employed.

T_2 is the spin-spin relaxation time constant, M_0 is the initial magnetization and 2τ is the refocusing period between 180° pulses. The first echo $2\tau_0$ is longer than 2τ due to the application of the phase encode magnetic field gradients. Fourier transformation (FT) of the spatially resolved echoes generates a series of T_2-weighted profiles. At every pixel a CPMG T_2 decay is produced. Inverse Laplace Transform (ILT) of the decay results in

generation of a T_2 distribution at every pixel [11]. This method can yield poor SNR per unit time especially for samples with a long T_1 signal lifetime. Previous work [11, 15] showed that SE-SPI has a minimum measurable T_2 of approximately 2 ms. This limitation stems from the need for pulsed phase encode magnetic field gradients between the 90° pulse and the first 180° pulse. A relatively long τ_0, to allow eddy currents to dissipate, prevents measurement of short T_2 signal lifetime components.

6.2.2 DANTE-Z CPMG

The DANTE-Z selective inversion pulse scheme consists of a train of short, strong RF pulses, N', each with flip angle $\theta \ll \pi$, spaced τ_D apart. Only resonances that are offset from the transmitter by $\Delta\nu = N/\tau_D$ Hz, where N is an integer, are significantly affected by the pulse train [14, 20-24]. The transmitter frequency ν_0 and $1/\tau_D$ may be selected to ensure only one sideband ($\nu_0 + 1/\tau$) falls within the region of interest (ROI).

The DANTE-Z CPMG method, Fig. 6-2 a [15], consists of two successive scans: during the first scan, the magnetization is inverted from *z* to *-z* inside a desired frequency band, while during the second scan, all magnetization is maintained along *z*. Subtracting the signals from those two scans leaves only signal from the selected frequency band. When the selected magnetization is along the *z*-axis, the magnetization will be principally affected by T_1 relaxation. In porous media T_1 is always longer than T_2 [25-27]. Therefore, DANTE-Z CPMG should be advantageous when the sample of interest is a fluid bearing porous medium. Eq. (6.2) gives the transverse magnetization after the n^{th} echo. Once more the signal amplitude of each echo is directly proportional to the transverse magnetization.

$$M_{xy} = M_{+T_p}(1 - 2e^{-\frac{t_{\text{interval}}}{T_1}})\, e^{-\frac{2n\tau}{T_2}} \qquad \textbf{(6.2)}$$

where M_{+Tp} is the selected *z* magnetization, including relaxation time effects, with a selective pulse duration of T_P. The time $t_{interval}$ is the delay after the slice selective pulse is turned off, before the first 90° pulse. During this interval the ramped slice selection gradient acts like a spoiling gradient. $2n\tau$ is the total duration of the CPMG measurement. T_1 is the spin-lattice relaxation constant. Relaxation during the pulsed excitation, interval T_p, is complicated since it occurs during RF irradiation. M_{+Tp} is not readily determined analytically. We employed numerical simulations to investigate the effects of T_1 and T_2 during selective pulse excitation.

6.2.3 Adiabatic inversion CPMG

As described in Chapter 5, adiabatic pulses are amplitude and frequency modulated pulses [28-32]. The MR signal is excited by sweeping the effective magnetic field, $\mathbf{B_{eff}}$, adiabatically so the magnetization vector **M** remains approximately collinear with $\mathbf{B_{eff}}$. One important benefit of adiabatic pulses is the ability to excite over a broad range of resonant frequencies with a high degree of tolerance to RF field non-uniformity. The adiabatic rotation should be performed rapidly relative to relaxation times T_1 and T_2.

As was shown in Chapter 5, adiabatic inversion CPMG, Fig. 6-2b [14], consists of two successive scans: during the first scan, the magnetization is inverted from *z* to *-z* inside a desired frequency band, while during the second scan, all magnetization is maintained along z. Subtracting the signals from those two scans leaves only the selected frequency band. In this sense it is conceptually similar to the DANTE-Z method. When

the selected magnetization is along the *z*-axis, the magnetization will be principally affected by T_1 relaxation. Therefore, once again adiabatic inversion CPMG is predicted to be advantageous when the sample of interest is a fluid bearing porous medium ($T_1 > T_2$) [25-27].

As with the DANTE-Z method, Eq. (6.2) gives the signal intensity after the nth echo. Numerical simulation of the Bloch equations was employed to observe effects of T_1 and T_2 during T_p.

(a)

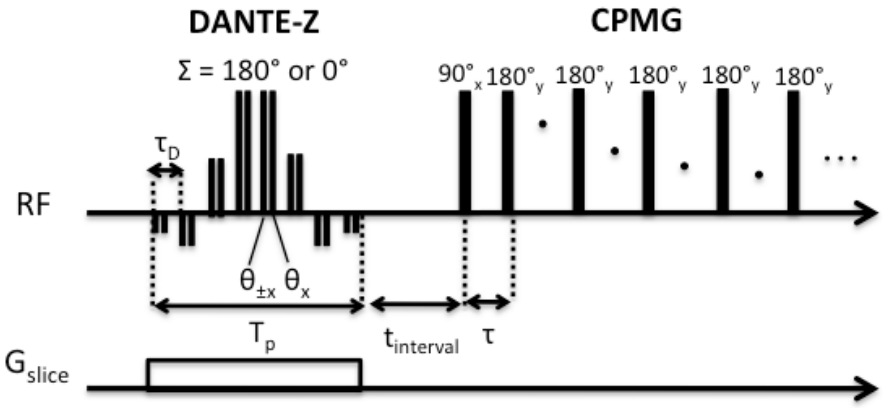

(b)

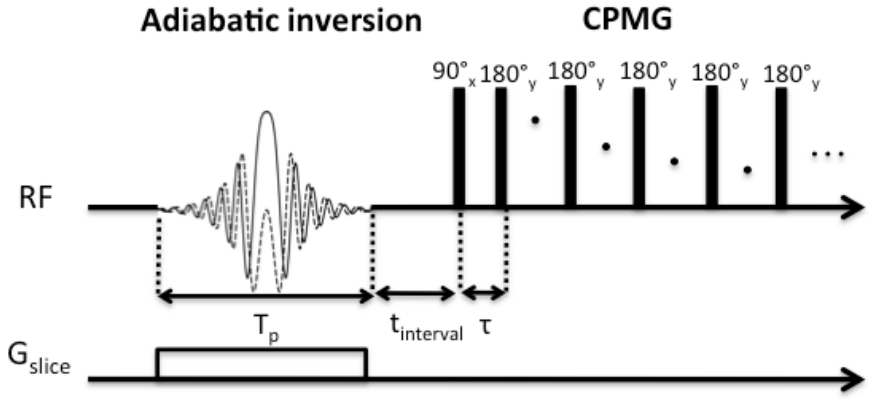

Figure 6-2 (a) DANTE-Z CPMG method. During the first scan, θ pulses in all pairs have the same phase providing a cumulative angle of 180° for the selected frequencies. During the second scan, the θ pulses in each pair are in anti-phase yielding a total flip angle of zero. The acquired signal is the difference between the two scans. (b) Adiabatic inversion in the presence of a slice selective magnetic field gradient followed by CPMG measurement. 2τ is the interval between the 90° pulse and the first echo. T_p is the overall inversion pulse duration. The time $t_{interval}$ is the delay after the slice selective pulse is turned off.

6.3 Experimental

6.3.1 Data processing

The Unisort and Acciss processing packages, developed in the Interactive Data Language (IDL) programming environment (ITT, Boulder, CO) by the UNB MRI Centre, were employed for image reconstruction and display. The WinDXP program (Oxford Instruments, Oxford, UK) was employed for T_2 distribution determination. WinDXP is a windows-based software toolbox, which allows distributed exponential fitting of data acquired using RINMR (Oxford Instruments, Oxford, UK) data acquisition software.

6.3.2 Equipment

All MRI measurements were performed on a Maran DRX-HF (Oxford Instruments Ltd, Oxford, UK) 0.2 T permanent magnet which is 8.5 MHz for ^{1}H. The RF probe was a custom-built solenoid, 4.4 cm inner diameter, driven by a 1 kW 3445 RF amplifier (TOMCO Technologies, Sydney, Australia). The 90° RF pulses were 11.4 μs with an RF power of 300 W. A shielded three axis gradient coil driven by Techron (Elkhart, IN) 7782 gradient amplifiers provided maximum magnetic field gradients of 26 G/cm, 24 G/cm and 33 G/cm in *x, y*, and *z*, respectively.

6.3.3 Bulk CPMG, SE-SPI and slice selective T_2 measurements of Berea core plugs

Measurements were undertaken on a Berea sandstone core plug (Kocurek, Industries, Caldwell, TX) Berea is a coarse grained, quasi-homogeneous sandstone. Physical properties of the Berea sample are reported in Table 6.1.

Table 6.1 Petrophysical properties of rock samples employed.

Sample	Berea sandstone	Synthetic rock core [c]	mortar	Wallace sandstone
T_2^* (μs)	746	57	730	337
T_1 (ms) [a]	200	5 (38%) 27 (62%)	1 (30%) 7 (70%)	10 (30%) 151 (70%)
T_2 (ms) [b]	25 (46%) 147 (54%)	2 (68%) 19 (32%)	0.8 (54%) 4 (46%)	6 (55%) 66 (45%)
Saturating fluid	2% brine	2% brine	Distilled water	2% brine
Length (cm)	5.0	5.3	4.5	5.0
Diameter (cm)	3.8	2.5	3.8	3.8

[a] T_1 recovery modeled as a bi-exponential processes
[b] T_2 modeled as a bi-exponential decay
[c] 5% Fe_2O_3 and 17% clay

Bulk CPMG, SE-SPI and selective CPMG measurement parameters are found in Table 6.2. The filter width = 125000 Hz and filter dead time = 26 μs, were chosen to be the same for all measurements. In SE-SPI the Field of View (FOV) was 8 cm with a maximum magnetic field gradient strength of 11 G/cm. Image spatial resolution was 1.25 mm with 64 pixels. In the SE-SPI measurements, composite 90° pulses and composite 180° pulses [33] and a XY-16 phase cycle [19] were employed to compensate for RF field inhomogeneity and to preserve magnetization phase while refocusing.

Table 6.2 Acquisition parameters for MR measurement of Berea sandstone for spatial resolution, minimum observable T_2, RF pulse power, and sensitivity comparison.

Parameters	Bulk CPMG	SE-SPI	DANTE-Z CPMG	Adiabatic inversion CPMG
Selective pulse duration (ms)	N/A	N/A	1.58	1.58
Selective pulse amplitude	N/A	N/A	50 %	20%
Slice selective magnetic field gradient strength (G/cm)	N/A	N/A	1	2
90° pulse duration (μs)	22.5	11.4	22.5	22.5
90° and 180° pulse amplitude	50%	100%	50%	50%
Echo time (μs), 2τ	600	600 [a]	600	600
Number of echoes	2048	2048	2048	2048
Number of echo points [b]	1	5	1	1
Number of averages	8	8	8	8
Repetition time (s)	2	1	2	2
Overall acquisition time (s)	16	2280	32	32
Resolution (mm)	N/A	1.25	5	5

[a] The first echo time was 602 μs
[b] Time domain data points acquired on each echo

Shaped magnetic field gradient pulses were designed with a recently developed pre-equalization technique [13, 34]. The impulse response of the magnet gradient system is measured and employed to design an input magnetic field gradient waveform, which produces a desired output. For the y gradient coil employed in this work, a pre-equalized magnetic field gradient waveform with a total duration of 8 ms was employed. The magnetic field gradient as experienced by the sample has a quasi-trapezoidal shape, 285 μs in duration, such that the gradient amplifier slew rate and bandwidth limitations (25 kHz) are not exceeded.

A DANTE-Z pulse train of duration 1.58 ms with 40 pulses and τ_D = 40 μs was employed. The slice thickness was varied by changing the slice selective magnetic field gradient strength. The slice position was changed by altering the carrier frequency of the excitation pulses. 50% RF amplitude and a slice selective magnetic field gradient of 1 G/cm were applied to select a 5 mm slice. The slice selective magnetic field gradient was not pre-equalized. Trapezoidal magnetic field gradients defined by 512 points at 1μs intervals were employed. The total duration of the slice selection approached 2 ms.

The adiabatic inversion with T_p = 1.58 ms and a slice selective magnetic field gradient pulse of 2 G/cm with 20% RF power was employed to select a 5 mm slice. As with the DANTE-Z method, the slice selective magnetic field gradient was not pre-equalized. Trapezoidal magnetic field gradients defined by 512 points at 1μs intervals were employed. The total duration of slice selection approached 2 ms.

The DANTE-Z pulse train and the adiabatic inversion pulse were employed as magnetization preparation before MRI measurement for visualization and adjustment of the slice of interest. A double half k-space (dhk) Single-Point Ramped Imaging with T_1 Enhancement (SPRITE) measurement was employed for this purpose [35].

6.3.4 Accuracy of slice selective CPMG methods

SE-SPI, DANTE-Z CPMG and adiabatic inversion CPMG with the above parameters were applied to a 2% brine saturated Berea sample from which water was partly removed by 1.5-h of centrifugation at 3500 r.p.m. Centrifugation is a common procedure in reservoir core analysis and introduces a spatially varying saturation. In this

way, one can produce a brine content distribution along a sample and measure T_2 as a function of the fluid content [6].

6.3.5 Bulk CPMG, SE-SPI and slice selective T_2 measurements of synthetic rock core, mortar, and Wallace sandstone

Measurements were carried out on a synthetic rock core (China University of Petroleum, Beijing), a mortar (McGill University, Montreal, QC) and a Wallace sandstone (Wallace Quarries Ltd., NS) to compare the ability of the above methods to measure short T_2 signal lifetime components. The physical properties of the above samples are reported in Table 6.1. Wallace sandstone was employed to observe the effect of a wide T_1 distribution on the minimum observable T_2. The synthetic rock and mortar had short T_2s.

The measurement parameters are reported in Table 3. The filter width = 125000 Hz and filter dead time = 26 μs were the same for all measurements. The FOV was 8 cm with a maximum magnetic field gradient strength of 11 G/cm. The DANTE-Z pulse train and the adiabatic inversion pulse were employed with the same parameters as for brine saturated Berea sandstone.

6.3.6 Bulk and adiabatic inversion CPMG of synthetic rock core, mortar, and Wallace sandstone

The adiabatic inversion pulse with a T_p of 1.58 and 0.3 ms, and a slice selective magnetic field gradient of 2 or 10 G/cm respectively, was employed to select a 5 mm slice. 20% and 80% RF amplitude were employed for the 1.58 and 0.3 ms RF pulse durations (Table 6.3). The slice selective magnetic field gradient was not pre-equalized.

Trapezoidal magnetic field gradients defined by 512 points at 1 μs intervals were employed for slice selection. The $t_{interval}$ delay, 512 μs, is necessary for eddy current dissipation between switching off the slice selective magnetic field gradient and the beginning of the CPMG pulse train. Including this delay, the total duration of slice selection approached 2 ms and 0.8 ms, respectively.

Table 6.3 Acquisition parameters for MR measurement of synthetic rock core plug, mortar, and Wallace sandstone for minimum observable T_2 comparison.

Parameters	Bulk CPMG	SE-SPI	DANTE -Z CPMG	Adiabatic inversion CPMG
Selective pulse duration (ms)	N/A	N/A	1.58	1.58, 0.3
Selective pulse amplitude	N/A	N/A	50 %	20%, 80%
Slice selective magnetic field gradient strength (G/cm)	N/A	N/A	1	2, 10
90° pulse duration (μs)	22.5	11.4	22.5	22.5
90° and 180° pulse amplitude	50%	100%	50%	50%
Echo time, 2τ (μs)	200	600 [a]	200	200
Number of echoes	2048	1024	2048	2048
Number of echo points [b]	1	5	1	1
Number of averages	8	8	8	8
Repetition time (s)	2	1	2	2
Overall acquisition time(s)	16	1140	32	32
Resolution (mm)	N/A	1.25	5	5

[a] The first echo time was 602 μs
[b] Time domain data points acquired on each echo

6.3.7 T_1 inversion recovery measurements

To perform T_1 distribution measurements, data sets employing inversion recovery measurement with variable inversion delay were acquired. Sixty-three delays were implemented for the Wallace sandstone sample. The minimum delay was 0.5 ms and the maximum delay was 980 ms with a bilinear spacing between these extremes (two intervals each with linear spacing). One interval was from 0.5 ms to 100 ms, while the other interval was from 100 ms to 980 ms.

For the synthetic rock and mortar twenty-eight inversion delays were employed. The minimum delay was 0.05 ms and the maximum delay was 60 ms with a bilinear spacing between these extremes. One interval was from 0.1 ms to 10 ms, while the other interval is 10 ms to 75 ms.

6.3.8 Numerical simulations of the DANTE-Z pulse train and the adiabatic inversion pulse

Numerical simulations were undertaken to investigate and compare the performance of the DANTE-Z pulse train and the adiabatic inversion pulse considering T_1 and T_2 relaxation time effects. The simulations were carried out employing a home-built Bloch equation simulation written by Dr. Ben Newling in the IDL programming environment ((ITT, Boulder, CO). The simulation applies a 3×3-rotation matrix for each digitized time increment during amplitude and phase modulated RF pulses.

6.4 Results and discussions

6.4.1 Spatial resolution, minimum observable T_2, and sensitivity comparisons

6.4.1.1 Spatial resolution and minimum observable T_2

Berea sandstone, which has a typical sandstone T_2 distribution, was imaged employing dhk SPRITE [35] as shown in Fig. 6-3. The sample was fully saturated and so the one-dimensional axial profile is uniform. Bulk CPMG was employed to measure the T_2 distribution for the fully saturated Berea sandstone sample. The bulk T_2 distribution was bimodal with peaks centered at 4 ms and 100 ms. The minimum observable T_2 was 0.6 ms as shown in Fig 6-4. Since the saturated Berea sandstone is uniform, it is reasonably anticipated that the bulk CPMG measurement will agree well with a spatially resolved measurement from a portion of the sample.

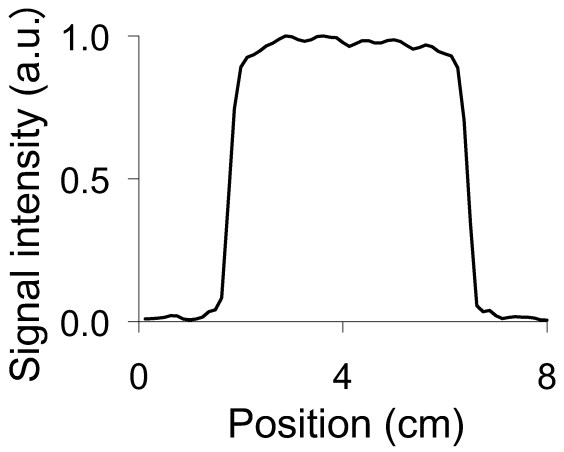

Figure 6-3 dhk SPRITE water content axial profiles of a 5 cm Berea sandstone core saturated with 2% brine. Water content in the profile is uniform as anticipated for a uniform sample.

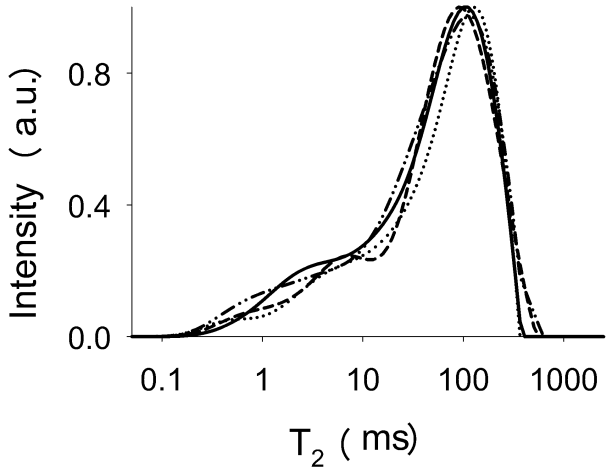

Figure 6-4 Results of bulk CPMG (—), SE-SPI (…), DANTE-Z CPMG (----) and adiabatic inversion CPMG (—..) of T_2 distribution for the SE-SPI and selective CPMG methods for the 2% brine saturated Berea sandstone which is shown in Fig 6-3; the T_2 distribution is displayed for the central pixel and the central slice, respectively. The plots show that all four methods measure signal lifetime components down to ~ 0.6 ms. 2τ = 600 μs was employed for all measurements.

With SE-SPI, the T_2 distribution was measured down the long axis of the sample with a 1.25 mm resolution. The T_2 decay curves of each pixel were spatially resolved and T_2 distributions produced by Inverse Laplace Transform. The T_2 distribution, measured from the decay of a central pixel, is displayed in Fig. 6-4 along with the bulk T_2 distribution. The SE-SPI experiment produces a T_2 distribution that agrees with the bulk CPMG measurement. The T_2 distribution plot for the above SE-SPI experiment suggests a minimum measurable T_2 of 0.6 ms. This is consistent with the magnetic field gradient pulse duration as experienced by the sample (285 μs) in the τ_0 interval of Fig. 6-1. Note that the magnetic field gradient pulse experienced by the sample is much shorter than the applied magnetic field gradient pulse of 8 ms [34].

The SE-SPI measurement presented here is a further development of T_2 mapping with pure phase-encode MRI. A recently developed pre-equalization method models the MRI system as linear and time invariant and employs an impulse response measurement to direct magnetic field gradient waveform design [13]. This is a considerable improvement compared to SE-SPI T_2 distribution measurements without employing pre-equalized magnetic field gradient waveforms. The application of pre-equalized magnetic field gradient waveforms has reduced the magnetic field gradient duration, as experienced by the sample, to 285 μs. Therefore, a reduction in $2\tau_0$ from 1.2 ms to 602 μs is possible; permitting the capture and characterization of shorter T_2 lifetime signal components that disclose more information regarding the composition of the porous media. This is particularly important since T_2 signal lifetimes of approximately 1 ms are common in petroleum reservoir core plugs.

For slice selective CPMG measurement, DANTE-Z and adiabatic inversion pulses with acquisition parameters reported in Table 6.1 were employed to measure T_2 for a slice, width 5 mm, from the fully saturated Berea positioned at the center of the sample. The T_2 distribution plots, Fig 6-4, show that both slice selective CPMG measurements can reproduce a minimum T_2 of 0.6 ms. The T_2 distributions are in good agreement with bulk CPMG and SE-SPI.

6.4.1.2 Sensitivity comparisons

The T_2 distributions are normalized in Fig. 6-4 to facilitate comparison. However, the sensitivities of bulk CPMG, SE-SPI and slice selective CPMG measurements are not the same.

The sensitivity is defined as $\frac{SNR}{\sqrt{t}}$, where SNR is the signal-to-noise ratio while t is the total measurement time. The sensitivities are reported in Table 6.4. For bulk and slice selective measurements the signal was measured as the maximum signal intensity of the CPMG decay. For SE-SPI the first T_2 weighted profile was chosen to measure the maximum signal intensity for the desired pixel. The noise was calculated as the standard deviation of the signal intensity after full decay of the CPMG data or one-dimensional T_2 weighted profile.

Note that the bulk CPMG, SE-SPI and slice selective CPMG measurements involve significantly different quantities of material. Slice selective CPMG methods measure the same quantity of material; a 5 mm slice of interest, which incorporates 10% of the material, from a 5 cm, saturated Berea sandstone. However, SE-SPI measures a pixel of interest (1.25 mm), which incorporates 2.5% of the material. To compare the sensitivity of the above measurements reliably, all the sensitivities were adjusted to equivalent quantities of material (Table 6.4). The sensitivities normalized by length, for adiabatic inversion CPMG, DANTE-Z CPMG and SE-SPI measurements were 1.7, 1.4 and 0.4 times that of the bulk CPMG measurement, respectively. It is striking that slice selective methods are more sensitive than bulk CPMG; this issue will be the subject of further investigation in future

The high sensitivity of selective CPMG measurement is beneficial, particularly in MRI measurements of reservoir core plugs that are naturally performed at low magnetic field with low instrument SNR. Assuming high spatial resolution is not required, as is

mostly the case in petrophysics (~ cm), T_2 distribution measurements with CPMG based methods are highly advantageous.

Table 6.4 Sensitivity comparisons for different T_2 mapping methods

Parameters	Bulk CPMG	SE-SPI	DANTE-Z CPMG	Adiabatic inversion CPMG
SNR	475	40	100	120
Overall acquisition time, t (s)	16	1140	32	32
Sensitivity, $\frac{SNR}{\sqrt{t}}$	118.7	1.2[a]	17.7[b]	21.2[b]
Sensitivity per mm[c]	2.4	0.95	3.4	4.2

[a] Sensitivity for one pixel
[b] Sensitivity for one slice
[c] Sensitivity was adjusted through normalization by sample length, slice width, or pixel size as appropriate

6.4.2 Accuracy of slice selective CPMG methods

For the purpose of demonstration, and to test the accuracy of the T_2 measurements and slice of interest, SE-SPI and slice selective CPMG measurements were applied to brine saturated Berea from which brine was partly removed by centrifugation.

The non-uniform one-dimensional axial profile in Fig. 6-5 is due to a variation in fluid saturation across the sample. The brine content is higher on the right side of the profile because fluid accumulates at the outlet end of the sample due to capillary pressure effects and the outlet boundary condition. Brine will be removed from large pore sizes due to capillary pressure effects, and the change in T_2 distribution results from desaturation of certain pore size ranges [12].

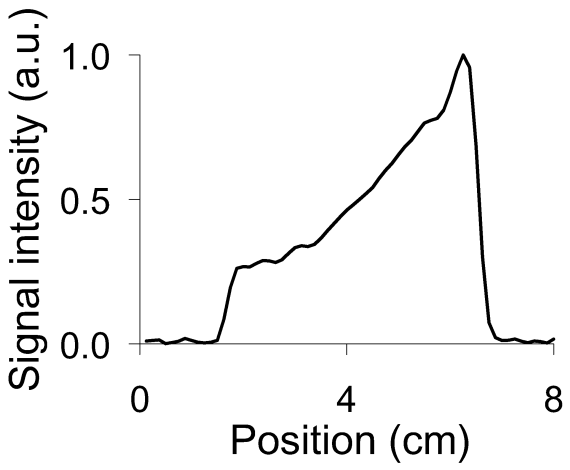

Figure 6-5 dhk SPRITE water content axial profiles of a 5 cm Berea sandstone core saturated with 2% brine recorded after 1.5 h centrifugation at 3500 r.p.m. Note the characteristic distribution of saturation after centrifugation.

Contour and waterfall plots of the T_2 distributions measured with SE-SPI at different positions along the partially desaturated Berea are shown in Figs. 6-6a and 6-6b. A shift of the T_2 distribution toward shorter lifetimes with reduced saturation is clear.

Contour and waterfall plots of the T_2 distributions were measured with DANTE-Z CPMG and adiabatic inversion CPMG at different positions (8 slices) along the desaturated sample are reported in Figs. 6-6c-f. The distance between the slice centers was chosen to be 6.5 mm. As the slices move from right to the left (fully to partially saturated) of the sample, the T_2 distribution shifts from longer T_2 components to shorter T_2 components. The two slice selective CPMG measurements yield almost identical T_2 distribution variations over the desaturated Berea sample, which are very similar to the SE-SPI results as shown in Figs. 6-6a and 6-6b.

For the above Berea sandstone with a typical sandstone T_2 distribution, as shown in Fig. 6-4, and employing 1.58 ms duration selective RF pulses, the T_2 distribution

measurement results are similar for bulk CPMG, SE-SPI, and slice selective CPMG methods. One may replace SE-SPI measurements by slice selective CPMG at the expense of losing high spatial resolution, but the T_2 distribution measurements will feature higher sensitivity. The multi-exponential fitting procedure is sensitive to SNR but a systematic study is beyond the scope of this thesis. The accuracy of slice selective CPMG measurements of short T_2 components may depend on the duration of the slice selective RF pulse and T_1 and T_2 distributions of the sample. These factors are considered in the appendix.

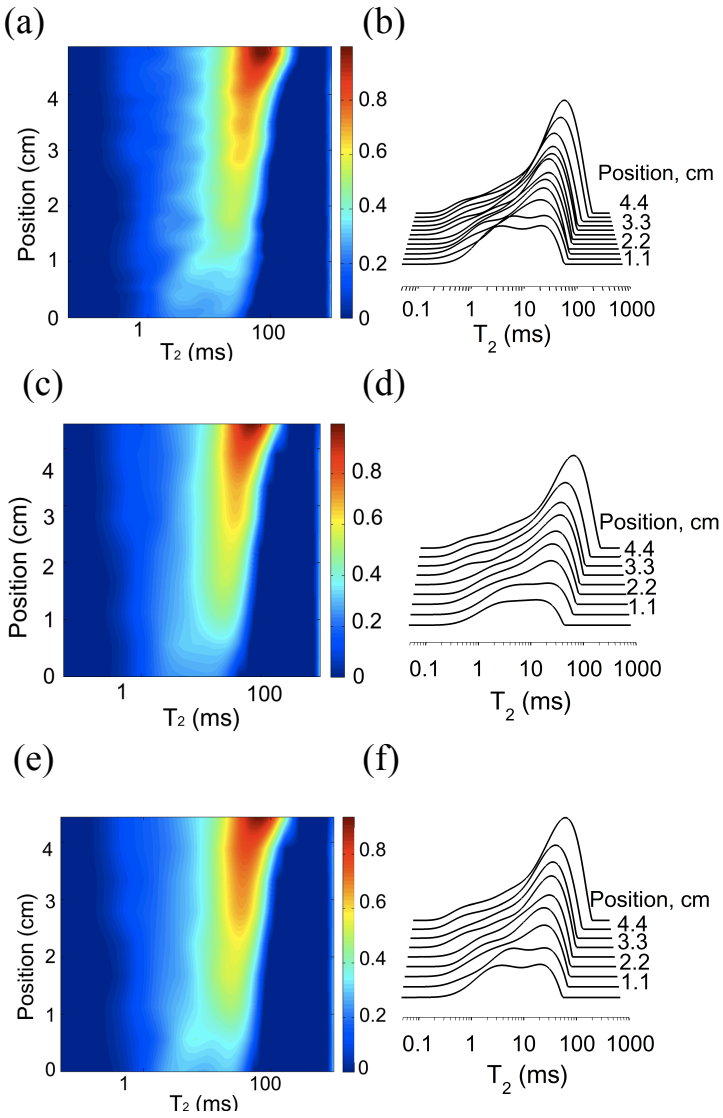

Figure 6-6 (a) Contour plot and (b) waterfall plot of the T_2 distributions measured with SE-SPI at different positions along the partly de-saturated Berea sandstone core. We have plotted the contour and waterfall plots from every fourth pixel. Plots (c), (d), (e), and (f) show contour and waterfall plots of the T_2 distributions measured with DANTE-Z CPMG and adiabatic inversion CPMG at different positions (8 slices) along the same sample. The 5 mm slice was displaced across the sample. The distance between the slice centers was 6.5 mm. The 2τ time was 600 μs.

6.4.3 Minimum observable T_2 comparisons

T_2 measurements were carried out on three additional samples – synthetic rock core, mortar and Wallace sandstone, each fully saturated with water. The T_2 distributions of the above samples are shown in Fig. 6-7. Bulk CPMG, SE-SPI and slice selective CPMG measurements were undertaken. For the SE-SPI and slice selective CPMG measurements, the T_2 distribution for a central pixel and a central slice were chosen for display, respectively. Water in the above samples exhibits a uniform T_2 relaxation over the sample; this makes the comparison of spatially resolved and bulk T_2 distributions valid.

The principal concern in this thesis is high quality measurements of the T_2 distribution of the pore fluid and access to short T_2s spatially resolved. The ILT approach imposes a smooth distribution that may not be physically correct in some instances. A single exponential decay processed by ILT will yield a symmetrical T_2 distribution in log space, with a width that is not physical. The T_2 distribution shape is not calibrated and not over-interpreted in this work. The interpretation is only based on changes in T_2 distributions (employing bulk CPMG as a control) rather than an absolute interpretation.

For all the above samples, the T_2 distributions, which are produced by SE-SPI (Figs. 6-7a-c), suffer from attenuation of short lifetime T_2 signal. As compared to bulk CPMG measurements, the T_2 distributions measured by SE-SPI miss T_2 components shorter than 0.6 ms. This is more evident for the mortar (Fig. 6-7b), where very short T_2 components contribute about 54% of the area under the distribution. Therefore the minimum observable T_2 for SE-SPI is longer than bulk CPMG measurement due to the difference in echo times.

Although DANTE-Z and adiabatic inversion CPMG measurements were performed employing the same echo time as bulk CPMG (200 μs), they still cannot measure T_2 components shorter than 1 ms for the above samples (Figs. 6-7a-c). In DANTE-Z and adiabatic inversion T_2 measurements (with 1.58 ms RF pulse duration), the area under the T_2 distribution curve has been reduced significantly for $T_2 < 1$ ms. This T_2 signal attenuation in slice selective measurements may be explained by T_1 lifetime effects in these samples. This hypothesis is investigated in the next section.

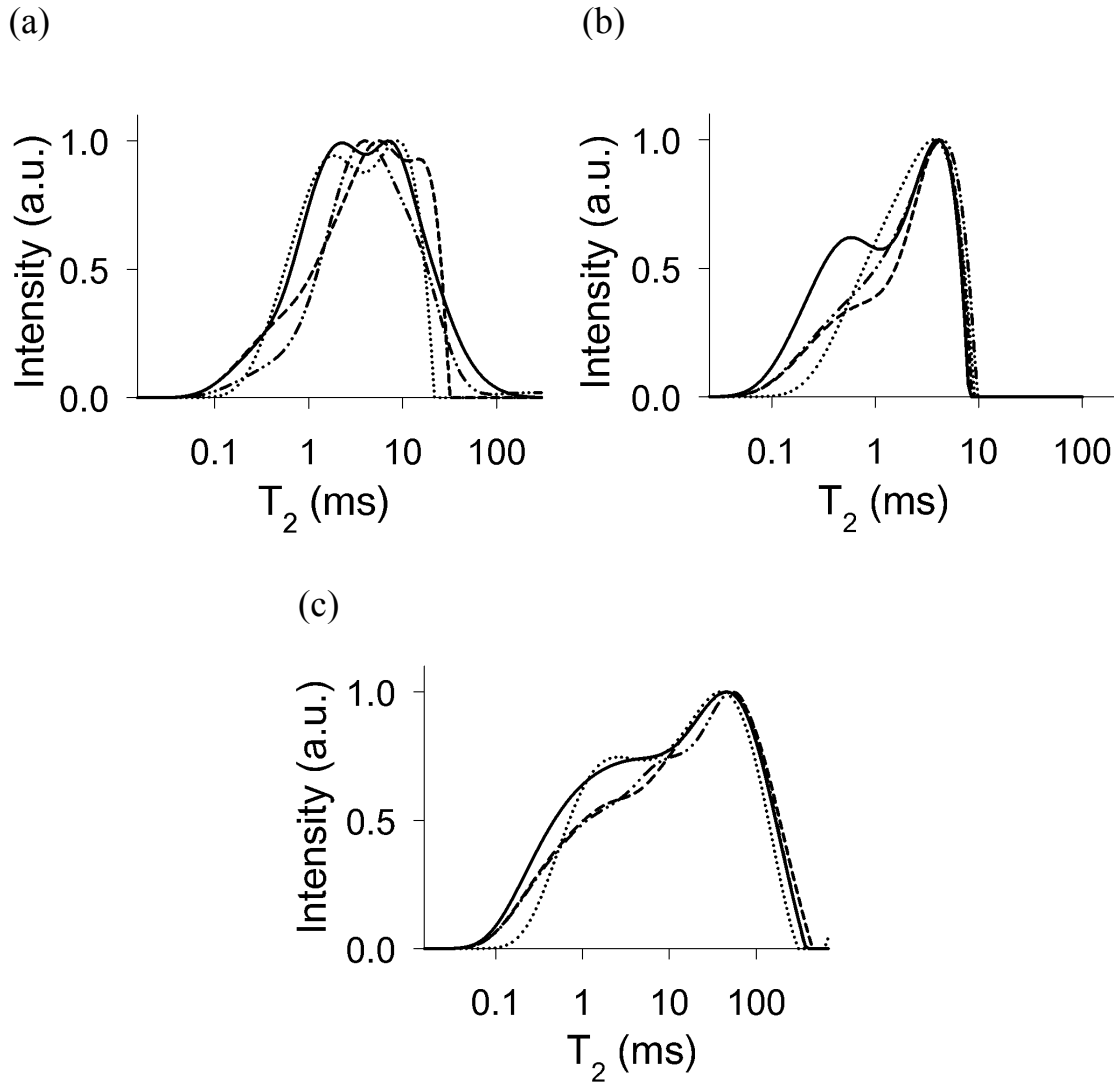

Figure 6-7 T_2 distributions measured from the water saturated (a) synthetic rock core, (b) mortar and (c) Wallace sandstone. The results were produced from bulk CPMG (—), SE-SPI (…), DANTE-Z CPMG (----) and adiabatic inversion CPMG (— ··). For SE-SPI and the selective CPMG measurements, the T_2 distribution displayed is for the central pixel and the central slice, respectively. Note that for the SE-SPI measurement 2τ was 600 µs rather than 200 µs. The T_2 distributions from slice selective CPMG methods employing the DANTE-Z pulse train (----) and the adiabatic inversion pulse (— ··) show considerable attenuation of short T_2 lifetime components, due to relaxation during T_p and $t_{interval}$.

T_1 distributions measured from the above samples employing an inversion recovery method are reported in Fig. 6-8. Detailed interpretation of peaks from ILT data may be challenging. However, one can be sure that peaks are real thanks to comparison of the peak values with the values in Table 6.1, which are results of fitting the decays to a bi-exponential model.

The fluid saturated synthetic rock core has a two-lobe T_1 distribution with a pronounced peak at $T_1 \approx 25$ ms. The shoulder at $T_1 \approx 5$ msretains considerable intensity. The water-saturated mortar has a narrow T_1 distribution, including shorter T_1 components. The pronounced T_1 peak is at $T_1 \approx 7$ ms, while the other peak is very short at $T_1 \approx 1$ ms. In Wallace sandstone, T_1 stretches over a wide interval from 1 ms to 1.5 s with substantial signal components at $T_1 \approx 200$ ms.

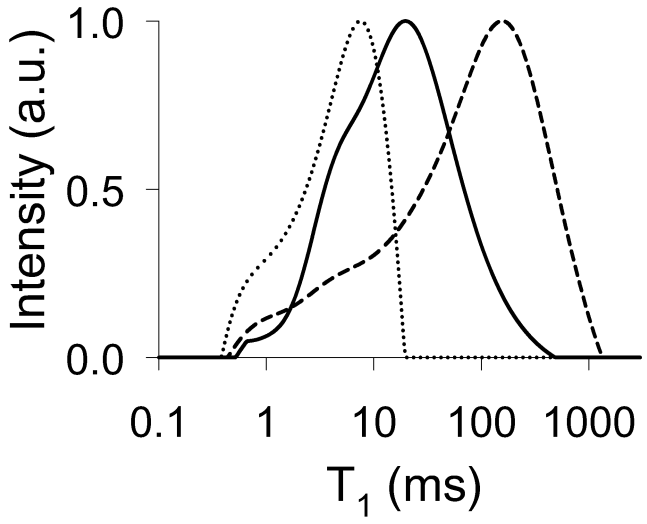

Figure 6-8 T_1 distributions measured from the saturated synthetic rock core (—), mortar (…) and Wallace sandstone (----) employing an inversion recovery measurement. The synthetic rock core and mortar include short lifetime T_1 components (T_1 = 5 ms and 1 ms, respectively).

For synthetic rock and mortar samples (Figs. 6-7a and 6-7b) where the short T_1 components (5 ms and 1 ms, respectively) contribute 38% and 30% of the T_1 distributions, respectively, the decrement in area under the T_2 distribution curves are more evident than Wallace sandstone (Fig. 6-7c). Wallace sandstone significantly has longer T_1 components than synthetic rock and mortar samples. The results may be explained by Eq. (6.2), which predicts signal loss due to the existence of short T_1 lifetime components. Short T_1 lifetime components will affect M_{xy} through the first and second terms in Eq. (6.2). Since T_1 scales with T_2 in porous media [15], T_1 relaxation during T_p and $t_{interval}$ (512 μs) will affect the observed T_2 distribution in slice selective measurements. During T_p and $t_{interval}$, signal from components with short T_1 are suppressed more than the signal components with long T_1. Suppression of the signal with short T_1 can have an adverse effect on the minimum observable T_2 as shown in Figs. 6-7a-c. One should consider T_2 relaxation during T_p as well, but T_1 effects are dominant in these samples.

6.4.4 Comparison of results for different adiabatic pulse durations

The results of Fig. 6-7 reveal that the ability of slice selective CPMG methods to observe short T_2 components will be impaired when the slice selective RF pulse duration is long in comparison to the sample's relaxation times. The shorter the RF pulse duration, the less relaxation will occur during the slice selection process. The T_2 distribution results, in this case, will therefore be of higher quality.

For the DANTE-Z pulse train, τ_D in Fig. 6-2a must be short enough to put the second excitation band (= $1/\tau_D$ Hz) outside the FOV. The pairs of θ pulses in Fig 6-2a

eliminate all but one sideband. This diminishes the problem of multiple selective excitations. τ_D should also be short to maintain the total DANTE pulse train short (since the pulse length scales with the τ_D delay). τ_D should however be long enough to permit a pair of pulses that can be as long as several μs each. Thus τ_D = 40 μs appears to be a reasonable compromise [4]. For a given τ_D, setting number of pulses equal to 40 produces a DANTE-Z pulse train of total duration of 1.58 ms.

However adiabatic pulses may be substantially shorter than 1.58 ms. An adiabatic pulse as short as 0.3 ms is experimentally possible. This is an advantage, specifically when adiabatic pulses are utilized to invert a slice in a sample with short relaxation times. An adiabatic inversion pulse with a duration of 0.3 ms will diminish relaxation time effects during selective excitation.

The T_2 distributions for synthetic rock core, mortar and Wallace sandstone were measured employing a 0.3 ms adiabatic inversion pulse. The T_2 distributions measured with bulk CPMG and the adiabatic inversion CPMG (T_p = 0.3 ms and 1.58 ms) methods are plotted in the same graph for each sample (Figs. 6-9a-c). For all three samples the adiabatic inversion CPMG T_2 measurement employing shorter pulse durations have significant improvement in measurement of short T_2 signal lifetime components. The improvement in the T_2 distributions is more evident for synthetic rock and mortar samples, where there is a greater contribution of short T_1 signal lifetimes in comparison with the Wallace sandstone (Fig. 6-8).

Employing a T_p of 0.3 ms has diminished the relaxation time effects during the slice selection in a large extent for the Wallace sample (Fig. 6-9c). Considering a simple bulk CPMG measurement as a control, there is small loss of short T_2 signal lifetimes due

to relaxation time effects during T_p and $t_{interval}$ for the synthetic rock and mortar samples (Figs. 6-9a and 6-9b). Once more, considering bulk CPMG measurement as a control, the T_2 signal enhancement for the shorter T_2 peak, 0.8 ms, (Fig. 6-9b) is incorrect and due to instabilities of ILT processing.

To eliminate the relaxation time effects during the experiment for samples including short lifetime T_1 components, one needs adiabatic inversion pulses with duration shorter than 0.3 ms. It is a challenge to design adiabatic pulses shorter than 0.3 ms under adiabatic condition [32]. However, one may employ pre-equalized magnetic field gradients, as employed for SE-SPI, to reduce $t_{interval}$ from 512 μs to a shorter time (~100 μs).

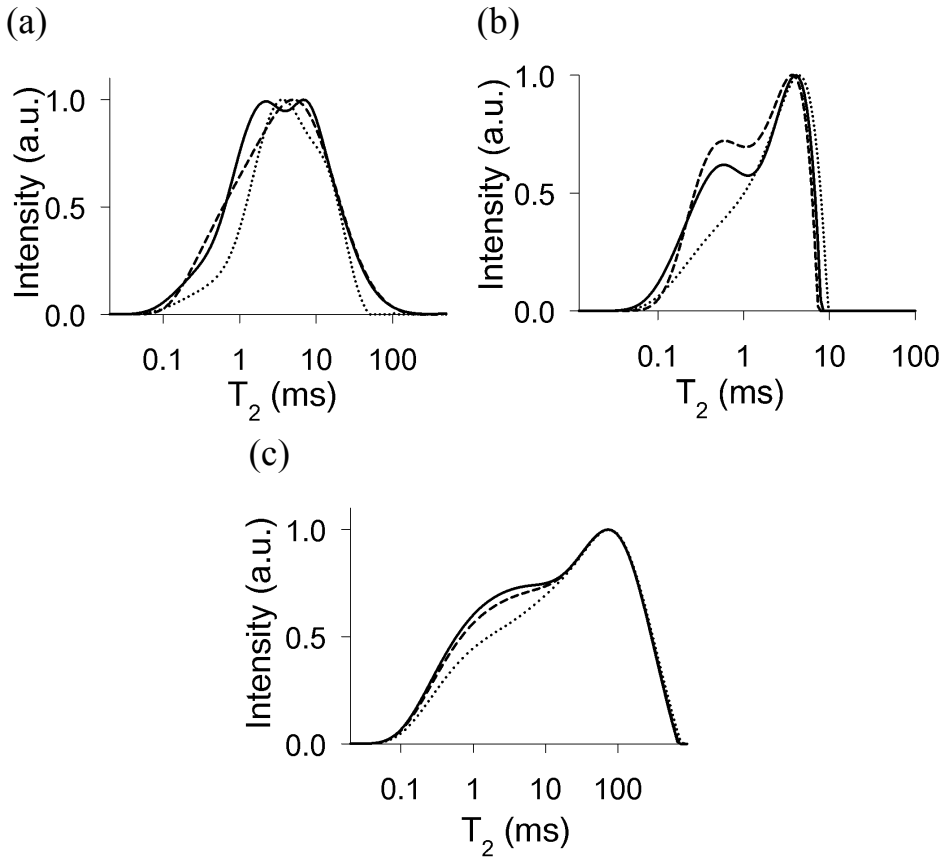

Figure 6-9 T_2 distributions for (a) synthetic rock core, (b) mortar and (c) Wallace sandstone. Adiabatic inversion CPMG measurements were employed to produce distribution. In each figure (—) shows the T_2 distribution for the bulk CPMG measurement. (…) shows the T_2 distribution when the adiabatic inversion HS pulse duration was 1.58 ms. In each figure (----) illustrates the T_2 distributions for the same sample but with application of a shorter adiabatic inversion pulse, 0.3 ms. A T_p of 0.3 ms has diminished the relaxation time effects during the slice selection. The T_2 signal enhancement in (b) for ($T_2 > 0.1$) is due to instabilities of ILT processin.

The DANTE-Z pulse train may be inconvenient in terms of the excitation bandwidth. A smaller number of pulses (N') enlarge the selected bandwidth (~1/N'). Too large a bandwidth requires a stronger magnetic field gradient than advisable considering hardware limitations, for a given slice thickness. The inversion bandwidth of the DANTE-Z pulse is inversely proportional to the DANTE-Z pulse interval ($1/N'\tau_D$). In

adiabatic inversion pulses design, T_p and bandwidth are independent. Every combination of T_p and bw_{eff} (effective bandwidth) are valid, but the condition $T_p bw_{eff} > 3$, corresponding to adiabatic limit, must be considered. One can have a very short adiabatic inversion pulse (~ 0.3 ms) and reasonable bandwidth (~ 10 kHz) at the same time. In addition, when the RF pulse bandwidth is narrower, reduced magnetic field gradient strength is needed to localize the slice of interest.

Note that an alternative for the slice selective CPMG methods may be SE-SPI with a lower spatial resolution. In SE-SPI the resolution can be decreased by decreasing the number of phase encode gradient steps. For a typical FOV of 8 cm and typical sample length of 5 cm, the image resolution is 1.25 mm for 64 phase encode gradient steps. One can achieve a resolution of 5 mm by employing 16 phase encode gradient steps. The measurement time will be decreased from 1140 s (Table 6.4) to 285 s, but this is still longer than the measurement times needed for slice selective CPMG methods (32 s) and hence less sensitive.

The main drawback of low resolution SE-SPI is that the pixel shape degrades. The degradation is due to the convolution effects of k-space sampling. In addition, SE-SPI measurement will always produce contiguous slices. It is not possible to select nonadjacent slices at different positions in the sample.

6.4.5. The internal magnetic field and core plug linewidth versus slice selective RF pulse bandwidth

When fluid saturated porous media are subjected to a static magnetic field, an internal magnetic field, inside the pore space, is induced due to magnetic susceptibility

differences between the pore-filling fluid and the solid matrix [36]. The internal magnetic fields increase the linewidth, which may interfere with slice selection bandwidth.

The slice selective pulse excites a range of frequencies. For example, the adiabatic inversion pulse (Fig. 6-10b, Appendix) has an effective frequency bandwidth of 4250 Hz. While the local internal magnetic field gradients may be significant, they are local to the pore space. Therefore the absolute range of frequencies introduced is minor.

It has been shown in the literature [36] that linewidth scales linearly with the static magnetic field strength. An expression for $\Delta\upsilon$, the linewidth, was proposed where $\Delta\upsilon = \frac{\gamma \Delta B^{i}}{2\pi} = C\Delta\chi f_0$, with ΔB^{i} the breadth of the magnetic field distribution due to susceptibility contrast ($\Delta\chi$) in the fluid saturated rock. C is a dimensionless constant and f_0 is the Larmor frequency. The linewidth related to the internal magnetic field has been measured for a typical fluid saturated Berea sandstone, at a variety of static magnetic field strengths and the best fit of the plot $\Delta\upsilon$ versus $\Delta\chi f_0$ determined [36]. The best fit line had a slope C of 0.26. Knowledge of the susceptibility difference ($\Delta\chi = \chi_{\mathrm{Berea}} - \chi_{\mathrm{water}} = 98.85 \times 10^{-6}$) and Larmor frequency ($f_0 = 8.5 \times 10^{6}\ Hz$) yields a linewidth of 218 Hz. This is less than 5%, the selective pulse bandwidth (4250 Hz). Convolution of the linewidth with the slice selective RF pulse bandwidth may cause blurring of the slices edges, but would not have adverse effects over the selected slice.

The above discussion however does suggest that it would in general be advantageous to employ stronger slice selection gradients and selective RF pulses with a greater bandwidth for slice selection.

Furthermore, we have directly imaged the selected slices and know that the slice quality is good. If there were any significant problems related to the internal magnetic field gradients, we would observe slices with poor definition. The above problems are all ameliorated by working at 8 MHz, relatively low frequency, for rock core analysis. The situation may be different at higher frequencies.

6.5 Conclusion

A comparison of SE-SPI and slice selective CPMG measurements was undertaken for porous media samples

. The T_2 measurements suggest slice selective CPMG methods as an alternative for SE-SPI when T_2 need only be measured at particular positions within the sample and high resolution is not required. Slice selective CPMG measurements are much more sensitive than SE-SPI. The slice selective CPMG methods will be very beneficial, particularly for MR of porous media at low field. The magnetic field gradient strength and shape are critical for short echo time SE-SPI but are not critical for DANTE-Z CPMG and adiabatic inversion CPMG methods.

For slice selective CPMG methods, two inversion schemes, a DANTE-Z pulse train and an adiabatic inversion pulse were tested. The adiabatic inversion pulse may be applied in as short a time as 0.3 ms, which is very beneficial when measuring the T_2 distribution for samples including short lifetime T_1 and T_2 components (< 5 ms).

Our conclusion is that adiabatic inversion followed by a CPMG pulse train is the preferred way to measure local T_2 distributions provided a regional measurement of coarse spatial resolution is sufficient. The adiabatic inversion CPMG method is

straightforward; the most challenging aspect of the method is the calibration of the adiabatic inversion pulse, which is described in the literature [14].

6.6 Appendix: Numerical simulations of the DANTE-Z pulse train and adiabatic inversion pulse

The DANTE-Z pulse train and the hyperbolic secant (HS) adiabatic inversion pulses employed are compared through simulation. As discussed in section 2, relaxation takes place during pulse irradiation. Bloch equation simulation is applied to investigate the effects of T_1 and T_2 during T_p. At each discretized time step Δt of T_p, magnetization components perpendicular to the polarizing magnetic field, M⊥, decrease by $\Delta M_{\perp} = \frac{M_{\perp}\Delta t}{T_2}$, and the magnetization parallel to the polarizing field, M_z, changes by $\Delta M_z = \frac{(M_0 - M_z)\Delta t}{T_1}$ where M_0 is the initial magnetization along the *z*-axis.

Rotating frame relaxation lifetimes ($T_{1\rho}$ and $T_{2\rho}$) have not been considered in these simulations. We are in the regime in which the rotating frame relaxation times are typically long (mobile liquids) [37, 38]. $T_{1\rho}$ and $T_{2\rho}$ were also not previously considered in the literature in this regime except at low field (~ kHz) and/or very small pores [37, 39, 40]. Furthermore, the Bloch equation simulations in this section were undertaken following simulations previously performed in the literature [41, 42], which ignored the effect of the rotating frame relaxation lifetimes. Finally, the slices of interest were imaged in this work. The imaged slices were of high quality and well defined, seemingly free from any rotating frame relaxation time effects.

6.6.1 Comparisons of inversion profiles

The DANTE-Z pulse train was 1.58 ms with 7000 Hz as the observation bandwidth of the magnetization response in the simulation of Fig. 6-10a. The HS pulse was 1.58 ms in duration and the magnetization response is shown in an observation bandwidth of 12000 Hz in Fig. 6-10b. One can specify performance characteristics of the pulses from the responses shown in Figs. 6-10a and 6-10b. The selectivity can be calculated employing Eq. (6.2).

$$M_1 = \frac{1}{T_p \, \Delta F} \qquad \textbf{(6.3)}$$

where ΔF is the inversion bandwidth and T_p is the pulse duration [16]. To facilitate a complete separation of the spectral region of interest from neighboring regions, it is important that the slice edges be sharply defined. The sharpness can be calculated by Eq. (6.4):

$$M_2 = \frac{\Delta F}{\Delta f} \qquad \textbf{(6.4)}$$

where Δf is the transition region width. Undesirable off-resonance excitation may be quantified in terms of a suppression ratio R, the ratio of the M_z/M_0 on resonance to the root-mean-square amplitude of the excitation (independent of phase) outside the region $\Delta F + 2\Delta f$ [16]. Uniformity of inversion in the range ΔF can be measured in terms of standard deviation of the inversion values, M_z/M_0, over the ΔF range.

The performance parameters are found in Table 6.5. The DANTE-Z pulse train is sinc modulated to generate a quasi-rectangular slice, but still suffers from side band and

second-order modulations across the DANTE-Z inversion profile Fig. 6-10a. However, adiabatic inversion HS is highly selective and uniform over ΔF. Above a critical threshold, the inversion and magnetization profile are independent of the applied RF power. Clearly, as the RF power is increased, the trajectory executed by a particular isochromat may fluctuate; however, the isochromat comes to rest along the $+z$ or $-z$ directions. Hence above the critical power level, the HS pulse flips spins 360° everywhere but within the selected slice, where the flip angle is 180°.

Areas under the inversion profiles (Table 6.6), which may reflect the total amount of the inverted magnetization, are helpful for the comparison of the selective inversion pulses. To calculate the area under the inversion profiles in Table 6.6, the effective bandwidths (**Δ**f) were considered.

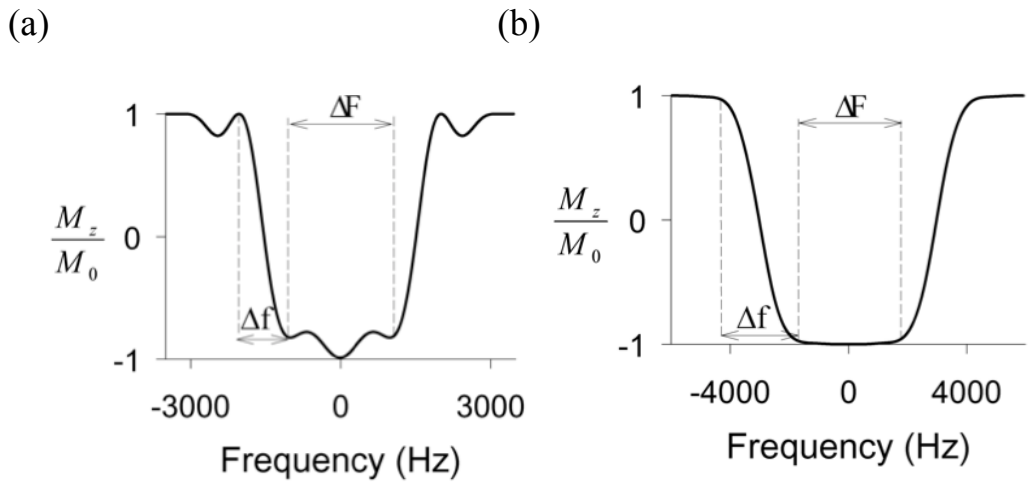

Figure 6-10 (a) Inversion profiles for the DANTE-Z pulse train and (b) the HS pulse. ΔF is the inversion bandwidth and Δf is the transition region width. The DANTE-Z pulse train is sinc modulated to generate a quasi-rectangular slice, but still suffers from side band and second-order modulations or "wobbles" across the DANTE-Z inversion profile. However, adiabatic inversion HS is highly uniform over ΔF.

Table 6.5 Performance parameters for the DANTE-Z pulse train and the HS adiabatic inversion pulse

RF pulse	Selectivity, M_1	Sharpness, M_2	Suppression ratio, R	Standard deviation of the inversion values, σ_{inv}	Area under the inversion profile
DANTE-Z pulse train	0.3	2.2	1.0754	0.282	155
Adiabatic inversion pulse	0.2	1.3	1.0008	0.006	175

6.6.2 Relaxation time effects on inversion profiles

The quality of the inversion profiles will be affected by T_1 and T_2 relaxation. Bloch equation simulations were utilized to investigate the T_1 and T_2 effects on inversion profiles during the pulse T_p and a $t_{interval}$ of 0.5 ms.

Fig. 6-11 shows the change in inversion profiles achieved by the DANTE-Z pulse train, and adiabatic inversion pulse, with T_1 varied from 0.1 to 100 ms. T_2 was set equal to T_1 for each simulated result. The areas under the inversion profiles are reported in Table 6.6. The adiabatic inversion pulse is more robust to T_1 relaxation effects during the pulse. The DANTE-Z pulse train inversion profile does change by more at the center, but the adiabatic inversion changes non-uniformly across the slice. As shown in Fig 6-11b, and Table 6.6 the inversion uniformity breaks down for very short T_1s.

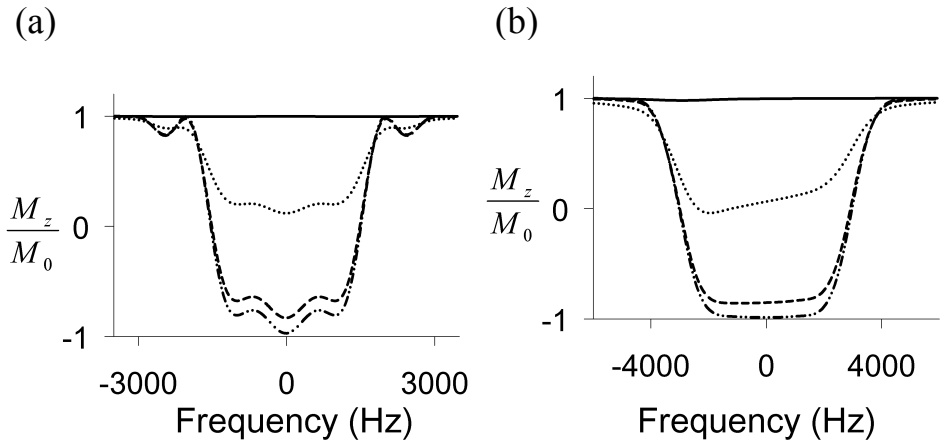

Figure 6-11(a) The change in inversion profile achieved by the DANTE-Z pulse train and (b) HS pulse with T_1 varied between 0.1 (—), 1 (…), 10 (----) and 100 ms (— ··).T_2 was equal to T_1 for each simulated result. The inversion profile uniformity breaks down for very short T_1s.

Table 6.6 The areas under the inversion profiles for the DANTE-Z pulse train and the HS pulse with T_1 varied from 0.1 to 100 ms (T_2 was equal to T_1 for each plot).

$T_1 = T_2$(ms)	Area under inversion profile (unit -less)
0.1	DANTE-Z: 0.3
	HS: 0.5
1	DANTE-Z: 66
	HS: 79
10	DANTE-Z: 138
	HS: 155
100	DANTE-Z: 152
	HS: 171

Fig. 6-12 shows the change in inversion profile achieved by the DANTE-Z pulse train and HS pulse with T_2 varied from 0.1 ms to 100 ms. T_1 was assumed to be ∞ for each plot. The areas under the inversion profiles are reported in Table 6.7.

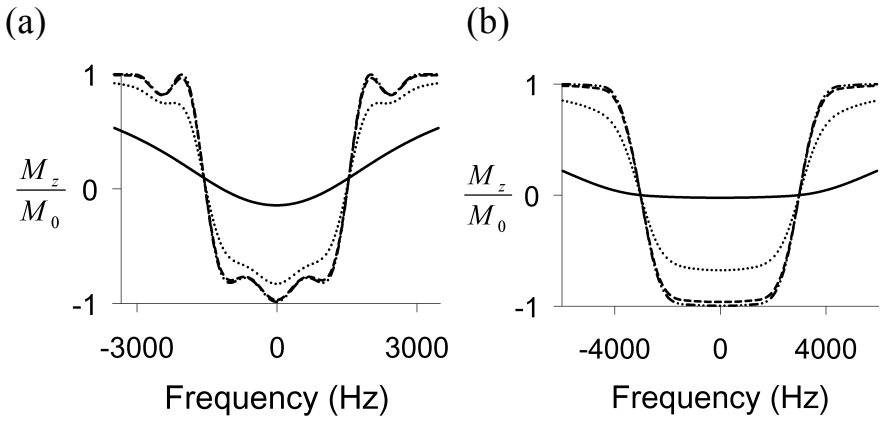

Figure 6-12 (a) The change in inversion profile achieved by the DANTE-Z pulse train and (b) HS pulse with T_2 varied between 0.1(—), 1 (…), 10 (----) and 100 ms (— ··). The inversion profiles will degrade as T_2 decreases. T_1 assumed to be ∞. The profiles are not rectangular and true inversion is not attained. The magnetization outside the inverted slice is reduced.

Table 6.7 The areas under the inversion profiles with T_2 varied from 0.1 to 100 ms (T_1 was assumed to be ∞).

T_2 (ms) ($T_1 = \infty$)	Area under inversion profile (unit -less
0.1	DANTE-Z: 89 HS: 89
1	DANTE-Z: 138 HS: 142
10	DANTE-Z: 149 HS: 170
100	DANTE-Z: 151 HS: 172

The effect of $t_{interval}$ set to 0.5 ms (similar to the selective CPMG experiments) upon cessation of the RF pulse was investigated (results not shown). The sample of interest was assumed to have T_1 as short as 1 ms or 10 ms. For a $t_{interval}$ of 0.5 ms there was 40% and 5% reduction at the center of the inversion profiles for T_1 of 1 ms and 10 ms, respectively.

The DANTE-Z pulse train was investigated to determine sensitivity to RF pulse amplitude (B_1) and duration miscalibrations compared to the HS pulse (results also not shown). Above a threshold value for B_1, the HS pulse is not sensitive to B_1 variation. This is no longer true in the presence of short T_2 values. An increase in B_1 means B_{1eff} has larger transverse components during the pulse, which carries the magnetization into the transverse plane, where very short T_2 components of the signal will undergo decay. Thus the best results are produced when the B_1 field strength is just sufficient to achieve an inversion and not greater [43].

The simulations suggest that the adiabatic pulse inversion profile is highly uniform over the slice and is less sensitive to RF amplitude miscalibration in comparison to the DANTE-Z pulse train. The adiabatic inversion pulse is also more robust than the DANTE-Z pulse train to relaxation time effects during the RF pulse.

6.7 References

[1] C. M. Muir, B. J. Balcom, Pure phase encode magnetic resonance imaging of fluids in porous media, Ann. Rep. NMR Spectrosc. 77 (2012) 81-113.

[2] J. Mitchell, J. Staniland, R. Chassagne, K. Mogensen, S. Frank, E. J. Fordham, Mapping oil saturation distribution, in a limestone plug with low-field magnetic resonance, J. Petrol. Sci. Eng. 108 (2013) 14–21.

[3] B. A. Baldwin, E. A. Spinler, *In situ* saturation development during spontaneous imbibition, J. Petrol. Sci. Eng. 35 (2002) 23–32.

[4] K. R. Brownstein, C. E. Tarr, Importance of classical diffusion in NMR studies of water in biological cells, Phys. Rev. A, 19(6) (1979) 2446-2453.

[5] G. Q. Zhang, G. J. Hirasaki, CPMG relaxation by diffusion with constant magnetic field gradient in a restricted geometry: numerical simulation and application, J. Magn. Reson. 163 (2003) 81-91.

[6] J. Mitchell, T. C. Chandrasekera, D. J. Holland, L. F. Gladden, E. J. Fordham, Magnetic resonance imaging in laboratory petrophysical core analysis, Phys. Rep. 526 (2013) 165-225.

[7] P. Majors, P. Li, E. J. Peters, NMR imaging of immiscible displacements in porous media, SPE Form. Eval. (1997) 164–169.

[8] E. M. Haacke, R. W. Brown, M. R. Thompson, R. Venkatesan, Magnetic resonance imaging ~ physical principles and sequence design, John Wiley &Sons, Inc., 1999.

[9] M. A. Horsfield, E. J. Fordham, C. Hall, L. D. Hall, 1H NMR imaging studies of filtration in colloidal suspensions, J. Magn. Reson. 81 (1989) 593–596.

[10] J. J. Attard, S. J. Doran, N. J. Herrod, T. A. Carpenter, L. D. Hall, Quantitative NMR spin-lattice-relaxation imaging of brine in sandstone reservoir cores, J. Magn. Reson. 96 (1992) 514–525.

[11] O. V. Petrov, G. Ersland, B. J. Balcom, T_2 distribution mapping profiles with phase-encode MRI, J. Magn. Reson. 209 (2011) 39–46.

[12] L. Li, H. Han, B. J. Balcom, Spin echo SPI methods for quantitative analysis of fluids in porous media, J. Magn. Reson. 198 (2009) 252–260.

[13] F. G. Goora, B. G. Colpitts, B. J. Balcom, Arbitrary magnetic field gradient waveform correction using an impulse response based pre-equalization technique, J. Magn. Reson. 238 (2014) 70–76.

[14] S. Vashaee. O. V. Petrov, B. J. Balcom, B. Newling, Region of interest selection of long core plug samples by magnetic resonance imaging: profiling and local T_2 measurement, Meas. Sci. Technol. 25 (2014) 035004-035014.

[15] O. P. Petrov, B. J. Balcom, Local T_2 distribution measurements with DANTE-Z slice selection, J. Magn. Reson. 215 (2012) 109-114.

[16] G. A. Morris, R. Freeman, Selective excitation in Fourier-transform nuclear magnetic resonance, J. Magn. Reson. 29 (1978) 433–462.

[17] A. Tann´us, M. Garwood, Adiabatic pulses, NMR Biomed. 10 (1997) 423–34.

[18] M. Garwood, L. DelaBarre, The return of the frequency sweep: designing adiabatic pulses for contemporary NMR, J. Magn. Reson. 153 (2011) 155–77.

[19] T. Gullion, The effect of amplitude imbalance on compensated Carr–Purcell sequences, J. Magn. Reson, Ser. A 101 (1993) 320–323.

[20] R. Freeman, G. Morris. The “DANTE” experiment, J. Magn. Reson. 213 (2011) 244-246.

[21] P. Xu, X. L. Wu, R. Freeman, User-friendly selective pulses, J. Magn. Reson. 99 (1992) 308–322.

[22] R. Freeman, S. P Kempsell, M. H. Levitt, Radio frequency pulse sequences which compensate their own imperfections, J. Magn. Reson. 38 (1980) 453-479.

[23] Z. H. Cho, Y. M. Ro and I. K. Hong, FM DANTE fast imaging and variations: Emerging rf-based ultrafast imaging techniques, Concept. Magn. Reson. 10 (1998) 33-54.

[24] K. Kose, Visualization of turbulent motion using echo planar imaging with a spatial tagging sequence, J. Magn. Reson. 98 (1992) 599-603.

[25] R. L. Kleinberg, S. A. Farooqui, M. A. Horsfield, T_1/T_2 ratio and frequency-dependence of NMR relaxation in porous sedimentary-rocks, J. Colloid. Interface. Sci. 158 (1993) 195–198.

[26] C. Straley, D. Rossini, H. Vinegar, P. Tutunjian, C. Morriss, Core analysis by low-field NMR, Log Analyst 3 (1997) 84–94.

[27] G. R. Coates, L. Xiao, M. G. Prammer, NMR logging: principles and applications, (Houston, TX, Haliburton), 1999.

[28] D. Rosenfel, S. L. Panfil, Y. Zur, Design of selective adiabatic inversion pulses using the adiabatic condition. J. Magn. Reson. 129 (1997) 115–124.

[29] D. G. Norris, Adiabatic radiofrequency pulse forms in biomedical nuclear magnetic resonance, Concept. Magn. Reson. 14 (2001) 89–101.

[30] S. Conolly, D. Nishimura, A. Macovski, Sweep-diagram analysis of selective adiabatic pulses, J. Magn. Reson. 83 (1989) 549–564.

[31] T. L. Hwang, P. C. van Zijl, M. Garwood. Fast broadband inversion by adiabatic pulses. J. Magn. Reson. 133 (1998) 200-203.

[32] Y. A. Tesiram, M. R. Bendall, Universal equations for linear adiabatic pulses and characterization of partial adiabaticity, J. Magn**.** Reson. 56 (2002) 26-40.

[33] M. H. Levitt, Composite pulses, Prog. Nucl. Magn. Reson. Spectrosc. 18 (1986) 61–122.

[34] F. Marica, F. G. Goora, B. J. Balcom, FID-SPI pulse sequence for quantitative MRI of fluids in porous media, J. Magn. Reson. 240 (2014) 61-66.

[35] M. Halse, J. Rioux, S. Romanzetti, J. Kaffanke, B. MacMillan, I. Mastikhin, N. J. Shah, E. Aubanel, B. J. Balcom, Centric scan SPRITE magnetic resonance imaging: optimization of SNR, resolution, and relaxation time mapping, J. Magn. Reson. 169 (2004) 102–117.

[36] Q. Chen, A. E. Marble, B. G. Colpitts, B. J. Balcom, The internal magnetic field distribution, and single exponential magnetic resonance free induction decay, in rocks, J. Magn. Reson. 175 (2005) 300-308.

[37] S. Michaeli, D. J. Source, M. Garwood, $T_{1\rho}$ and $T_{2\rho}$ Adiabatic relaxations and contrasts, Curr. Anal. Chem. 4 (2008) 8-25.

[38] S. Magia, T. Liimatainen, M. Garwood, S. Michaeli, Rotating frame relaxation during adiabatic pulses vs. conventional spin lock: simulations and experimental results at 4 T, Magn. Reson. Imaging, 27 (2009) 1074-1087.

[39] J. P. korb, Relative role of surface interactions and topological effects in nuclear magnetic resonance of confined liquids, J. Chem. Phys. 101(8) (1994) 7074-7081.

[40] E. Steiner, S. Bouguet-Bonnet, J. L. Blin, D. Canet, Water behaviour in mesoporous materials as studied by NMR relaxometry, J. Phys. Chem. A, 115 (2011) 9941-9946.

[41] D. G. Norris, H. Ludemann, D. Leibfritz, An analysis of the effects of short T_2 values on the hyperbolic-secant pulse, J. Magn. Reson. 92 (1991) 94-101.

[42] Lopez, W. Lu, J. D. Walls, Relaxation selective pulses in fast relaxing systems, J. Magn. Reson. 242(2014) 95-106.

[43] J. G. Powles, The adiabatic fast passage experiment in magnetic resonance, Proc. Phys. Soc. 71 (1958) 497-500.

Chapter 7 - Local T_2 Measurement Employing Longitudinal Hadamard Encoding and Adiabatic Inversion Pulses in Porous Media

The results discussed in Chapter 6 showed that the adiabatic inversion pulse followed by a CPMG pulse train is the preferred way (in comparison with SE-SPI and DANTE-Z CPMG methods) to measure local T_2 distributions where T_2 observation at only few particular locations is required. We now provide a follow-on investigation of local T_2 distribution measurement by employing multiply-selective adiabatic inversion pulses. It is very beneficial in slice selective MR to improve the overall efficiency of data acquisition by employing multi-slice techniques. A multi-band adiabatic inversion can be designed to achieve simultaneous selective excitation of several slices to increase the efficiency of adiabatic inversion CPMG measurements. However, the selection of many slices leads to the superposition of information from different slices; one needs to encode signal information from individual slices. In this work, the information from each slice is encoded in signal phases by employing Hadamard matrices (the elements of which are +/-1 and the rows of which are mutually orthogonal). This chapter is written in paper format since it is intended for submission to the Journal of Magnetic Resonance. The format of references in this chapter follows that of the journal to which the paper will be submitted.

Abstract

Multiple frequency band selective, adiabatic inversion, radio frequency pulses were employed to allow multi-slice T_2 measurements across porous media samples. Multislice T_2 measurement employing the longitudinal Hadamard encoding technique has

an inherent sensitivity advantage over corresponding slice-by-slice local T_2 measurements. The longitudinal Hadamard encoding technique can give localized T_2 information from *n* regions of interest with *n* scans with increased sensitivity compared to *n* single-slice measurements. B_1 insensitivity may be achieved by employing hyperbolic secant adiabatic inversion pulses, which simultaneously invert spins in several well-defined slices. While Hadamard encoding is well established for local spectroscopy, the current work is the first use of Hadamard encoding for local T_2 measurement.

7.1 Introduction

Magnetic resonance (MR) is an important method for characterization of petrophysical properties of reservoir core plugs. Bulk magnetic resonance analysis of fluids in reservoir cores and core plugs (measuring absolute fluid content and relaxation time distributions), is a routine part of petroleum reservoir core analysis. Its routine application to spatially resolved analysis of fluids in porous media is developing [1-7]. T_2 distribution measurements, including T_2 distribution mapping, are widely employed in clinical applications and more recently petroleum reservoir core analysis. Spatially resolved T_2 distribution measurements are, in particular, the most basic measurements employed to determine fluid-matrix properties in MR core analysis. In commonly employed low field MR instruments (0.05 T) it is important to achieve a high sensitivity T_2 distribution measurement.

Two different techniques have been recently introduced in porous media MR to measure the spatially resolved T_2 distribution.

(1) T_2 mapping based on magnetic resonance imaging (MRI) with spatial phase encoding, spin-echo single-point imaging (SE-SPI), has been introduced [1, 6]. This type of T_2 measurement method has the advantage of measuring T_2 at all positions along the sample with high resolution (~1 mm). However, this technique has the drawback of low sensitivity.

(2) Spatially resolved T_2 measurements, based on a slice-selective CPMG measurement, employing a DANTE-Z pulse train or an adiabatic inversion pulse, have recently been developed [5, 7]. In this type of T_2 measurement, T_2 is measured one slice at a time within a sample. Slice selective CPMG measurement is suitable for applications where T_2 observation at only few particular locations is required. The sensitivity of slice selective CPMG measurements, we have recently reported, is greater than with SE-SPI techniques [8]. We have recently shown that adiabatic inversion pulses, followed by a CPMG pulse train, are preferred to DANTE-Z CPMG to measure local T_2 distributions by slice selection.

It is very convenient in slice selective MR to improve the overall efficiency of data acquisition by employing multi-slice techniques [9-13]. A multi-band selective pulse can be designed to achieve simultaneous selective excitation of several slices. The selective excitation of many selected slices leads to the superposition of information from different slices. To separate the individual slice information, the modified experiment must be performed several times with the data stored separately with individual slice information labeled uniquely for each of the sub-experiments [10]. This allows for the correlation of each signal with the corresponding slice. The final calculation of each slice signal may be undertaken by the simple linear combination of the separate stored data

sets. In the literature it has been shown that the phase of a frequency selective pulse may be employed to label the signal from different slices [14-20].

Hadamard multi-slice localized NMR spectroscopic imaging techniques were introduced in the 1980s [19]. Recent reports employ the Hadamard idea in high resolution spectroscopic imaging [21]. In Hadamard spectroscopic imaging, radio frequency (RF) pulses excite or invert spins in multiple regions of interest (ROI), based on the excitation profile of the rows in a Hadamard matrix. The main advantage of Hadamard techniques over single-volume localization is that one can acquire information from *n* different ROIs by *n* scans with the maximum signal-to-noise ratio [16, 18]. While Hadamard encoding is well established for local spectroscopy, the current work is the first use of Hadamard encoding for local T_2 measurement.

In this work, the local T_2 measurement is performed by employing a Hadamard encoding scheme and adiabatic inversion pulses, which invert the magnetization in several well-defined frequency bands. If one requires T_2 information from several ROIs within a large sample, this technique is the most efficient method available.

Goelman and Leigh have shown that although adiabatic rapid passage is highly nonlinear, linear arguments can be employed to acquire data from several slices at the same time [16, 18]. Adiabatic inversion pulses may be added together to construct a multiband inversion pulse. A CPMG measurement preceded by the Hadamard adiabatic inversion scheme for measuring spatially resolved T_2 distribution is presented in this work.

Our Hadamard adiabatic inversion scheme selects slices of 6.5 mm width at a few positions within a large sample. The measured T_2 distributions are of similar quality to

bulk CPMG measurements. The method is a slice selective CPMG technique with improved sensitivity for T_2 mapping in short relaxation time porous media samples, particularly when T_2 is required to be measured at only few positions along the sample, and high sensitivity is required.

7.2 Theory

7.2.1 One-dimensional longitudinal Hadamard encoding

In this section, one-dimensional *n*th-order Hadamard matrices are considered that provide information from (*n-1*) ROI. In the presence of a constant magnetic field gradient, *n* pulses with frequency profiles corresponding to the Hadamard matrix row are employed. After *n* acquisitions, the encoded longitudinal distribution is described by the applied Hadamard matrix [10, 24]. Hadamard matrices ($\mathbf{H}_n$) are known for orders 1, 2, and any multiple of 4, for example:

$$\mathbf{H}_1 = [+], \quad \mathbf{H}_2 = \begin{bmatrix} + & + \\ + & - \end{bmatrix}$$
$$\mathbf{H}_4 = \begin{bmatrix} + & + & + & + \\ + & - & - & + \\ + & + & - & - \\ + & - & + & - \end{bmatrix} \qquad (7.1)$$

where + and – represent magnetization along the $+z$ and $-z$ directions in an MR context. Slices need not be equally spaced or of equal width.

7.2.2 Dual-band adiabatic inversion pulses (construction and restrictions)

The design of single-band hyperbolic secant adiabatic inversion pulses has been described [7, 25]. Two shifted hyperbolic secant adiabatic pulses can be added to generate a double-band inversion adiabatic pulse. For the case of two equal bandwidths, which are shifted to frequencies centered at ω_1 and ω_2, the Hamiltonian is given by [20]:

$$H(t) = \Delta\omega\, I_z + B_1(t)\, e^{i\phi(t)} \left[e^{-i\omega_1 t} + e^{-i\omega_2 t} \right] I_x \qquad \textbf{(7.2)}$$

where I_x and I_z are the spin angular momentum operators. $\Delta\omega$ is the off-resonance frequency, and $B_1(t)$ and $\phi(t)$ are the amplitude and phase function of the adiabatic pulse. It has been shown [16, 18] that unlike the single-band adiabatic pulses, which above an amplitude threshold are independent of the B_1 field, dual-band adiabatic pulses also have an upper limit ($B_1 < |\omega_1 - \omega_2|$). Only between the two limits are dual-band pulses independent of the B_1 amplitude [18]. The necessary conditions to acquire multiple adiabatic inversions at several frequencies, which are required for higher dimensionality Hadamard encoding, are defined in reference [16].

7.2.3 Imaging of the slice selected by a fourth-order longitudinal Hadamard encoding matrix

To visualize the slices of interest, adiabatic inversion pulses were followed by a double half-k SPRITE image acquisition. We have employed similar ideas in several recent papers [26-28] to visualize the slice.

7.2.4 Local T_2 measurement employing longitudinal Hadamard encoding

The CPMG T_2 measurement, preceded by a one-dimensional, fourth-order Hadamard encoding, is shown in Fig. 7-1. Four scans were undertaken, selectively inverting the sample magnetization according to the rows of a fourth-order Hadamard matrix (Eq. (7.1)). Adding and subtracting the four scans recovers the T_2 information from each of the slices.

In matrix notation, the fourth-order Hadamard encoding CPMG measurement may be written as:

$$\mathbf{H_4 S = T} \qquad \textbf{(7.3)}$$

where $\mathbf{H}_4$ is the Hadamard matrix of the fourth-order, **S** is the vector representing the signal from different slices, and **T** is a vector representing the observed CPMG T_2 decay. To find **S**, one can Hadamard transform **T**, which means multiplying **T** by the inverse of $\mathbf{H}_4$, which is equal to:

$$\mathbf{H}_4^{-1} = \frac{1}{4}\begin{bmatrix} + & + & + & + \\ + & - & + & - \\ + & - & - & + \\ + & + & - & - \end{bmatrix} \qquad \textbf{(7.4)}$$

The local T_2 measurement results for four different slices can be reproduced by the multiplication of the experiment results in Fig. 7-1, with the inverse matrix (Eq. (7.4)). One should recall that the slices are encoded by M_z but M_{xy} is measured.

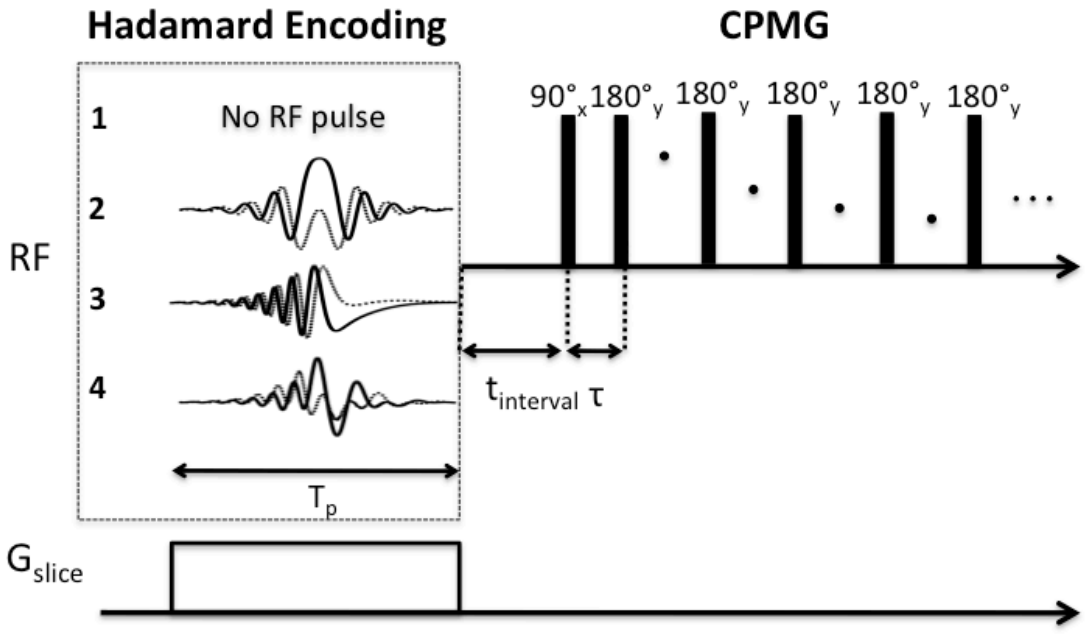

Figure 7-1 CPMG measurement preceded by a one-dimensional, fourth-order Hadamard encoding. The left sides hows RF pulses which produce *z* profiles according to the entries of the four signal rows of the Hadamard matrix, H_4. The adiabatic inversion selective pulses are in complex form, the real (—) and imaginary (-----) parts of the RF pulses are shown. The right side illustrates a CPMG measurement. 2τ is the interval between the 90° pulse and the first echo. CPMG measurement is repeated for all four RF pulses. T_p is the overall inversion pulse duration. The time $t_{interval}$ is the delay after the slice selective pulse ceases and before the first 90° pulse is applied. Adding and subtracting the four scans recovers the T_2 information from each of the ROIs.

7.3 Experimental

7.3.1 Numerical simulations

Numerical simulations of the adiabatic inversion pulses corresponding to each row of $\mathbf{H_4}$ were undertaken, employing a home-built Bloch equation simulation written in the IDL programming environment (ITT, Boulder, CO). The simulation applies a 3×3-rotation matrix for each discrete time increment in an amplitude and phase modulated RF pulse.

7.3.2 Data processing

The Unisort and Acciss processing packages developed in the IDL programming environment (ITT, Boulder, CO) by the UNB MRI Centre were employed for image reconstruction and display. The WinDXP program (Oxford Instruments, Oxford, UK) was employed for T_2 distribution determination. WinDXP allows distributed exponential fitting on data acquired using the RINMR Windows (Oxford Instruments, Oxford, UK) data acquisition software.

7.3.3 Equipment

MRI measurements were performed on a Maran DRX-HF (Oxford Instruments Ltd, Oxford, UK) 0.2 T permanent magnet. The RF probe was a custom-built solenoid, 4.4 cm inner diameter, driven by a 1 kW 3445 RF amplifier (TOMCO Technologies, Sydney, Australia). The RF probe provided 90° RF pulses of 11 μs duration for an input RF power of 300 W. A shielded three-axis magnetic field gradient coil driven by Techron (Elkhart, IN) 7782 gradient amplifiers, provided maximum magnetic field gradients of 26 G/cm, 24 G/cm and 33 G/cm in *x, y*, and *z*, respectively.

7.3.4 Local T_2 measurements of the Berea core plug employing a fourth- order longitudinal Hadamard encoding matrix

Measurements were undertaken on a Berea sandstone core plug (Kocurek industries, Caldwell, TX), 3.8 cm in diameter and 5 cm in length. Berea is coarse-grained, quasi-homogeneous sandstone, considered a standard porous medium for laboratory experiments. The core plug was saturated with 2% brine. The bulk relaxation times were

T_2^* = 764 μs, $T_2(1)$ = 147 ms, 54 %; $T_2(2)$ = 25 ms, 46% with T_2 modeled as a bi-exponential decay. The T_1 was essentially single exponential at 200 ms.

Bulk CPMG parameters were: 90° pulse length = 11 μs with 100% RF power, number of echoes = 2048, repetition delay = 2 s. 16 s were required for 8 signal averages.

Adiabatic inversion pulses based on the last three rows in $\mathbf{H_4}$ (Eq. (7.1)) with T_p = 750 μs and a slice selective magnetic field gradient of 6.4 G/cm with 55% RF power (11.5 kHz) were employed to select 6.5 mm thick slices. In order to ensure that the RF pulse power was sufficient to completely invert the spins in the slice of interest in each case, a free induction decay was measured, in the presence of a magnetic field gradient, to calibrate the hyperbolic secant pulse. Trapezoidal magnetic field gradients with 512 points at 1 μs intervals were employed.

7.4 Results and discussions

7.4.1 Numerical simulations

Bloch equation simulations were employed to investigate the frequency response of the inversion band pulses corresponding to the rows of $\mathbf{H_4}$ (Eq. (7.1)). The simulations were performed for the last three rows of $\mathbf{H_4}$. No RF pulse is applied for the first row. Simulated adiabatic pulses were 1.5 ms in duration, consisting of 321 complex points, which define the amplitude and phase function [7]. RF amplitude and bandwidth were adjusted to produce complex adiabatic inversion pulses, which produce inversion profiles in Figs. 7-2a-c.

For the single-band inversion profiles, as shown in Figs. 7-2a and 7-2b, RF amplitude and bandwidth were 9 kHz and 13.2 kHz, respectively. The simulation shows that for RF > 4.5 kHz, the inversion profile will be insensitive to B_1 field variations.

To produce the inversion profile such that it corresponds to the third row of $\mathbf{H_4}$, a phase factor of $\omega_1 t$ ($\omega_1 t = 2\pi f_1 t$, f_1 = 6.6 kHz) was added to the adiabatic inversion pulse phase equation. The center of the new inversion profile is shifted to 6.6 kHz, as is simulated in Fig. 7-2b. RF amplitude and bandwidth were the same as the adiabatic inversion pulse before being shifted.

As discussed in section 7.2.2, adding two shifted adiabatic pulses creates a double-band inversion adiabatic pulse (Eq. (7.2)). This paper employs two equal bandwidth inversion hyperbolic secant pulses centered at frequencies f_1 = -3.3 kHz and f_2 = 9.9 kHz. The bandwidth of each individual single-band adiabatic pulse was 6.6 kHz, half that of Figs. 7-2a and 7-2b. The simulation result corresponding to the double-band inversion pulse is illustrated in Fig. 7-2c. The separation between the inversion bands is 13.2 kHz. The simulation results show, when the RF amplitudes were just above the lower threshold (3.2 kHz), the inversion profile was, as expected, insensitive to RF field variations. As explained in the Appendix, RF amplitude should be less than the upper limit of B_1, to prevent nonlinear effects corresponding to interaction between the inversion bands [18].

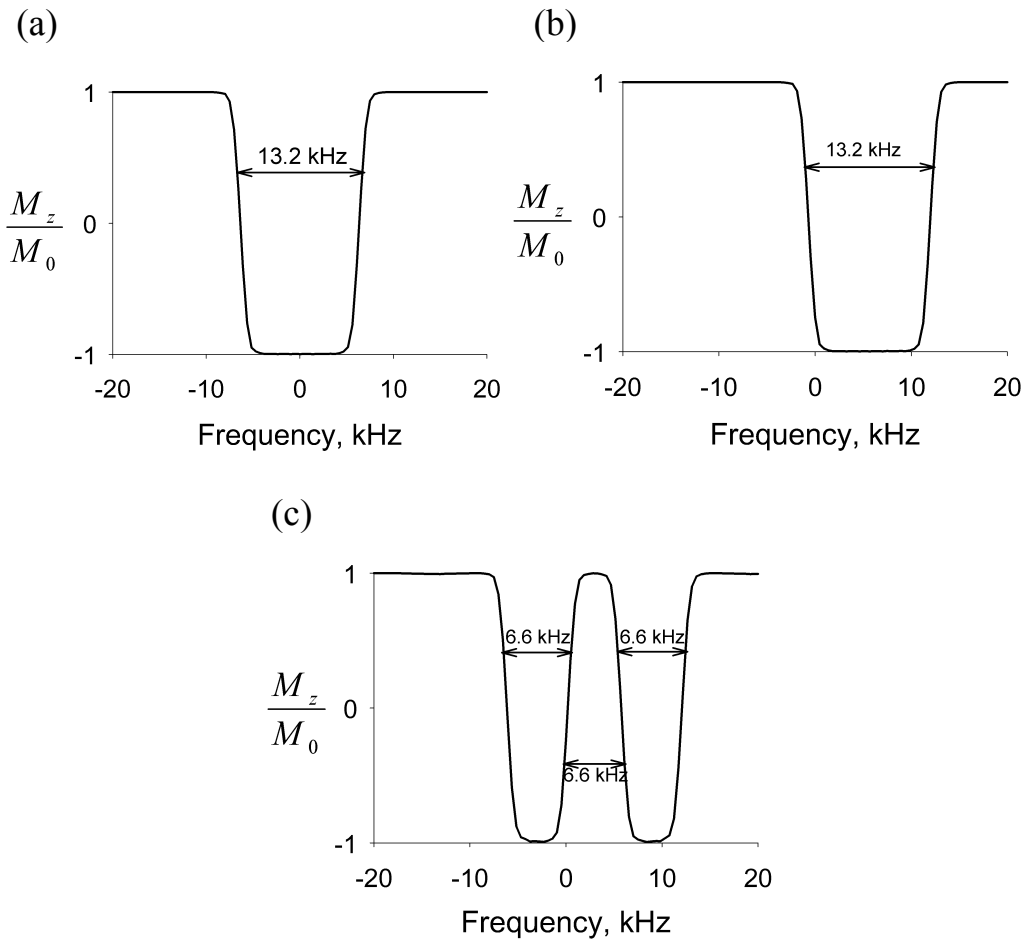

Figure 7-2 Simulated response of the *z* component of the magnetization vector as a function of off resonance frequency after the application of the RF pulses. (a), (b), and (c) corresponds to 2nd, 3th and 4throws in H_4, respectively.

7.4.2 Imaging of the slice selected by a fourth-order longitudinal Hadamard encoding matrix

The adiabatic inversion pulses were employed with a double half-k SPRITE measurement [26] to visualize the ROIs in Berea sandstone, before performing Hadamard encoded CPMG measurements. The time-bandwidth product for a typical RF pulse is a constant; therefore the adiabatic inversion pulse duration can be changed to 750 μs for

experimental purposes. The shorter the RF pulse duration the less relaxation will occur during slice selection.

The one-dimensional profiles from top to bottom in Fig. 7-3a correspond to the rows of $\mathbf{H_4}$. The first profile was produced in the absence of any adiabatic inversion pulse and therefore shows the whole profile of the brine saturated Berea sandstone. The sample was uniform and fully saturated, therefore the one-dimensional axial profile is uniform. The other three profiles, as shown in Fig. 7-3a, correspond to axial profiles of the adiabatic inversion pulses, which are simulated in Figs. 7-2a-c, respectively.

To prevent non-linear effects, as explained in the Appendix, the RF pulse amplitude was calibrated to be less than 12 kHz. In this paper frequency units (kHz) were employed for RF pulse amplitude so one can compare RF pulse amplitude with the RF pulse bandwidth in kHz. . The individual slices, Fig. 7-3b, are produced with the inverse Hadamard matrix multiplied by the axial magnetization profiles in Fig. 7-3a. The profiles demonstrate the accuracy of localization achieved by employing the Hadamard matrix. The slice width is approximately 6.5 mm, which is 13% of the Berea sample length.

Note that a one-dimensional *n*th-order Hadamard experiment provides information from *n-1* ROIs; therefore only three slices of interest will be produced after employing the fourth-order Hadamard matrix. The first slice in Fig. 7-3b represents the rest of the sample close to the edges.

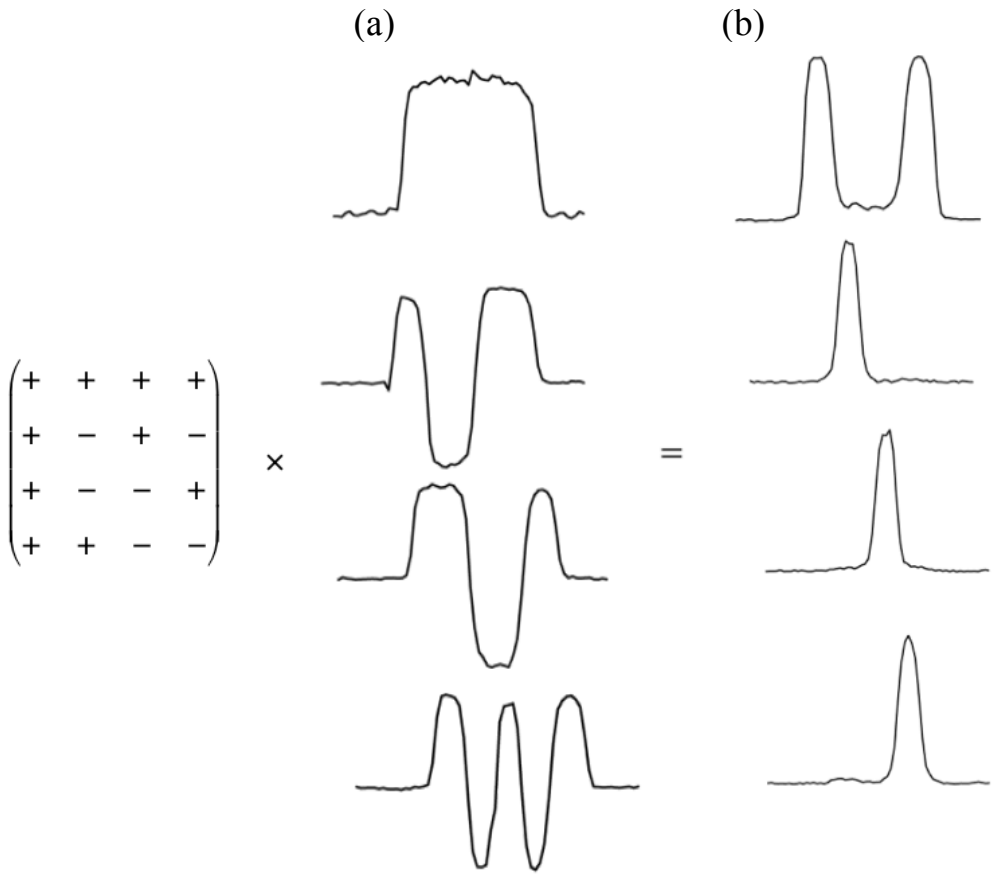

Figure 7-3 The principle of longitudinal Hadamard encoding. (a) shows double-half-k SPRITE profiles of a 5 cm Berea sandstone. The profiles correspond to the rows of the matrix H_4. (b) The individual ROIs are produced by multiplication of the data in (a) by the inverse of the Hadamard matrix (H_4^{-1}) which is shown at left.

Superposition of the one-dimensional profiles is shown in Fig. 7-4. The overlap (cross-talk effect) between the slices can be diminished by increasing the distance between adjacent inversion bands. By choosing $|\omega_1-\omega_2| = 3(bw)$ instead of $|\omega_1-\omega_2| = 2(bw)$, those effects can be reduced. An alternative for reduction of the cross-talk effect is to choose a double width for one of the middle ROIs. The Hadamard matrix, $\mathbf{H_4}$, would then be written as:

$$\mathbf{H}_4 = \begin{bmatrix} + & + & (++) & + \\ + & - & (--) & + \\ + & + & (--) & - \\ + & - & (++) & - \end{bmatrix} \qquad \textbf{(7-7.5)}$$

where each (−) represents an inversion of a 6.6 kHz frequency range.

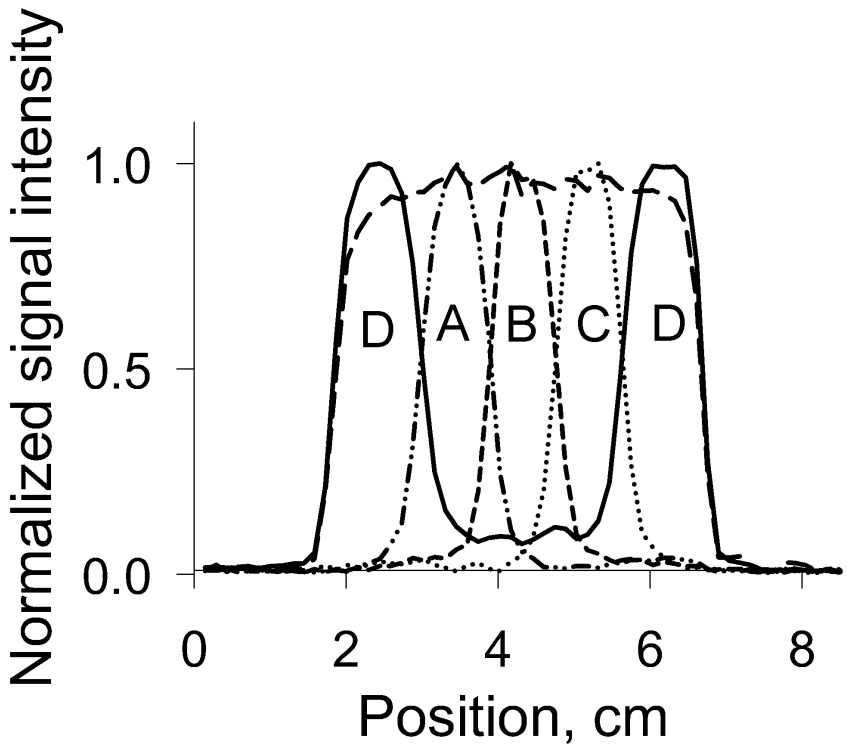

Figure 7-4 Superposition of the one-dimensional fourth order Hadamard encoding double-half-k SPRITE results of Fig. 7-3.

7.4.3 Local T_2 measurements of a Berea sandstone employing a fourth-order longitudinal Hadamard encoding matrix

Bulk CPMG was employed to measure the T_2 distribution for the fully saturated Berea sandstone sample. The bulk T_2 distribution was bimodal with peaks centered at 5 ms and 100 ms. The minimum observable T_2 was 0.2 ms as shown in Fig 7-5. Since the saturated Berea sandstone is uniform, it is reasonably anticipated that the bulk CPMG measurement will agree well with a spatially resolved measurement from a portion of the sample.

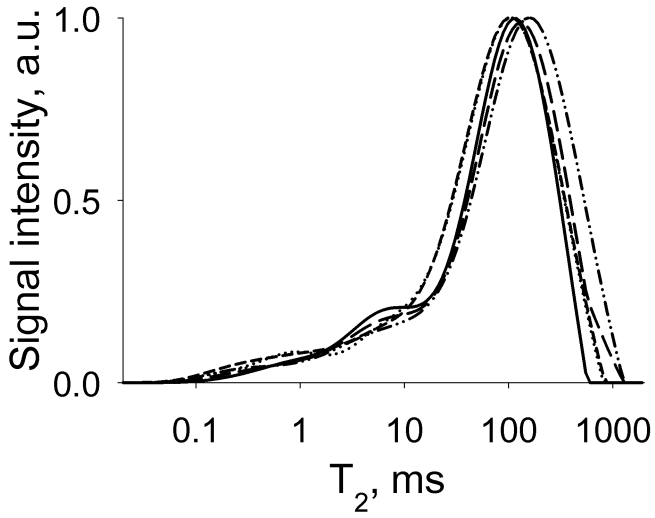

Figure 7-5 T_2 distributions, which are measured from the brine saturated Berea. The results were produced from bulk CPMG (—) and local T_2 measurements. (···), (– – –), and (— ··) show the T_2 distributions for slices A, B, and C respectively, Fig. 7-4. (— — —) shows the T_2 distribution for the central slice which is measured by employing slice-by-slice adiabatic inversion CPMG measurements. For all T_2 measurements 2τ was 200 μs.

The CPMG measurement, preceded by a one-dimensional, fourth-order Hadamard encoding (Fig. 7-1) was employed to measure T_2 for three slices, width 6.5 mm, from the

fully saturated Berea. One slice at the center of the sample and two slices displaced from the sample center were selected. To compare the Hadamard encoding CPMG measurement results with the slice-by-slice CPMG measurement described in [7], T_2 was measured for a slice 6.5 mm wide, at the center of the sample. The T_2 distributions (Fig. 7-5) show that local T_2 measurements can reproduce a minimum T_2 of 0.2 ms. The T_2 distributions are in good agreement with bulk CPMG results.

The T_2 distributions are normalized in Fig. 7-5 to facilitate comparison. Note that the signal to noise ratio (SNR) of bulk CPMG and Hadamard encoding CPMG will not be the same. The measurement sensitivity is defined as $SNR/\sqrt{t}$, where t is the total measurement time. For the measurements the signal was measured as the maximum signal intensity in the time domain CPMG decay. The noise was calculated as the standard deviation of the signal intensity after full decay of the time domain CPMG data. The sensitivities are reported in Table 7-1.

Hadamard encoding CPMG and slice-by-slice CPMG methods measure the same quantity of material; a 6.5 mm slice of interest, which incorporates 13% of the material, from a 5 cm, saturated Berea sandstone. To compare the sensitivity of the above measurements with bulk CPMG all the sensitivities were adjusted to equivalent quantities of material (Table 7-1). The sensitivities are normalized by length. The sensitivity per millimeter of the Hadamard encoding CPMG is 1.6 times that of the slice-by-slice CPMG measurement. Hadamard encoding measurements are more sensitive than the slice-by-slice CPMG due to the superposition of signals from four successive measurements. Note that the overall acquisition time of Hadamard encoding and basic slice-by-slice CPMG

measurements are the time for the four measurements, which produce three slices of interest for both methods.

Table 7.1 Sensitivity comparisons for different T_2 mapping methods

Parameters	Bulk CPMG	Hadamard encoding CPMG	Slice-by-slice CPMG
SNR	571	170	109
Overall acquisition time, t (s)	16	64[a]	64[a]
Sensitivity, $\frac{SNR}{\sqrt{t}}$	142	21.3	13.6
Sensitivity per mm[b]	2.8	3.3	2.1

[a] Acquisition time for four measurements which produce three slices

[b] Sensitivity was adjusted through normalization by sample length or slice width.

Hadamard encoding based T_2 distribution measurements may be advantageous in MR measurements of reservoir core plugs that are naturally performed at low magnetic field with low instrument SNR. The method is useful where one is interested in measuring T_2 in several small ROIs within a large sample, and it is an advantage to selectively increase SNR for specific ROIs without the need to acquire high-resolution T_2 measurements for the entire sample.

7.5 Conclusion

A new local T_2 measurement method employing longitudinal Hadamard encoding has been developed and tested. The method permits multi-slice T_2 measurement with optimal sensitivity. Results from the T_2 distribution measurements show the same quality as those obtained with bulk CPMG and slice-by-slice adiabatic inversion CPMG. However, the sensitivity has been improved.

This work is the first application of Hadamard encoding for local T_2 measurement. Local T_2 measurement employing longitudinal Hadamard encoding and adiabatic inversion pulses provides an alternative to slice-by-slice adiabatic inversion CPMG or to SE-SPI, when T_2 needs only be measured at a few ROIs within a large sample and high spatial resolution is not necessary. In contrast to SE-SPI, the method can yield either contiguous or non-contiguous slices. Hence, the method will be very beneficial for MR of porous media at low field. High dimensionality Hadamard encoding T_2 distribution measurements have great potential. In the three-dimensional case, Hadamard encoding CPMG can produce T_2 information from n volumes of interest with n scans. However, slice-by-slice CPMG measurement would require 2^n scans to produce T_2 information for n volumes of interest.

7.6 Appendix

For the dual-band adiabatic inversion pulse, when the RF amplitude was increased, a loss of *z* magnetization on both sides of the inversion bands was observed, as shown in Fig. 7-6. Goelman and Leigh have shown [18] that this nonlinear effect corresponds to an interaction between the inversion bands. Unlike the single-band adiabatic pulses, which above an RF amplitude limit are independent of the RF amplitude, the dual band adiabatic inversion pulse also has an upper limit ($B_1 < |\omega_1-\omega_2|$). For the higher RF amplitudes, 6 kHz, 8 kHz, 10 kHz, in terms of frequency, the nonlinear effects are obvious in Fig. 7-6. As RF amplitude increases, the *z* peak amplitudes outside the inversion bands increase and their frequencies shift toward the inversion bands.

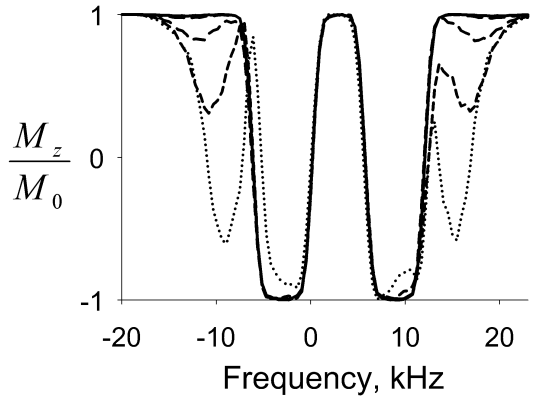

Figure 7-6 Simulated response of the *z* component of the magnetization vector as a function of off resonance frequency after the application of a double-band adiabatic inversion pulse. The double-band pulse was formed by the addition of two single-band pulses with 6.6 kHz bandwidths and a separation of 13.2 kHz. (—) shows the *z* magnetization profile for an RF amplitude 4 kHz slightly above the lower threshold 3.2 kHz. (– – –), (----), (···) and show the appearance of two extra *z* peaks when the RF amplitude is at 6 kHz, 8 kHz, and 10 kHz, respectively . The *z* peak amplitudes increase and their frequencies shifts toward the inversion bands as RF amplitude increases.

7.7 References

[1] O.V. Petrov, G. Ersland, B.J. Balcom, T_2 distribution mapping profiles with phase encode MRI, J. Magn. Reson. 209 (2011) 39–46.

[2] C.M. Muir, B.J. Balcom, Pure phase encode magnetic resonance imaging of fluids in porous media, Ann. R. NMR S. 77 (2012) 81-113.

[3] J. Mitchell, J. Staniland, R. Chassagne, K. Mogensen, S. Frank, E. J. Fordham, Mapping oil saturation distribution, in a limestone plug with low-field magnetic resonance, J. Petrol. Sci. Technol. 108 (2013) 14–21.

[4] B.A. Baldwin, E.A. Spinler, In situ saturation development during spontaneous imbibition, J. Petrol. Sci. Eng. 35 (2002) 23–32

[5] O.V. Petrov, B.J. Balcom, Local T_2 distribution measurements with DANTE-Z slice selection, J. Magn. Reson. 215 (2012) 109–114.

[6] L. Li, H. Han, B.J. Balcom, Spin echo SPI methods for quantitative analysis of fluids in porous media, J. Magn. Reson. 198 (2009) 252–260.

[7] S. Vashaee. O.V. Petrov, B.J. Balcom, B. Newling, Region of interest selection of long core plug samples by magnetic resonance imaging: profiling and local T_2 measurement, Meas. Sci. Technol. 25 (2014) 035004-035014.

[8] S. Vashaee, F. Marica, B. Newling, B.J. Balcom, A Comparison of magnetic resonance methods for spatially resolved T_2 distribution measurements in porous media, Meas. Sci. Technol. (2014) Submitted.

[9] G. Batta, K. Kover, C. Szatay, Methods for structure elucidation by high-resolution NMR: Application to organic molecules of moderate molecular weight, Elsevier, Oxford, 1997.

[10] B. Newling, J.A. Derbyshire, T.A. Carpenter, D.A. Xing, L.D. Hall, Construction of Multiply band-selective self-refocusing pulses for simultaneous spin-echo multislice imaging of fluid flow, using pulsed field gradients, J. Magn. Reson. 108 (1995) 269-273.

[11] E. Kupce, R. Freeman, Techniques for multislice excitation, J. Magn. Reson. 105 (1993) 234-238.

[12] P. E. Z. Larson, A.B. Kerr, A.P. Chen, M.S. Lustig, M.L. Zierhut, S. Hua, C.H. Cunningham, J.M. Pauly, J. Kurhanewicz, D.B. Vigneron, Multiband excitation pulses for hyperpolarized 13C dynamic chemical-shift imaging. J. Magn. Reson.194 (2008) 121–127.

[13] K.J. Lee, M.N.J. Paley, J.M. Wild, Combined simulated annealing and Shinnar–Le Roux pulse design of slice-multiplexed RF pulses for multi-slice imaging, J. Magn. Reson. 182 (2006) 133-142.

[14] L. Castañar, P. Nolis, A. Virgili, T. Parella, Simultaneous multi-slice excitation in spatially encoded NMR experiments. Chemistry, 19 (2013) 15472–15475.

[15] K.J. Lee, J.M. Wild, P.D. Griffiths, M.N.J. Paley. Simultaneous multislice imaging with slice-multiplexed RF pulses. Magn. Reson. Med. 54 (2005) 755–60.

[16] G. Goelman, J.S. Leigh, Multiband adiabatic inversion pulses, J. Magn. Reson. 101 (1993) 136-146.

[17] C. Dalvit, S. Young Ko, J. M. Bohlen, Single and multiple-selective excitation combined with pulsed field gradients. 131 (1996) 124–131.

[18] G. Goelman, J.S. Leigh, B_1-insensitive Hadamard Spectroscopic Imaging Technique. J. Magn. Reson. 91 (1) (1991) 93–101.

[19] A.G. Marshall, Fourier, Hadamard, and Hilbert transforms in Chemistry, Plenum press, New York, 1982.

[20] G. Goelman, V.H. Subramanian, J. Leigh, Transverse hadamard spectroscopic imaging technique, J. Magn. Reson. 89 (1990) 437-454.

[21] O. Cohen, A. Tal, G. Goelman, O. Gonen, Non-spin-echo 3D transverse Hadamard encoded proton spectroscopic imaging in the human brain, Magn. Reson. Med. 70 (2013) 7-15.

[22] R. Reddy, J.S. Leigh, G. Goelman, Hadamard spectroscopic imaging polarization transfer technique, J. Magn. Reson. 101 (1993) 139-144.

[23] G. Goelman, Fast Hadamard spectroscopic imaging techniques, J. Magn. Reson. 104 (1994) 212-218.

[24] L. Bolinger, J.S. Leigh, Hadamard spectroscopic imaging (HSI) for multivolume localization, J. Magn. Reson. 80 (1988) 162-167.

[25] Y.A. Tesiram and M.R. Bendall, Universal equations for linear adiabatic pulses and characterization of partial adiabaticity, J. Magn. Reson. 56 (2002) 26-40.

[26] M. Halse, D.J. Goodyear, B. MacMillan, P. Szomolanyi, D. Matheson, B.J. Balcom, Centric scan SPRITE magnetic resonance imaging, J. Magn. Reson. 165 (2003) 219-229.

[27] M. Halse, J. Rioux, S. Romanzetti, J. Kaffanke, B. MacMillan, I. Mastikhin, N.J. Shah, E. Aubanel, B.J. Balcom, Centric scan SPRITE magnetic resonance imaging: optimization of SNR, resolution and relaxation time mapping, J. Magn. Reson. 169 (2004) 102-117.

[28] Q. Chen, M. Halse, B.J. Balcom, Centric scan SPRITE for spin density imaging of short relaxation time porous materials, Magn. Reson. Imaging. 23 (2005) 263-266.

Chapter 8 – Conclusions and Future Work

8.1 Conclusion

A novel B_1 mapping method was demonstrated in Chapter 3. The method is based on measurements of image intensities acquired with a series of low flip angle excitation pulses employing centric scan SPRITE. The method is reliable, robust, and very simple. The B_1 mapping technique in the thesis utilized the principle of reciprocity so the SPRITE signal in each pixel is proportional to B_1^2 due to B_1 sensitivity in both excitation and the reception. The B_1^2 sensitivity makes the method very sensitive to B_1 variation in the sample space. Furthermore, the pure phase encode nature of the method permits a detailed measurement of B_1 field around conductive structures, which is not possible with conventional B_1 mapping methods. The B_1 field inhomogeneity has two distinct causes; first an interaction between the RF field and the sample being imaged, and second, the inherent inhomogeneity of the RF coil. One may distinguish these two effects by employing the B_1 mapping method described.

A simple approach was introduced to correct B_1 inhomogeneity effects by application of the measured B_1 field maps. Corrected SPRITE images resulted from dividing the original image by relative maps of B_1^2. Because the new B_1 mapping method requires acquisition of six to eight discrete images, it is slower than many B_1 mapping methods in the literature. However, the data handling and data manipulation is very easy. The B_1 mapping methodology was extended to two and three dimensions, and readily translated to both high and low field systems.

The B_1 mapping procedure presented in Chapter 3 works well as a pure phase encode method in the presence of conductive structures that support eddy currents. SPRITE measurements are largely immune to susceptibility and gradient induced eddy current artifacts. As a result, one can isolate the effects of metal objects on the B_1 field, which affects both the excitation, and detection of the MR signal. This isolation is challenging with frequency encoding MRI methods, which often suffer from B_0 inhomogeneity artifacts.

In Chapter 4, the newly new developed B_1 mapping technique was employed to investigate distortions in B_1 fields in the presence of the metal strips, where the surface of the metal was perpendicular to B_1 and parallel to B_0. Simulations of B_1 field induced eddy currents were also undertaken. The B_1 induced eddy currents result in distortion of the B_1 field in the sample space. The B_1 simulation results were in good agreement with experimental results, and illustrated the significant effects of conductors on the B_1 field distribution and B_1 amplitude in the surrounding space. The electrical conductivity of the metal has a negligible effect. The strip geometry was chosen to mimic metal electrodes. Recently, B_1 induced eddy current effects have become important in the development of NMR and MRI techniques for *in situ* studies of electrochemical process. The results are, specifically, important for NMR and MRI of batteries and other electrochemical devices.

The results in Chapter 5 demonstrated region of interest selection within the FOV of long core samples by employing spatially selective adiabatic inversion pulses. This technique allows for reduced FOV, higher resolution imaging and localized T_2 measurements. Adiabatic inversion pulses are immune to radio frequency field inhomogeneity. The dhk SPRITE method following the selection yields naturally density

weighted axial profiles of the sample and the inverted ROI. Although spatial encoding and excitation may be non-ideal near the edges of the FOV, subtraction of the inversion profile from the whole profile yields an undistorted slice. This method is particularly useful in MRI of long cores in the oil and gas industry, where the sample of interest is frequently much longer than the natural FOV defined by the radio frequency coil and region of constant magnetic field gradient. Local T_2 distribution measurement employing adiabatic inversion pulses is the most important outcome of Chapter 5. Such measurements will be of great value in core analysis.

In Chapter 6, a comparison of SE-SPI and slice selective CPMG measurements was undertaken, for petroleum reservoir core plugs and porous media samples. The results suggest that an adiabatic inversion slice selection followed by a CPMG pulse train is the preferred way to measure local T_2 distributions, provided a regional measurement of coarse spatial resolution is sufficient. The method has a great value in MR of porous media at low field and yields high sensitivity local T_2 measurements.

A new local T_2 measurement method employing longitudinal Hadamard encoding and adiabatic inversion pulses has been developed and tested in Chapter 7. The method permits multi-slice T_2 measurement with optimal sensitivity. The T_2 distribution measurements show the same quality as those obtained with the bulk CPMG and slice-by-slice adiabatic inversion CPMG in Chapter 6. However, the sensitivity has dramatically been improved in comparison with slice-by-slice adiabatic inversion CPMG.

8.2 Future work

It is anticipated that both new B_1 mapping and local T_2 measurements methods that have been developed will be employed extensively in the UNB MRI Centre.

In Chapter 3 one-dimensional SPRITE images were corrected by determining relative B_1 maps. The B_1 correction method can be simply extended to correct spatial non-uniformity in two and three-dimensional SPRITE images. The corrected SPRITE images result from dividing the original image by relative maps of B_1^2. However, if one knows how the image intensity depends on B_1 field strength for other commonly employed MRI experiments, the image may be corrected through knowledge of absolute B_1 maps. The B_1 correction method can be particularly useful for the common spin echo MRI experiment.

Knowledge of the B_1 field distribution may be useful in tailored radio frequency pulse excitation, which are required for uniform excitation of regions of interest or selective saturations.

The new B_1 mapping method may also be applicable in parallel excitation techniques. Parallel excitation methods, which utilize multiple transmit coils with spatially distinct B_1 profiles and distinct current waveforms, have been used to improve excitation profiles and/or to reduce the duration of complex RF pulses, which is especially important for MR measurements of fast decaying species or in strong main field non-uniformities.

In both of the above applications, the correspondence of the desired and achieved excitation profile depends on knowledge of the spatial distribution of the B_1 field, which must be measured.

The B_1 mapping method may be employed to determine the B_1 field distribution in both the inner and outer volumes of any RF coil design. The method may also provide an easy means of evaluating coil designs for MR engineering purposes. The resultant B_1 maps are useful for checking the quality of RF coil manufacturing and for validating RF field calculations. It is also important to be able to determine the extent of the spatial field homogeneity of the RF coil to specify the largest possible sample that can be employed. The electrical conductivity of materials may be obtained via B1 mapping, which can particularly be useful in MR of porous media and tumor diagnosis in medical imaging.The results in Chapter 4 will particularly be useful for NMR and MRI of batteries and other electrochemical devices. Such analyses will become valuable in many applications involving battery systems. In electrochemical MRI, orienting the electrodes such that they are largely parallel to the B_1 field (B_0 field either parallel or perpendicular) will significantly reduce induced B_1 eddy current effects. The objects employed were electrode-like strips of metals, but one may employ the B_1 mapping experiment and/or simulations to quantify B_1 related effects around arbitrarily complex metallic structures. The method may be employed to visualize the B_1 distribution in the presence of metallic biomedical implants, such as aneurysm clips, endoprostheses, and internal orthopedic devices, which give rise to artifacts in the MRI of patients.

The spatially resolved T_2 measurements based on a slice-selective CPMG, either slice-by-slice or multiple slices, may be employed wherever the monitoring of T_2 at distinct locations is required For example, if one needs to measure the T_2 distribution during a very long and/or repetitive experiment (e.g. a core flood experiment) and wants to avoid processing a large amount of data, the method may be very convenient.

The preparation of magnetization may be achieved by utilizing saturation adiabatic pulses. One may select an ROI by saturation of the rest of the magnetization outside the ROI in this way. We expect good saturation of magnetization out of the ROI due to the insensitivity of adiabatic pulses to B_1 inhomogeneity.The Hadamard encoding T_2 measurement, which has optimal sensitivity in comparison with slice-by-slice adiabatic inversion CPMG and SE-SPI T_2 measurements, can be extended to two and three dimensions. High dimensionality Hadamard encoding T_2 distribution measurements have great potential. This is an important extension for low magnetic field MR measurements in "UNB MRI Centre". For example, two dimensional T_2 distribution mapping in fluid saturated core plugs is highly desirable because the bedding plane structure in rocks often results in different pore properties within the sample.

Curriculum Vitae

Candidate's full name: Sarah Vashaee

Universities attended:

January 2012 - April 2015, Ph.D candidate, University of New Brunswick, Fredericton, NB, Canada

September 2009 - January 2012, Master student, University of New Brunswick, Fredericton, NB, Canada

September 2003 - September 2008, Bachelor of Science, Sharif University of Technology, Tehran, Iran

Publications:

[1] **S. Vashaee**, B. Newling, B. MacMillan, B.J. Balcom, B_1 mapping with a pure phase encode approach: Quantitative density profiling, J. Magn. Reson. 232 (2013) 68-75.

[2] **S. Vashaee**, O.V. Petrove, B.J. Balcom, B. Newling, Region of interest selection of long core plug samples by magnetic resonance imaging: profiling and local T_2 measurement, Meas. Sci. Technol. 25 (2014) 035004-035014.

[3] **S. Vashaee**, F. Goora, M.M. Britton B. Newling, B.J. Balcom, Mapping B_1-induced eddy current effects near metallic structures in MR images: a comparison of simulation and experiment, J. Magn. Reson. 250 (2015) 17-24.

[4] **S. Vashaee**, F. Marica, B. Newling, B.J. Balcom, A Comparison of magnetic resonance methods for spatially resolved T_2 distribution measurements in porous media, Meas. Sci. Technol. 26 (2015) 055601-055617.

[5] **S.Vashaee**, B. Newling, B.J. Balcom, Local T_2 measurement employing longitudinal Hadamard encoding and adiabatic inversion pulses in porous media, J. Magn. Reson. Under preparation for submission.

[6] B.J. Balcom, **S. Vashaee**, B. Newling, B. MacMillan, Methods of radio frequency magnetic field mapping, U.S. Patent, 8,890,527, awarded November 18, 2014.

Conference Presentations:

[1] **S. Vashaee**, B. Newling, B.J. Balcom, Reduced field of view profiling of long core samples employing spatially selective adiabatic inversion pulses, Poster presentation at the 11^{th} International Conference on Magnetic Resonance Microscopy Joint Topic Conference on NMR in Well logging and Core Analysis (ICMRM11), August 14-18, 2011, Beijing, China.

[2] **S. Vashaee**, B. Newling, B.J. Balcom, Local T_2 measurement employing spatially selective Shinnar-Le-Roux pulses, Poster presentation at the 11^{th} International Conference on Magnetic Resonance Microscopy Joint Topic Conference on NMR in Well logging and Core Analysis (ICMRM11), August 14-18, 2011, Beijing, China.

[3] **S. Vashaee**, B. Newling, B. MacMillan, B.J. Balcom, B_1 mapping with a pure phase encode approach: quantitative density profiling, Presentation at the 11^{th} Bologna Conference on Magnetic Resonance in Porous Media (MRPM11), September 9-13, 2012, University of Surrey, Guildford, UK.